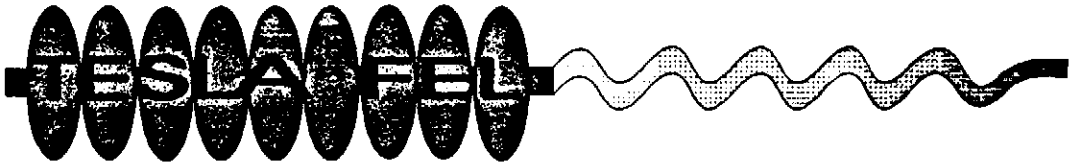

Deutsches Elektronen-Synchrotron, DESY

A VUV Free Electron Laser at the TESLA Test Facility at DESY

Conceptual Design Report

Members of the Study Group:

This report is based on work started at DESY in spring 1994. The scientific case has been discussed on two meetings on November 16, 1994 and on April 27/28, 1995. Contributions to either the scientific case or the machine concept were made by:

Åberg, T.	Helsinki Univ. of Technology
Al-Shamery, K.	Univ. Bochum
Bacher, R.	DESY
Backe, H.	Univ. Mainz
Becker, U.	FHI Berlin
Böwering, N.	Univ. Bielefeld
Bonifacio, R.	INFN, Milano
Bradshaw, A.	FHI Berlin
Brefeld, W.	DESY
Colby, E.	Fermilab Chicago
Comtet, G.	Lab. de Photophys. Moléculaire Paris
DeCastro, R.	LNLS Campinas
Dohlus, M.	DESY
Dujardin, G.	Lab. de Photophys. Moléculaire Paris
Eberhard, W.	KFA Jülich
Edwards, H.	DESY
Faatz, B.	DESY
Fawley, W. M.	Lawrence Berkeley Laboratory LBL
Federmann, F.	MPI Strömungsforschung Göttingen
Feldhaus, J.	DESY
Feldmann, D.	Univ. Bielefeld
Feulner, P.	TU München
Flöttmann, K.	DESY
Freund, H. J.	Univ. Bochum
Gamp, A.	DESY
Ganteför, G.	KFA Jülich
Goldstein, J.	Los Alamos Nat. Lab.
Greinert, W.	Univ. Bochum
Gürtler, P.	DESY
Hanke, K.	DESY
Hellner, L.	Lab. de Photophys. Moléculaire Paris
Hoffmann, P.	FHI Berlin
Jovin, T. M.	Max-Planck-Inst. f. Biophys. Chemie Göttingen
Kamke, W.	Univ. Freiburg
Kiernan, L. M.	DESY
Kipp, L.	Univ. Kiel
Kisker, E.	Univ. Düsseldorf
Krzywinski, J.	Polish Acad. of Sciences Warschau
Kunz, C.	Univ. Hamburg
Leenen, M.	DESY

Leisner, Th.	FU Berlin
Limberg, T.	DESY
Martensson, M.	Uppsala Univ.
Materlik, G.	DESY
Meiwes-Broer, K. H.	Univ. Rostock
Menzel, D.	TU München
Möller, T.	DESY
Mosnier, A.	CE Saclay
Müller-Dethlefs, K.	Univ. München
Nicol, T.	Fermilab Chicago
Nikitina, Y.	Tomsk Univ., Russia
Pagani, C.	INFN Milano
Palmer, R. E.	Univ. Birmingham
Pflüger, J.	DESY
Pierini, P.	INFN Milano
Proch, D.	DESY
Rosenzweig, J.	UCLA Los Angeles
Roßbach, J.	DESY
Rottke, H.	Max-Born-Inst. Berlin
Rubensson, J. E.	KFA Jülich
Rühl, E.	FU Berlin
Rzazewski, K.	Polish Acad. of Sciences Warschau
Saldin, E. L.	ASC Samara
Sandner, W.	Max-Born-Inst. Berlin
Scharlemann, T.	Lawrence Livermore Natl . Lab. LLNL
Schmahl, G.	Univ. Göttingen
Schmidt-Böcking, H.	Univ. Frankfurt
Schneider, C. M.	Max-Planck-Inst. f. Mikrostrukturphys. Halle
Schneider, J.	DESY
Schneidmiller, E. A.	ASC Samara
Schreiber, S.	DESY
Schwentner, N.	FU Berlin
Seidel, M.	DESY
Sekutowicz, J.	DESY
Serafini, L.	INFN Milano
Sheffield, R. L.	Los Alamos Nat. Lab.
Skibowski, M.	Univ. Kiel
Sonntag, B.	Univ. Hamburg
Spielberger, L.	Univ. Frankfurt
Steinrück, H.-P.	Univ. Würzburg
Tesch, K.	DESY
Trines, D.	DESY
Voß, H. J.	Univ. Hamburg
Walker, N.	DESY
Wanzenberg, R.	DESY
Weise, H.	DESY
Westphal, C.	Univ. Essen
Wiik, B. H.	DESY
Will, I.	Max-Born-Inst. Berlin
Wipf, S. G.	DESY
Wöste, L.	FU Berlin

Wurth, W.	TU München
Yurkov, M. V.	JINR Dubna
Zacharias, H.	Univ. Essen
Zimmermann, P.	TU Berlin

Table of Contents

EXECUTIVE SUMMARY

DESY proposes to construct a fourth generation VUV light-source yielding a coherent, very bright beam of photons with wave lengths tunable between 20 nm and 6 nm. This source is based on the principle of Self Amplified Spontaneous Emission (SASE) and consists of the following main elements:

- A radio frequency photoinjector delivering short dense bunches of electrons.
- A series of magnet systems designed to compress the electron bunches longitudinally from initially 2 mm down to 50 μ.
- A 1 GeV electron linear accelerator based on superconducting Nb cavities.
- A 30 m long, very precise undulator.
- Experimental facilities.

The short, very dense, nearly monoenergetic bunch of electrons produced by the source and compressor system is accelerated to high energies in the linear accelerator without diluting its properties, and then passed through the undulator yielding a laser like burst of light.

The performance of this world wide unique light-source is far superior to the performance of conventional third generation light-sources now operating or under construction. Indeed the average values of brilliance and photonflux are about three orders of magnitude higher than those of sources like BESSY II, ALS and ELETTRA. The peak values are more than eight orders of magnitude higher. Of special advantage are the high degree of coherence, the polarization, the extremely short pulse length and the fast tunability of the photon energy.

The scientific potential of this facility has been explored by external working groups focussing on a wide range of topics. They conclude that the unique properties of this facility will open up new and exciting areas of basic and applied research in a number of disciplines ranging from biology, chemistry to

physics. However, to fully exploit the high quality of the beams new experimental techniques, based on the most advanced optical elements, detectors and electronics must be developed.

The construction of this unique VUV facility has only recently become possible due to advances at DESY and elsewhere in the production and acceleration of very dense, high current electron beams as required for the next generation of large electron-positron linear colliders. An electron-positron collider made of superconducting long wave length radio frequency cavities is also the back bone of a tunable, very bright, coherent source of photons at wave lengths of 0,1 nm, the scale of atomic phenomena.

Endorsed by its Scientific Council DESY is now developing the superconducting radio frequency technology which will provide the basis for the construction of a large electron-positron collider with integrated X-ray laser sources. These activities are carried out within the framework of the large international TESLA collaboration presently consisting of 28 Institutes from eight countries. These institutions contribute components and skilled man power to the TESLA Test Facility (TTF) now under construction at DESY.

The TTF R&D programme includes also the construction of a 500 MeV superconducting linear accelerator which will be used as a driver of an undulator to demonstrate the SASE principle for the first time at short wave lengths. This demonstration experiment which is scheduled for 1997/98 will - besides information of the SASE process itself - give experience in handling this unique, bright and powerful beam.

The proposed VUV laser makes full use of the TTF SASE upgraded and augmented as follows:

- **The radio frequency photoinjector.** Only the cathode rf cavity and the focussing system must be replaced.

- **The longitudinal bunch compression system.** A third bunch compressor must be added at the 500 MeV point.

- **The linear accelerator.** It must be upgraded from 500 MeV to 1000 MeV by doubling its length and a corresponding upgrade of the rf and cryogenic systems.

- **The undulator.** The length of the modular undulator must be increased from 10 m to 25 meters by adding further moduls.

- **Civil engineering.** Construction of a 50 m long accelerator tunnel and the experimental hall.

Thus only a relatively modest investment is required to turn the TTF SASE into a world wide unique users facility. If funds will become available in 1997, commissioning could start in 2000.

The proposed facility has not only a world wide unique research programme of its own, but it is also the first necessary step towards the realisation of an X-ray laser facility at Ångström wave length.

1. Introduction

Over the past 30 years synchrotron radiation has turned into a most powerful research tool applied in many different fields of science: in physics, chemistry and biology, in materials sciences, geophysics and in medical diagnostics. This rapid progress was driven by the development of new, increasingly brilliant synchrotron radiation sources installed at electron/positron storage rings. Fig.1.1 shows the time averaged spectral brilliance achieved or expected at various synchrotron radiation facilities. These new research opportunities have been widely used by university groups as well as by scientists from research institutes and industrial laboratories. In a joint effort driven by the facilities and their user communities novel beamline concepts with optical components able to take the large heat load were developed together with highly efficient, high resolution instrumentation. With the new 3rd generation synchrotron radiation facilities in operation, ESRF in Grenoble, ELETTRA in Trieste, SRRC in Hsinchu and the ALS in Berkeley, as well as the facilities under construction in Sweden (MAX II in Lund), in the USA (APS in Argonne), in Japan (Spring 8 in Himeji) and in Berlin (BESSY II), synchrotron radiation research strives for new highlights.

In parallel, recent advances in the development of linear accelerators for large linear colliders considered as the next generation of machines for particle physics, new break throughs in the performance of low emittance electron guns, and in addition the recent successful operation of very precise undulators opens an exciting new possibility to build **Free Electron Lasers (FEL)** based on the principle of **Self Amplified Spontaneous Emission (SASE)**. A **SASE FEL** can in principle produce radiation in the spectral range of the VUV, soft and even hard X-rays without using seed lasers or mirrors. Electron bunches with extremely high power density and low emittance at GeV energies move through a long undulator creating initially in the usual way an intense photon beam at a wavelength λ_0 determined by the electron energy, the magnetic field and the period of the undulator (Spontaneous Emission). Later the electron bunches interact with this electromagnetic radiation field leading to a density modulation with a periodicity equal to the wavelength λ_0, which in turn enhances the power and the coherency of the radiation field emitted by the bunch. This process is called Self Amplification. It starts at some position in the entrance part of the undulator and reaches a saturation value for a given undulator structure. The **SASE FEL** proposed at DESY will be driven by the superconducting **TESLA Test Facility (TTF)** linear accelerator upgraded to 1 GeV and augmented by a low emittance injector and a longitudinal bunch compressor.

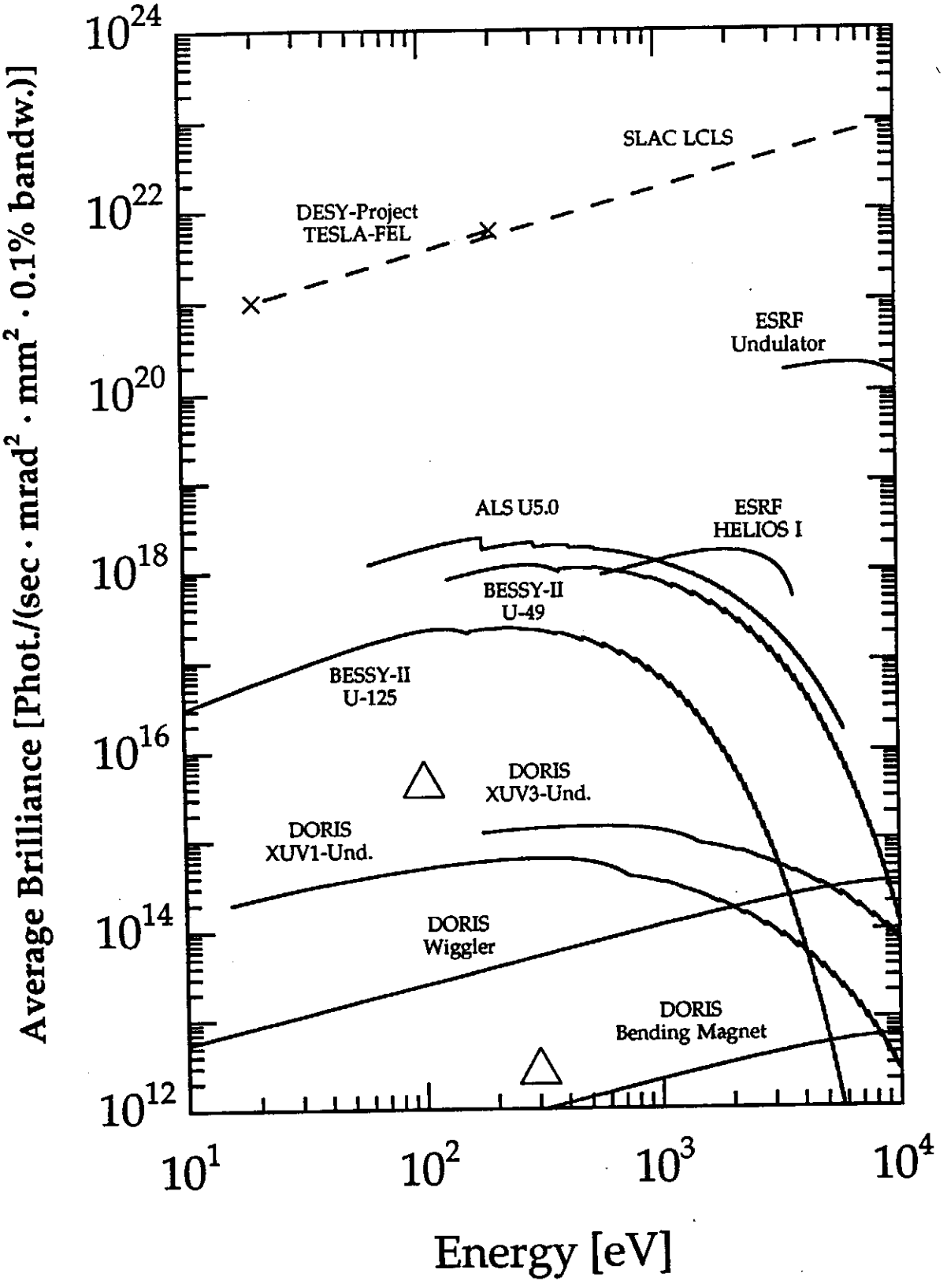

Fig 1.1: Spectral brilliance of the **TTF FEL** in comparison with second and third generation synchrotron radiation sources and the LCLS Free Electron Laser project discussed at SLAC, Stanford, USA. The open triangles represent values achieved with plasma lasers under the optimistic assumption that they can fire once a second.

As shown in Fig.1.1 the average spectral brilliance of such an FEL is by three orders of magnitude higher than the values reached by the new 3rd generation synchrotron radiation facilities operating with low emittance storage rings. The gain in peak brilliance amounts to 7 or 8 orders of magnitude. Fig.1.2 demonstrates the enormous gain in average flux expected for the fundamental line of the **TTF FEL.** Even in the 3rd harmonic, which is located in the so called water window important for microscopy applications in biology, the calculated flux is by almost 2 orders of magnitude higher than that due to the spontaneous emission of the undulator. However, it is not only the high intensity which makes this laser a unique research tool in the VUV and soft X-ray regime, the radiation in the laser line shows a very high degree of transverse coherence, a potential for imaging at short wavelengths which will be explored in the future.

The almost complete polarization of the laser beam and the fast tunability of the photon energy make the source highly attractive to a user community with wide spread interests. Another key feature of the **TTF FEL** is its time structure indicated in Fig.1.3. A comparison of its peak brilliance with that of storage ring based 3rd generation synchrotron radiation facilities is shown in Fig.1.4. The bunch train shown in Fig.1.3 is delivered with a repetition rate of 10 Hz and its internal structure can be modified according to the needs of various experiments. The average length of the individual pulses is approximately 400 fsec (FWHM) and allows for novel time-of-flight experiments, even with photons from the spontaneously emitted spectrum. In addition the individual pulses are expected to show an internal intensity modulation in time which varies from pulse to pulse. Pump and probe experiments with the **TTF FEL** on diluted samples like aligned free atoms or free clusters are most promising.

Fig.1.5 shows the peak power obtained with existing lasers together with the expected values for lasers under construction, or the design values for proposed new machines in the wavelength range from 100 to 0.1 nm. Because of its high peak power at a wavelength of 6.4 nm the **TTF FEL** offers new possibilities to study highly nonlinear physical phenomena. Precautions will be taken which allow a controlled increase of the power density of the beam from the level known from 3rd generation synchrotron radiation facilities to the extreme values typical for the Free Electron Laser. At this point the **SASE FEL** should be put into perspective by comparing its performance with the potential of modern plasma lasers. In terms of peak power the **TTF FEL** at 6.4 nm wavelength will exceed the best plasma lasers available today by about 4 orders of magnitude (see Fig.1.5). Concerning the average spectral brilliance the **TTF FEL** exceeds the plasma lasers by 5 or even 9 orders of magnitude, mainly because of the very low repetition rate of the latter (see Fig.1.1).

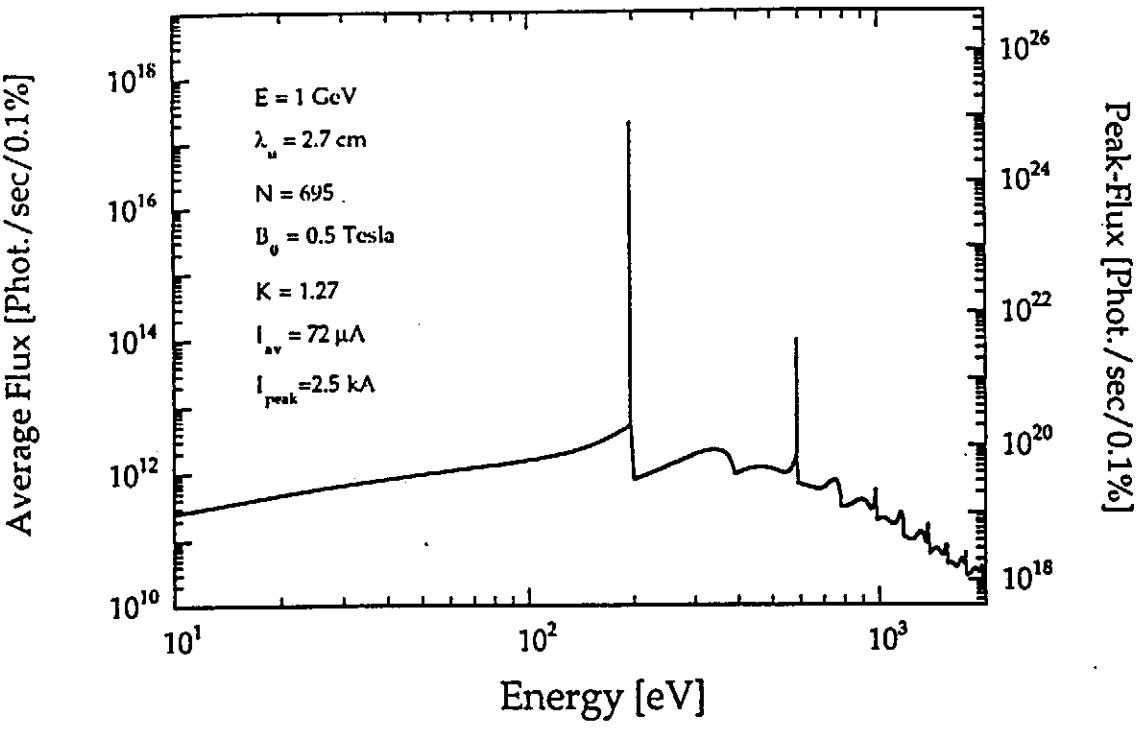

Fig.1.2: Angle integrated photon flux of the **TTF FEL** calculated for its design parameters. The ordinate on the left shows the time averaged flux, the ordinate on the right the peak flux. Note the small spectral width of the delta function like laser radiation compared with the ordinary, spontaneous emission of the undulator.

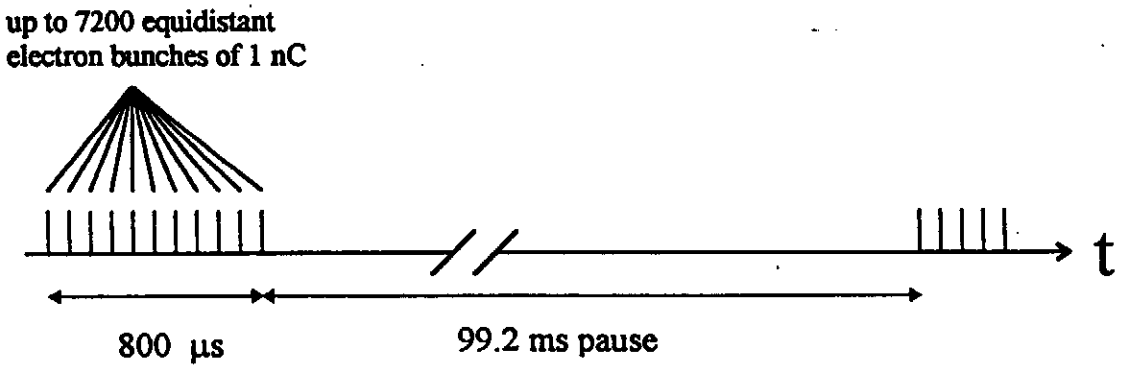

Fig.1.3: Time structure of one bunch train of the **TTF FEL** operating at a repetition rate of 10 Hz. The width of an individual bunch is approximately 400 fsec. The number of bunches in one train can be varied between 1 and 7200.

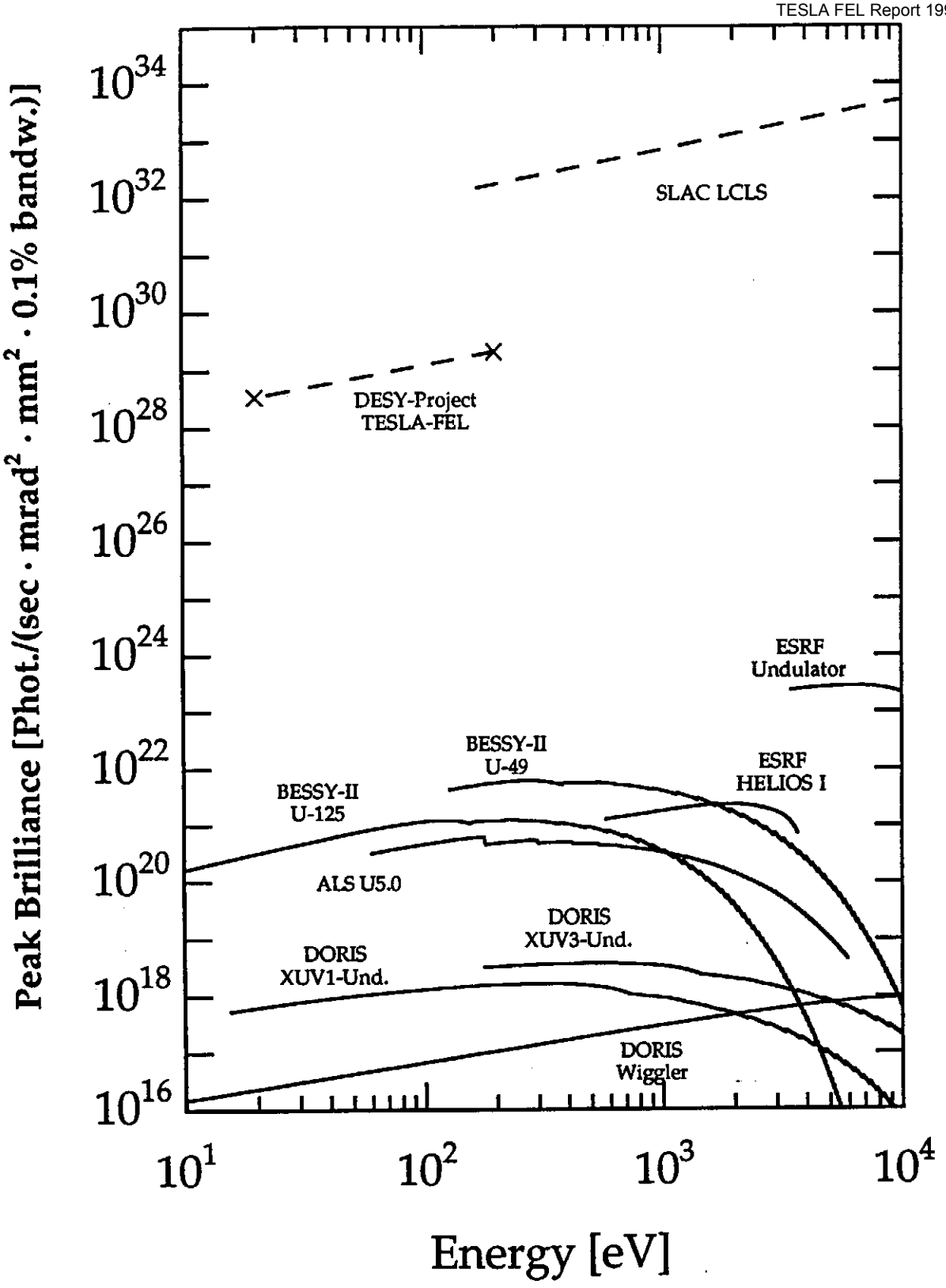

Fig.1.4: Spectral peak brilliance of the **TTF FEL** in comparison with second and third generation synchrotron radiation sources and the LCLS Free Electron Laser project discussed at SLAC, Stanford, USA.

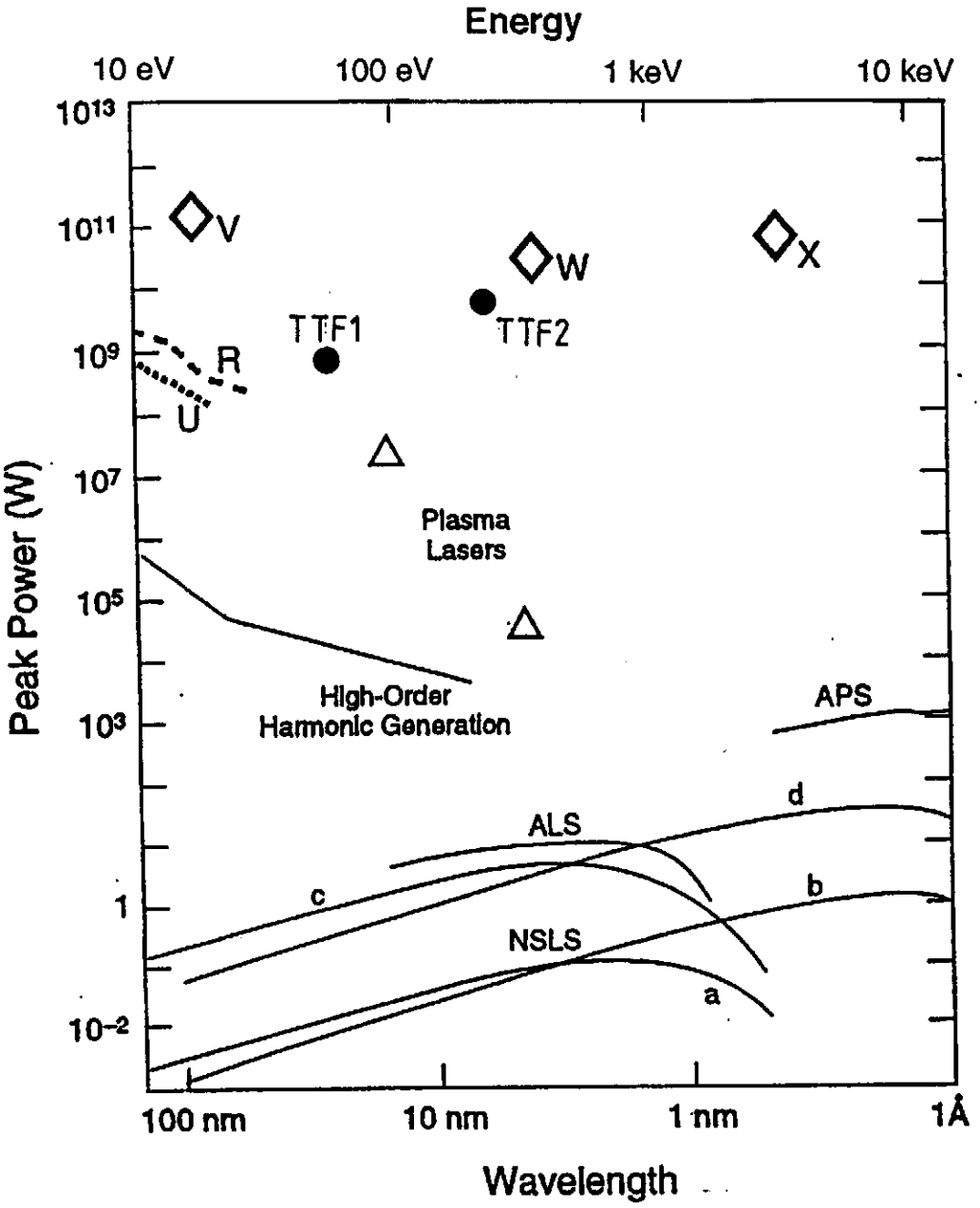

Fig.1.5: Peak power as a function of wavelength for some storage ring based synchrotron radiation facilities and the lasers in operation or under construction in 1994 together with the proposed new facilities according to reference [1]:

R OK4 Optical Klystron at Duke University
U Deep Ultraviolet FEL, Brookhaven National Laboratory [6]
V Chirped Pulse Amplifier FEL, Brookhaven National Laboratory
W Linear Coherent Light Source-1, Stanford Linear Accelerator Center
X Linear Coherent Light Source-2, Stanford Linear Accelerator Center
TTF1 SASE FEL at DESY in its initial phase (500 MeV electrons)
TTF2 SASE TTF FEL at DESY (1 GeV electrons)

Because of the attractive characteristics of a **SASE Free Electron Laser** for the large synchrotron radiation user community, possibilities to realize such machines and their application in various fields of science have been discussed in a number of workshops. The workshop on "Fourth Generation Light Sources" held at SLAC in 1992 [2], which turned out to focus on X-ray lasers, was followed by a meeting held at Brookhaven National Laboratory in 1993 entitled "Towards Short Wavelength Free Electron Lasers" [3]. The scientific case for lasers in the soft and hard X-ray regime has been discussed in two workshops held at SLAC in 1992 [4] and 1994 [5]. In preparation of the scientific case for the **TTF FEL** proposed by DESY a first meeting with potential users took place at DESY in November 1994. Since then working groups for the following fields of application have been formed:

Microscopy
Atoms, molecules, ions and plasmas
Clusters and radicals
Reaction and relaxation dynamics in photochemistry and surface science
High resolution photoelectron spectroscopy of solids
Magnetic materials, dichroism

Summaries of the reports of the working groups are presented in chapter 3. There are interesting suggestions for additional use of the electron beam from the **TTF** Linac, however, interference with the FEL experimental program has to be avoided.

Some of the proposed FEL experiments will use the direct beam. However, most of the experiments require optical elements to focus or diffract the photon beam of extremely high power density. The search for the best mirror material and optimal beamline geometries therefore plays a major role in the required R&D work together with the design of a high resolution monochromator which can accept the high power load. To make full use of the **TTF FEL** large efforts have to be made to develop fast detectors with high spatial resolution and appropriate data acquisition systems. Here the experience of the particle physics detector community at DESY will be very helpful.

To build a **Free Electron Laser** based on the **SASE** principle as well as the development of beamline components and instrumentation represents a real challenge. A number of innovative steps have to be made to make this project, which leads future synchrotron radiation research beyond the limits of 3rd generation storage rings, a success. DESY, with its outstanding expertise in accelerator physics and its long standing experience in synchrotron radiation research, covering the spectral range from the visible to photon energies of 300 keV, is the ideal place in Europe to construct and operate this demanding facility in close collaboration with the user community. It is

also a first and necessary step towards the dream of realizing a true X-ray laser operating at 1 Ångstrøm, the natural scale for atomic and condensed matter phenomena.

References

1 Report of the Committee of the National Academy of Sciences on *Free Electron Lasers and Other Advanced Sources of Light,* National Academy Press, Washington, DC, 1994, USA.

2 *Workshop on Forth Generation Light Sources*, M. Cornacchia and H. Winick (editors); SSRL report 92/02, Feb 24-27, 1992.

3 Report on the *Workshop Towards Short Wavelength Free Electron Lasers*, I. Ben-Zvi and H. Winick (editors), Brookhaven National Laboratory, May 21-22, 1993; BNL Report 49651.

4 *Workshop on Scientific Applications of Short Wavelength Coherent Light Sources*, W. Spicer, J. Arthur and H. Winick (editors), SLAC Report 414, 1992.

5 Workshop on *Scientific Applications of Coherent X-rays*, J. Arthur, G. Materlik and H. Winick (editors), SLAC Report 437, 1994.

6 Conceptual Design Report (Volume I) on the *DUV Free Electron Laser: A Fourth Generation Source in the Vacuum Ultra-Violet*, Brookhaven National Laboratory, January 1994, BNL Report 49713.

2 Overview

2.1 Outline

The Free Electron Laser at the TESLA Test Facility (TTF FEL) is based on the principle of „Self Amplified Spontaneous Emission = SASE" [1]. The key advantage of the SASE scheme (as will be discussed in some more detail in chapter 11) compared to other FEL schemes is that neither an input seed laser nor mirrors forming an optical cavity is required. Thus no known fundamental limitation would prevent operation even down to the Ångstrom region. In the first section of the undulator the electrons radiate independently and the phases of the photons are randomly distributed. Since microbunch formation starts from this „random" noise, a long undulator is needed to achieve laser action with exponential growth in light output, see Figure 2.1. For the TTF FEL an overall undulator length of 30 m is planned.

It is not the aim of this general introduction to present or discuss the theory of SASE FELs, which can be found in text books and journal articles, e.g. [2], [3]. Instead, the motivation for the choice of basic design parameters will be presented together with the proposed method of realization.

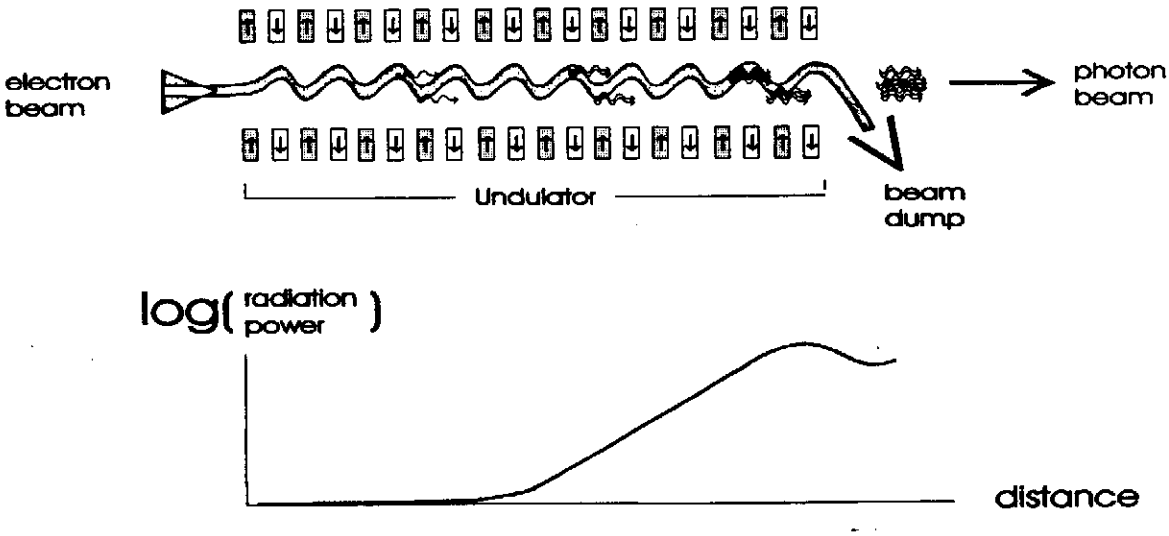

Figure 2.1: Schematic drawing of an FEL operating in the „Self Amplified Spontaneous Emission = SASE" mode. The peak current in the electron bunch is very high and the undulator is long enough, so that power saturation is reached during a single passage starting from noise.

The photon wavelength λ_{ph} of the first harmonic is related to the period length of a planar undulator λ_u by

$$\lambda_{ph} = \frac{\lambda_u}{2\gamma^2}\left(1+\frac{K^2}{2}\right) \quad , \qquad (1)$$

where, $\gamma = E/mc^2$ is the relativistic factor of the electrons and $K = e B_u \lambda_u / 2\pi mc$ the „undulator parameter", e being the elementary charge, m the electron rest mass, c the speed of light, and B_u the peak field in the undulator.

The physics program for the TTF FEL requires a photon wavelength of 6 nm. Therefore, a value $\gamma \approx 2000$ (i.e. 1 GeV beam energy) is necessary, see eq. (1), if state-of-the-art undulator parameters are assumed, e.g. $\lambda_u = 27$ mm, $K = 1.3$. Note that a much smaller K parameter would not result in a much smaller required electron energy, but it would reduce the radiated power substantially.

Two beam parameters are essential to reach power saturation within a not too long undulator: A small transverse beam emittance ε_t to provide both small beam diameter and small beam divergence in the undulator, and a small longitudinal beam emittance ε_z to achieve kilo-Ampere instantaneous beam currents at an energy width in the 0.1% range.

The superconducting (s.c.) linear accelerator currently under construction at DESY („TESLA Test Facility" = TTF) is an ideal accelerator to drive a SASE FEL. There are two main reasons:

- The perturbation of small emittance beams during the acceleration process is smallest with a superconducting linac at lower frequency. Because the resonator volume and the stored energy are large, the accelerating field is hardly affected by the presence of the electron beam. The variation of the effective accelerating voltage over the bunch length („longitudinal wakefield") is minimal and the magnitude of beam induced rf deflections („transverse wakefields") is small.

- A superconducting linac provides a large AC power efficiency and a high duty cycle. The wall plug to electron beam power efficiency can be as high as 30 % with a CW s.c. linac. This number reduces to a still very attractive 20 % if the linac is pulsed with a high accelerating gradient, which is economically more favorable if a large electron energy is desired, because it saves investment costs in tunnel length and rf components. The TESLA Test Facility will operate at 1 % duty cycle, orders of magnitude larger than a normal conducting linac would do at the TTF nominal gradient of 15 MV/m. Besides power efficiency, this is a crucial advantage for potential experiments, because it leaves sufficient time between pulses in the bunch train for data handling.

Finally, it should briefly be mentioned, why a linac is considered much more suitable for driving the proposed FEL than a storage ring. Going to shorter and shorter photon wavelengths requires smaller and smaller electron beam emittance (see eq. (2)). While in a linac the transverse beam emittance automatically decreases in parallel with energy due to the so-called adiabatic damping, the storage ring emittance is determined by quantum fluctuation which *increases* with energy. Also, kilo-Ampere peak currents would be extremely hard to achieve in a storage ring due to the microwave instability. As a consequence, a SASE FEL cannot be driven within a storage ring at beam energies above about 1 GeV.

The most expensive single component of a short wavelength FEL is the accelerator. Taking into account, that a SASE FEL needs beam parameters similar to those to be

realized for a Linear Collider, it is obvious that the TTF linac can be ideally utilized for driving a SASE FEL. For the discussion of the TESLA Test Facility linac and its relation to the TESLA 500 Linear Collider scheme we refer to the TTF Design Report [4].

The TTF design energy is 500 MeV. It has to be upgraded to 1 GeV electron beam energy required for the desired photon wavelength. Figure 2.2 shows the overall TTF FEL scheme.

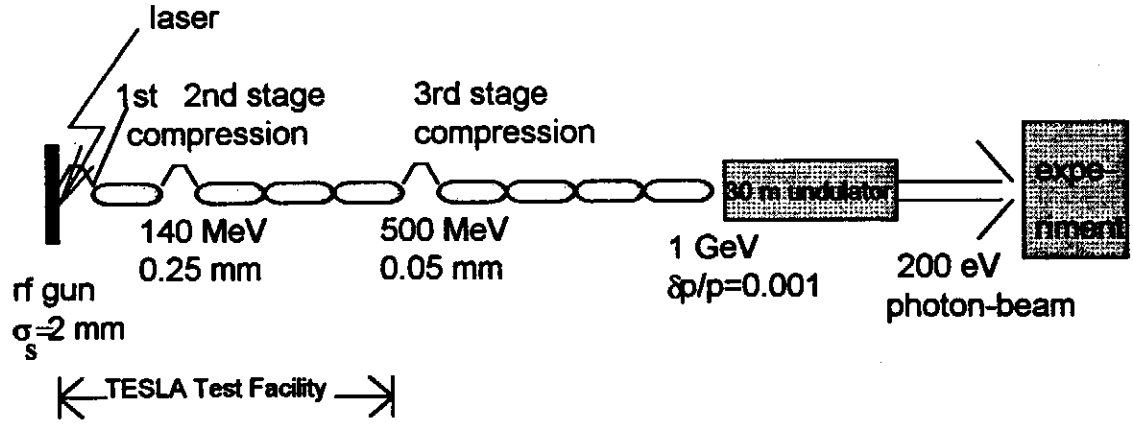

Figure 2.2: Schematic layout of the TTF FEL based on the TESLA Test Facility (TTF). Four additional TESLA accelerator modules bring the energy up to 1 GeV. The bunch length is reduced from 2 mm to 50 μm within three steps of bunch compression. The SASE FEL process requires an undulator of 30 m length. The overall length of the facility is some 200 meters.

2.2 Electron Source

The transverse coherence condition imposes a tight requirement on the transverse emittance ε_t of the electron beam [2]:

$$\varepsilon_t = \frac{\varepsilon_t^n}{\gamma} \leq \frac{\lambda_{ph}}{4\pi} \qquad (2)$$

ε_t^n is the *normalized* emittance which is the quantity conserved during acceleration according to Liouville's Theorem. For $\lambda_{ph} = 6$ nm, $\gamma = 2000$, this requires $\varepsilon_t^n < 1\ \pi$ mrad mm[1]. Actually, as will be discussed in chapter 11, this condition is not very strict, but the saturation length significantly increases if ε_t^n is larger. Thus, we aim at $\varepsilon_t^n = 1\ \pi$ mrad mm for the rms electron emittance of a 1 nC bunch charge from the electron gun, and we allow for a factor of two emittance dilution during longitudinal beam compression and acceleration up to 1 GeV. According to beam dynamics simulations in both the bunch compressors and the accelerator, this seems to be a conservative assumption, see chapters 6 and 8.

[1] The factor π is only included in the dimensions to indicate that the numerical value of the emittance (in the present case 1) does *not* include π. Following common practice, we nevertheless omit the factor π in formulae describing the beam size etc., i.e. we write $\sigma=\sqrt{\varepsilon_t \beta}$, instead of, in a mathematically rigorous way, $\sigma=\sqrt{\varepsilon_t / \pi \cdot \beta}$.

These very high phase space densities came within reach due to two major achievements: The development of the rf gun [5] and the concept of space charge compensation [6]. While $\varepsilon_t^n = 3\ \pi$ mrad mm (at 1 nC) can be considered state of the art [7], an improved rf gun design with smaller emittance will be discussed in chapter 5. It is most likely that the TTF FEL rf gun will be able to use many components of the rf gun of the TTF Injector II, which is designed for a larger bunch charge so that it cannot directly meet the FEL emittance requirements [4]. This would save investment costs of the most expensive parts, e.g. laser, klystron, and modulator.

It is stressed that development of and diagnostics for low emittance beams goes directly in parallel with R&D on Linear Colliders.

2.3 Longitudinal Bunch Compression

As mentioned before, a very high instantaneous beam current is needed in the undulator to reach photon power saturation within a reasonable undulator length. For the TTF FEL, this number is 2500 A, corresponding to 50 μm rms bunch length for a 1 nC bunch charge. This value is not attainable directly from the electron gun, because space charge forces would blow up both the transverse beam size and the momentum spread. Thus, the use of magnetic bunch compression is foreseen in order to reduce the rms bunch length from 2 mm in three steps down to 50 μm.

In principle one could consider performing the bunch compression in one step at an energy level, where space charge is not critical any more (> 300 MeV or so). However, even at the comparatively low TTF rf frequency, the cosine-like time dependence of the accelerating field would then impose an intolerable nonlinear correlated energy distribution along the bunch, see chapter 6. The proposed solution is to perform compression in three steps at 22 MeV (2 mm → 0.8 mm), 140 MeV (0.8 mm → 0.25 mm) and 500 MeV (0.25 mm → 0.05 mm).

It is worth noting that recently rms bunch length measurements of 15 μm have been reported (but only at 1/20 nC) [8], and that multi-nC bunch compression below 100 μm is an objective of the Accelerator Test Facility under construction at KEK, Japan [9] because it is an essential component of future Linear Colliders.

2.4 Acceleration

As the high TTF bunch charge of 8 nC is associated with an intolerably large emittance, the FEL operation is based on 1 nC bunches. Since from the rf point of view only the average beam current $\langle I_b \rangle$ during the rf pulse and the total beam loaded rf pulse length T_{rf} matter, it is proposed to keep both parameters approximately constant: $\langle I_b \rangle = 9$ mA, $T_{rf} = 800$ μs. Due to the master clock frequency of 9 MHz, a bunch to bunch distance of 1/9 μs is chosen, so that a total of up to 7200 bunches will be accelerated per rf pulse. The TTF FEL pulse structure is sketched in Figure 2.3.
For the bunch compression an rf phase adjustment off the crest is needed to provide the necessary correlated energy distribution along the bunch. Finally, it might be important for the FEL users, to tune the beam energy from pulse to pulse. All of these modifications do not need any major change of hardware.

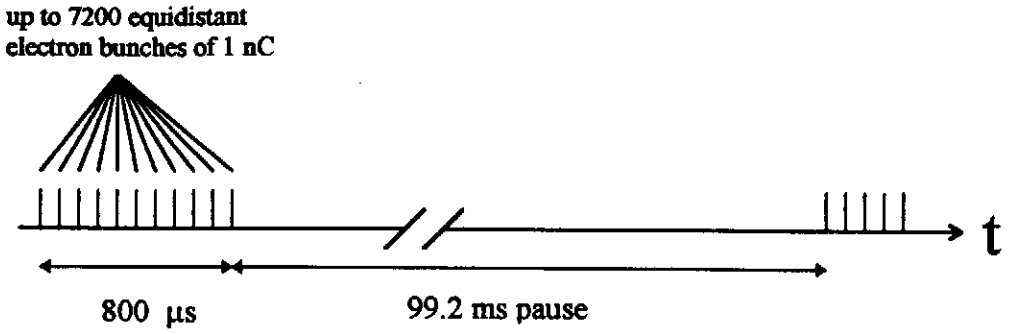

Figure 2.3: TESLA FEL pulse structure

2.5 Undulator

The undulator is the most prominent FEL specific component. Several designs, including superconducting helical undulators, pure permanent magnet undulators, hybrid structures of electromagnetic and permanent magnets, and planar hybrid undulators have been considered. The proposed design is motivated by the request to avoid technical risks. Thus, a planar hybrid undulator is foreseen with period length λ_u = 27 mm and peak magnetic field B_u = 0.5 T, parameters very much like those of existing undulator magnets. The main challenges are the total length of 30 m, the additional quadrupole focusing to be supplied and tight tolerances. To simplify production, measurement and installation, a modular construction method is proposed. This also permits electron and photon beam monitors and correction elements to be installed between subsequent modules of approx. 5m length each.

2.6 FEL Process

Various computer codes have been used to investigate the start-up from noise, and the lethargy, exponential and saturation regimes, respectively, e.g. NUTMEG [10], FS2R[11], TDA[12], GINGER[10]. There is now a common understanding among the experts, that the SASE FEL physics is sufficiently well understood (both numerically and analytically) to provide a realistic and reliable basis for the design of a SASE FEL facility. This is also illustrated by the fact that there is no essential disagreement between results of all the previously mentioned codes written by different groups and based on different approaches.

A peculiar characteristic of the SASE FEL is the strong spiking both in the temporal and spectral domain of the emitted radiation. It is a consequence of longitudinal subsections inside each electron bunch radiating at statistically independent phases, if the start-up is from noise instead of being „seeded" by an external radiation field of high longitudinal coherence (i.e. by a „seed laser"). As a consequence, one expects large fluctuations of the instantaneous radiation power distribution inside each radiation pulse, changing from pulse to pulse, while the radiated power averaged over each pulse will be quite stable. As seeding at 6 nm is impossible due to lack of lasers, schemes generating harmonic content of the longitudinal electron density modulation at (roughly) the 40th harmonic of a

conventional laser could be considered (multiple stage harmonic generation [13]). Further studies on these schemes are desirable, but they are presently not proposed for the TTF FEL, because the TTF FEL aims at establishing the SASE mechanism for short wavelengths in order to pave the way for an Ångstrøm FEL, on which the multiple stage harmonic generation scheme is even more unlikely to be applicable.

Semi-analytical formulae have been used to investigate the parameter space [14]. The final parameter optimization and determination of tolerances has then been performed using numerical codes. This will be discussed in chapter 11. The resulting parameter list is shown in Table 2.1. Figures 1.1 and 1.2 (see chapter 1) illustrate, respectively, the average and peak spectral brilliance expected from the TTF FEL in comparison with second and third generation synchrotron radiation sources.

VARIABLE	UNITS	VALUE
beam energy	GeV	1.000
λ(radiation wavelength)	nm	6.4 (193 eV)
λ_u (undulator period)	mm	27.3
undulator gap	mm	12
B (undulator peak field)	T	0.497
undulator length	m	30
β beam optics beta function	m	3
rms beam size	mm	0.05
ε^n (normalized emittance) in the undulator	π mrad mm	2.0
peak electron beam current	A	2490
number of electrons per Gaussian bunch		6.24E+9
number of photons per Gaussian bunch		4E+13
peak electron beam power	GW	2490
energy spread σ_γ/γ	10^-3	1.00
bunch length	μm	50.
L_g (power gain length)	m	1.00
L_s (saturation length)	m	< 25
P_{sat} (saturated power)	GW	3
average brilliance	photons/s/mm^2/mr^2/0.1%	up to 6E+21
bunch train length	μsec	800
number of bunches per train		up to 7200
repetition rate	Hz	10

Table 2.1: Main parameters of the TESLA Test Facility FEL (TTF FEL). The insertion device is assumed to be a planar hybrid undulator.
These values should be used as a guideline only since the optimization has not yet been finished and experimental experience has to be gained in this wavelength regime.

2.7 Civil Engineering, Shielding and Safety

In addition to the existing TTF hall, a 70 m long tunnel to accommodate the additional accelerator modules and the undulator has to be built. Also, an experimental hall for potential users of the photon beam is needed. Due to the high average beam current in the TTF linac, heavy shielding is necessary. The bremsstrahlung shower moving along with the photon beam into the part of the experimental hall that is in the direction of the linac beam line requires shielding with loaded concrete. This will be discussed in chapter 12. Figure 2.4 shows the overall layout of the TESLA FEL installation on the DESY site.

2.8 TTF FEL Phase 1

According to the present schedule, the TESLA Test Facility will go into operation in mid 1997. This opens up the possibility of a first test at wavelengths larger than 25 nm, corresponding to beam energy below 500 MeV. With a test in the wavelengths regime between 25 and 100 nm, beam requirements are considerably relaxed, so that an emittance of $\varepsilon_x^n = 3\ \pi$ mrad mm (at 1 nC bunch charge) could be tolerated, and the final bunch compressor is not needed.

It should be noted that probably even in the year 1998 no self-stimulated FEL will be operational in this wavelength regime elsewhere, so that it will be highly desirable to learn about the validity of codes and theories at these wavelengths as early as possible. Also, experience with electron and photon beam diagnostics would make it possible to improve the equipment while the energy upgrade is installed. No operation for users is foreseen during phase 1 operation.

The main components that need to be installed after phase 1 are:
1) four additional TESLA accelerator modules
2) the final bunch compressor unit
3) the experimental hall

The undulator and the beam dump should be installed at the final position to avoid major reconstruction.

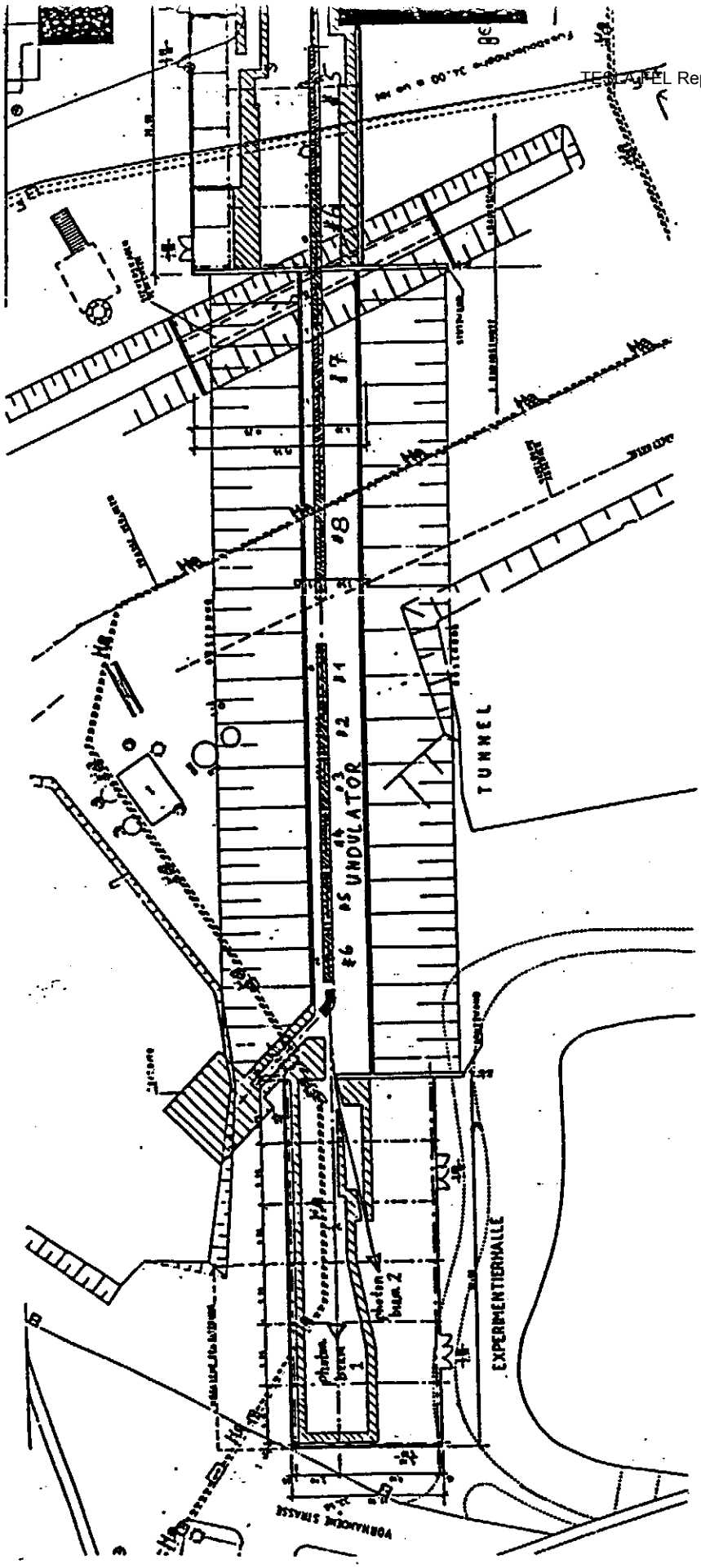

Figure 2.4: Layout of the TTF FEL installation on the DESY site.

2.9 Milestones

The following milestones are foreseen along the way to building the TTF FEL:

Electron acceleration by first TESLA Module	end of 1995
Start operation of TESLA Test Facility at 500 MeV	end of 1997
SASE FEL tests at the TESLA Test Facility with $E \leq 500$ MeV (TTF FEL Phase 1)	during 1998
Installation of TESLA Modules No. 5-8 and of full size undulator	1998 - 1999
Start commissioning of TTF FEL at 1 GeV	2000

References:

1 R. Bonifacio, C. Pellegrini, I.M. Narducci: Opt. Commun. **50** (1984) 373.
2 W.B. Colson, C. Pellegrini, A. Renieri (eds.): Laser Handbook Vol. 6, North Holland (1990)
3 K.J. Kim, M. Xie: Nucl. Instr. Meth. A, **331** (1993), 359.
4 D.A. Edwards (ed.): TESLA Test Facility Linac - Design Report, TESLA 95-01 (1995)
5 J. Fraser, R. Sheffield: Nucl. Instr. Meth. A 250 (1986) 71
6 B. Carlsten: Nucl. Instr. Meth A 285 (1989) 313
7 C. Travier: Proc. EPAC 94 London (1994) 317
8 P. Kung, H.-C. Lihn, H. Wiedemann: SLAC-Pub-6507 (1994)
9 F. Hinode, et al. (eds.): ATF Accelerator Test Facility Design and Study Report, KEK (1995)
10 E.T. Scharlemann: in Ref. 2
11 E. L. Saldin, E.A. Schneidmiller, M. V. Yurkov: DESY Report 94-219 (1994)
12 C.-M. Tran, J.S. Wurtele: Comput. Phys. Commun. 54 (1989) 263
13 L. Serafini, M. Ferrario, C. Pagani, A. Peretti: SHOK: Sub-Harmonic High-Gain Optical Klystron, INFN/TC-90/11 (1990)
14 K.J. Kim, M. Xie: Nucl. Instr. Meth. A, 331 (1993) 359

3. Scientific Applications

3.1. Introduction

The TTF-Free-Electron-Laser will be a unique light source which emits radiation up to photon energies of about 200 eV in the first harmonic.

The average values of brilliance and photon flux are about three orders of magnitude higher than those of third generation synchrotron sources like BESSY II, ALS and ELETTRA. The peak values are more than eight orders of magnitude higher. Of special advantage are the high degree of linear polarization, the extremely short pulse length, the high peak brilliance, the fast tunability of the photon energy and the transverse coherence.

The unique properties of the TTF-FEL radiation will open up new and exciting areas of basic and applied research in a number of disciplines from biology, chemistry to physics. For example, the high-peak-output power will be used to induce nonlinear physical phenomena, measure the opacity of plasmas, diagnose short-lived events in dilute media and provide microscopic snapshots of temporally unstable targets. The first series of test experiments, especially on dilute gaseous samples can use the photon beam as emitted by the TTF-FEL. But later on most experiments will require monochromatization and focusing or defocusing of the TTF-FEL beam. The development of optical elements capable of withstanding the high power VUV-laser radiation is a great challenge which will stimulate the VUV optics technology. Pump and probe, the ideal method to fully exploit the extremely short pulses for dynamical studies will require the stable synchronization of lasers with the TTF-FEL.

Areas of research expected to greatly profit from the TTF-FEL encompass:
Atomic and Molecular Spectroscopy; Spectroscopy of Ion Beams; Ionized Gases and Plasmas, Spectroscopy of Atomic and Molecular Clusters; Solid State Spectroscopy; Physics and Chemistry of Surfaces and Thin Films; Photochemical Processes; Biological Structure and Dynamics. In material science the TTF-FEL will be a very valuable tool in the study of : Materials and Surface Processing, Multilayer Magnetic Films, the Electronic Structure of Semiconductors, Heavy Fermion Materials and High Temperature Superconductors and the Dynamics of Catalytic Reactions.

The detection of the number, energy angular distribution, polarization of the outgoing fragments, ions, electrons, and photons as a function of the number, energy and polarization of the incoming TTF-FEL photons will grant very detailed information on the photon induced processes. Dilute systems, multicoincidence techniques and pump and probe experiments are accessible with the TTF-FEL.

In order to fully exploit the high quality of the TTF-FEL photon source new experimental techniques based on the most advanced optical elements, detectors and electronics have to be developed, a formidable challenge to the experimentalists.

3.2. Areas of Research

3.2.1 X-ray Microscopy and Microspectroscopy

a) X-ray microscopy

X-ray microscopy provides higher resolution than optical microscopy and deeper penetration capability than electron microscopy and allows the investigation of thick hydrated samples. The two dominating processes determining the contrast in x-ray microscopy performed with soft x-rays are photoelectric absorption and phase shift. The wavelength range between the K-absorption edges of oxygen (λ = 2.34 nm) and carbon (λ = 4.38 nm) is especially interesting because in this wavelength range the radiation is weakly absorbed by water but strongly absorbed by organic or anorganic matter resulting in a good amplitude contrast of a wet specimen. This wavelength range is called the "water window" [1]. In addition to the amplitude contrast, caused by photoelectric absorption , phase contrast can also be used for X-ray microscopy experiments [2]. Phase contrast experiments performed with x-ray wavelengths in the water window give considerably improved image contrast and lower dosages. In addition, phase contrast allows to perform high resolution experiments in the shorter wavelength range of about λ = 0.3 nm.

Up to now, different types of microscopes have been developed, namely transmission x-ray microscopes, scanning transmission x-ray microscopes and photoelectron x-ray microscopes for spectromicroscopy. Detailed information on the state of the art can be found in the proceedings of symposia on x-ray microscopy held in Göttingen in 1983, Taipei in 1986, Brookhaven in 1987, Toshigi in 1988, London in 1990, S. Diego in 1992 and in Chernogolovka / Moscow in 1993 [3-9]. The best spatial resolution obtained up to now in x-ray microscopy is $\leq$ 30 nm using micro zone plates as high resolution x-ray lenses. One reason for this is that aberrations of high resolution x-ray optical elements scale with their dimensions and grazing incidence or normal incidence x-ray mirrors are considerably larger than micro zone plates with diameters of about 50 μ.

X-ray microscopy is used in different fields, e.g. in biology, biophysics, medicine, colloid chemistry, soil sciences. In a recent paper [10] many applications are put together, including investigations on chromosomes, malaria infected erythrocytes, calcified tissues, sperm, muscles, macrophages, lipid membranes, polymers and polymer blends, soil colloids etc.

It is known from theoretical investigations and measurements that the dose applied to the sample increases inversely to the fourth power of the resolution. In biological objects investigated with high resolution the applied dose can cause structural changes and especially in wet biological systems, can alter the inital element distribution.

Therefore, artefacts visible in the x-ray image can occur, especially if multiple images are taken in order to get three-dimensional image information. These difficulties can be overcome by 1.) cryo x-ray microscopy and/or 2.) imaging with very short pulses.

Cryo-x-ray microscopy : At the BESSY x-ray microscope a cryogenic object chamber has been implemented and a first series of experiments has been performed using initially live algae [11]. The algae have been irriadiated over a long time with an accumulated photon density of about 10^{12} photons / μm^2 corresponding to a dose of about 10^{10} Gy. No structural changes were observed. The conclusion is that the cryo method will allow to image chemically unfixed specimen with a resolution $\leq$ 10 nm. Furthermore, the high stability of vitrified objects will allow to take mulitple images for three dimensional image formation.

Imaging with very short pulses-FEL radiation : Is it possible to take a high resolution image of initially live, unfixed biological specimen with one pulse of the FEL ? The answer is yes and is based on experimental results obtained with the x-ray microscope at BESSY and with an x-ray microscope with a pulsed plasma source :

To image a 25 nm protein structure in a ten μm water layer with a wavelength of 25 nm in phase contrast one needs a photon density in the object of about 2.7×10^8 photons/μm^2 corresponding to a dose of 2.7×10^6 Gy. To get this photon density it is necessary to focus a beam with an energy of several μJ onto an area of about 10 x 10 μm^2. Because of the high power density in the irridiated part of the object this part will be destroyed but the exposure time of 400 fs is much smaller than the time scale of hydrodynamic motion which is in this case about 50 ps [12]. The x-ray optical set up can consist of a grazing incidence optical system to enlarge the divergence of the beam, an x-ray condenser, a high resolution micro zone plate downstream of the object and CCD-camera. In addition one can think of a two zone plate set up to get stereoscopic images with one pulse of the FEL. It should be mentioned that it is necessary to do the experiments with a wavelength in the "water window", so FEL-radiation is necessary with a photon energy of about 500 eV and $\Delta E/E = 10^{-3}$.

b) Microspectroscopy and Spectromicroscopy

There are different ways to obtain spectroscopic information in the soft X-ray region. The first method is to scan the primary photon energy continously especially through thresholds of primary excitations. This method is called excitation spectroscopy. Element specific information and in favourite cases information about the chemical environment is obtained. With the other method, which is called secondary spectroscopy, the emitted secondary particles following the absorbtion process are selected with respect to their kinetic energy (photoelectrons), wavelength (luminsecence, fluorescence) or mass (ions).

The combination of these techniques with spatial information in the submicron range is called microspectroscopy. There are presently two methods for microspectroscopy. The first method relies on the illumination of a restricted sample area with high photon

density. Electrons (one day may be also photodesorbed ions) are imaged and at the same time selected with respect to their kinetic energies [13, 14] .

It is obvious, that high magnification and high selectivity can profit from the highest photon density tolerable on the sample. The second method is connected with scanning microscopy, where a small spot of light is generated by optical components, as there are: Fresnel zone plates [15], Bragg-Fresnel optics, normal incidence mirrors with single- (< 30 eV) and multilayer coatings (> 50 eV) [16], grazing incidence mirrors [17] and capillaries [18]. With this technique primary as well as secondary spectroscopy can be performed without the need of imaging spectrometers. It turned out that a single grazing incidence ellipsoid mirror has the greatest flexibility since it reflects the incoming light over a wide range of energies [19].

The scanning microscopy at HASYLAB is of that type and is presently limited in resolution by the quality of the optical elements. It is, however, foreseeable that, once this problem is solved, the next limitaion will be the flux in the focal spot. Already now some secondary processes cannot be observed with present day resolution. The processes which are available in principle are the following:

1. transmission
2. reflection
3. stray light
4. total photoelectric yield
5. energy resolved photoelectric yield
6. angle resolved photoelectric yield
7. visible and UV luminescence with spectral resolution
8. X-ray fluorescence with spectral resolution
9. photon stimulated ion desorbtion with time of flight mass spectroscopy

The processes 1-7 have already been installed and used for imaging. The processes 8 and 9 have too low intensities for this purpose. Nevertheless they are of great interest in surface and interface analysis. X-ray fluorescence is one of the rare processes which has enough escape depth to analyse buried interfaces, a field of great interest in applied problems.

The TTF-FEL will be of considerable importance to open up these two channels for analysis. While all the processes listed above can profit from higher flux on the sample, provided that the detectors will be developed to take full advantage of the expected high signals with a low duty circle, the latter two processes will probably be brought above the threshold of practical applications. Even at light sources of the third generation the flux is presently marginal for getting ion desorbtion and X-ray fluorescence spectroscopy combined with high spatial resolution. Not to mention that this has not been done up to now even with low resolution!

There is one problem which should be addressed. Mechanical scanning of the sample can be done with the TTF-FEL but it has to be synchronized with its pulse structure, which results in a limited speed. The present scanning stages and transition times for

one pixel to the next is larger than 1 msec. Since the duty cycle leaves "holes" between pulse trains of 9 msec it is also questionable wether or not there is much advantage to try to push up the speed with which a sample can be moved. It is therefore probably correct to envisage a type of investigation where first an overview over 1000 to 10000 pixels is produced in 2-15 min. Then a fast spectroscopic analysis with high accuracy of selected points on the sample can follow.

The detection problem for desorbed ions can be solved by large drift paths and multichannel detectors separating the counts of different species and also those of a single type of ions.

For soft x-ray fluorescence spectroscopy a disperging grating spectrometer with multichannel detection, may be on the basis of a charge coupled device, will be needed.

The destructive power of the high intense microspot on the sample will differ with different types of samples and problems. The intensity has either to be kept below that limit or a mode where a single 500 fsec pulse can be produced every 100 msec combined with a scan to a non-illuminated part of the sample needs to be applied.

References:

1. H. Wolter, Spiegelsysteme streifenden Einfalls als abbildende Optiken für Röntgenstrahlen, Ann. Phys. 6. Folge 10(1952) 94-114.

2. G. Schmahl et al., Phase contrast studies of biological specimen with the x-ray microscope at BESSY, Rev.Sci. Instrum. 66(2) (1995) 1282-1286.

3. G. Schmahl, D. Rudolph (Eds.), X-ray Microscopy. Springer Series in Optical Sciences, Vol. 43, Springer Verlag, Berlin (1984).

4. P.C. Cheng, G.J. Jan (Eds.), X-ray Microscopy-Instrumentation and Biological Applications. Springer Verlag, Berlin (1987).

5. D. Sayre et al. (Eds.), X-ray Microscopy II, Springer Series in Optical Sciences, Vol. 56, Springer Verlag, Berlin (1988).

6. K. Shinohara et al. (Eds.), X-ray Microscopy in Biology and Medecine. Japan Scientific Societies Press, Tokyo, Springer Verlag, Berlin (1990).

7. A.G. Michette et al., X-ray Microscopy III, Springer Series in Optical Sciences, Vol. 67, Springer Verlag, Berlin (1992)

8. C. Jacobsen, J. Trebes (Eds.), Soft X-ray Microscopy, SPIE Vol. 1741 (1992).

9. V.V. Aristov, A.I. Erko (Eds.), X-rayy Microscopy IV, Bogorodski Pechatnik Publishing Company, Chernogolovka, Moscow Region (1995).

10. J. Kirz et al., Soft X-ray Microscopes and their Biological Applications, Quarter

ly Review of Biophysics (1995), in press.

11. G. Schneider et al., Cryo X-ray microscopy, Synchrotron Radiation News (1995), in press.

12. R. London et al., The role of X-ray induced damage in biological micro-imaging, in ref. 8, p. 333-340.

13. Tonner, B.P., Nuclear Instr. Meth. A 291, 60 (1990).

14. Pienetta P., King P. et al, J. Electron Spectros. Relat. Phenom. 52, 797 (1990).

15. Ade H., Kirz J. et al, Appl. Phys. Lett. 56, 1841 (1990)

16. Cerrina F., Margaritondo G., Underwood J.H. et al, Nucl. Instrm. Meth. A 266, 303 (1988)

17. Voss J. et al., J. X-ray Science Technology 3, 85 (1992)

18. Bilderback D.H., Hoffmann S.A., Thiel D.J., Science 263, 201 (1994)

19. Kunz C. and Voss J., Rev. Sci. Instrum. 66 (2), 2021 (1995)

3.2.2. Single and Multiphoton Excitation Dynamics of Atoms and Ions

The photon energy range covered by the TTF-FEL encompasses the excitation energies of the valence-, subvalence- and outer high -l core shells of the free atoms throughout the periodic table and of many ions. This includes the giant 3p-3d and 4d -> 4f/εf resonances of the 3d metal series, the rare earths and the elements preceding and following these series. Due to their easy amenability to experimental and theoretical studies, the rare gas atoms will continue to play a key role in the investigation of the atomic many electron dynamics. The subvalence and outer core shell spectra display dramatic deviations from the predictions of independent particle models caused by the strong coupling between many closed and open channels. The field of vacuum ultraviolet spectroscopy of rare gas atoms and metal atoms has recently been reviewed [1,2]. Many electron correlations and the excitation and deexcitation dynamics will continue to be the focus of the investigations. However, the short pulses and the high power density ($> I_0$ = au = 3.5 x 10^{16} W/cm^2) achievable with the TTF-FEL add new dimensions to the field. In recent years the interaction of very strong laser fields with atoms has developed into an exciting new area of atomic and laser physics. New phenomena as multielectron stripping, above threshold ionization, high-order harmonic generation and stabilization of highly excited atomic states by strong light fields were discovered (see, e.g., [3-8] and references therein). It is very interesting to examine to what extent these effects will persist at the high frequencies of VUV radiation. The coupling of the intense TTF-FEL field to the giant resonances in outer core level excitations are of special interest in this respect. At present there are no models which allow for a straightforward extrapolation towards the high frequencies of VUV radiation. In figure 3.2.1 the regions in which the different dynamical effects (Perturbia = perturbation approaches hold for MPI = multiphoton ionization) are expected to occur are approximately indicated. The intensity I is measured in atomic unit I_0 and the frequency ω in half atomic unit ω_0 , equal to the H 1s binding energy. For low frequencies nonperturbative ionization mechanisms like tunneling and field ionization are important. For high frequencies the atoms are expected to stabilize against the radiation field in specific states if the intensity is large enough.

The TTF-FEL thus opens a fascinating new area for a nondestructive exploration of dilute systems consisting of either atoms or ions. In the following we will outline studies with the TTF-FEL which at present look very promising to us.

a.) Single Photon Multielectron Excitations

Shake-up, shake-down, shake-off and double ionization processes are clear manifestations of electron correlation [1,2]. Therefore, they have attracted considerable interest in recent years (see, e.g., [9-11] and references therein). He and Li^+ are the ideal prototype atom and ion to investigate the Coulombic three particle fragmentation occur-

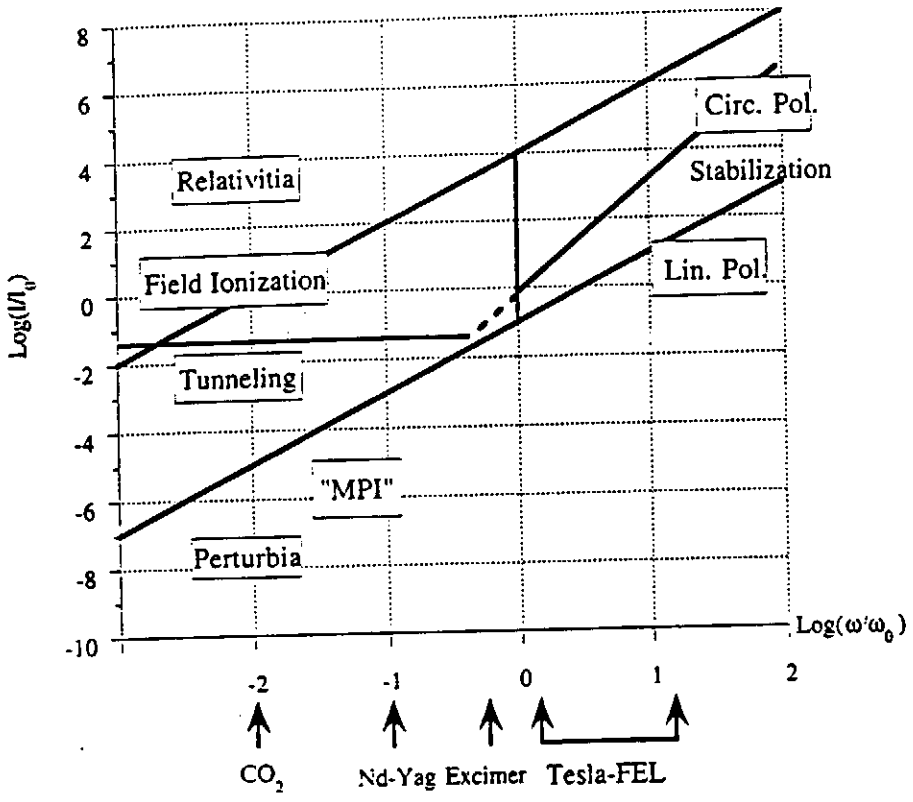

Figure 3.2.1

The nonpertubative regime is represented by the area above the lowest line. It has been drawn according to the criteria that the Keldysh parameter $\gamma k = (E_b / 2\ E_p)^{1/2} = 1$, where the binding energy $E_b = \omega_0 = 1/2$ au. Here E_p is the ponderomotive potential energy, equal to E_p : $(1/4)\ I\ \omega^{-2}$ in atomic units. The nonpertubative part is divided into sections with different strong-field dynamics. In non-hydrogenic systems and Rydberg atoms the nonperturbative intensity limit is expected to be lower than indicated in the figure.

ring in double photoionization. The determination of the triple differential cross section with high angular and energy resolution close to threshold would allow for stringent tests of the most advanced theoretical models. In comparison to present investigations [12] the TTF-FEL would allow for unprecedented accuracy and furthermore for the study of the modifications of the threshold behaviour brought about by the strong laser field. In Li, the simplest open-shell many electron system, recently triply excited states could be populated by the absorption of a single VUV photon [13,14]. In these "hollow" atomic states all electrons reside outside the K-shell. The extremely small cross sections ($\sigma < 100$ kbarn) at present limit these investigations to the strongest resonances and to detection by total ion yield. With the TTF-FEL one can foresee the unravelling of very weak resonances and the extension of the studies above the triple ionization threshold using ion, electron and fluorescence spectroscopy. The experiments on He, Li^+ and Li require a photon energy resolution $\lambda/\Delta\lambda \geq 10.000$. Besides these prototype systems the TTF-FEL will allow to extend these experiments to higher Z atoms and to search for even higher numbers of electrons excited by one photon. Coincidence experiments in which all the outgoing electrons, ions and photons are detected will become feasible at least for special cases providing detailed insight in the dynamics driven by the many particle Coulomb and exchange interactions. Complete photoionization experiments [1] can be foreseen.

b.) Interaction with Free Ions

Experimental data on inner-shell photoexcitation or photoionization in singly or multiply ionized atoms are required for understanding of many laboratory plasma and astrophysical phenomena. As atoms in a condensed matter matrix often exist in ionic form, photoabsorption measurements on free ions can additionally prove very helpful in the interpretation of solid state spectra. Giant resonances are known to occur in photoabsorption of positive ions [15] but their origin is not well understood. Systematic investigations along isoelectronic or isonuclear sequences are of particular value as they provide insight into fundamental aspects of the photoionization process such as relativistic effects, correlation effects, and orbital collapse.

To date there is relatively very little experimental data on the photoabsorption and photoionization behaviour of free ions. This is mainly due to the substantial difficulties associated with the generation and confinement, in adequate numbers, of the ions and also in particular the limited flux of continuum VUV radiation available from synchrotron sources. Recently a number of experiments based on the merging of an ion beam with synchrotron radiation [15,16] have shown some success but only in measuring the spectra of singly or doubly ionized species having considerable cross sections at resonances. The combination of an ion source such as an Electron Beam Ion Source EBIS, which can deliver ion densities of 10^8 cm^{-3}, with a high photon flux source such as the TTF-FEL would represent a dramatic improvement in the level of experimental detection capability over existing synchrotron based set ups. The total number of ions interacting with the VUV photons can be increased by lengthening the interaction region. Well established techniques such as photoabsorption, fluorescence,

photoion, photoelectron and coincidence spectroscopies could be employed to elucidate the resulting photon-ion interaction process.

High power pulsed laser based approaches such as the Dual Laser Plasma technique [17] have been used quite successfully to measure the relative photoabsorption cross section of a number of ions. This technique involved focusing the optical output of a high power (typically 1 J in 20 ns => 5.0 x 10^7 W) pulsed laser, *in vacuo* on a spectroscopically pure metal target which produces a transient high temperature and density plasma with species in various degrees of ionization. By careful determination of the appropriate combination of laser irradiance, focusing geometry, and temporal/spatial probing of the plasma with a bright pulsed VUV source the various dominant degrees of ionization within the expanding plasma can be isolated with a high degree of purity. The short pulse duration, high number of photons per pulse, variable time structure and energy tunability offered by the proposed TTF-FEL makes it an ideal and unique source with which to probe and diagnose the plasma.

c.) Photon induced Atomic Fluorescence and Atomic Bremsstrahlung

The fluorescence emitted upon the decay of excited atomic states can provide detailed information on the states and decay rates complementary to that obtained by electron and ion spectroscopy (see, e.g., [18] and references therein). Selective excitation by photons, the ideal approach, is severely hampered by the low count rates due to the small VUV fluorescence yield. The high photon flux of the TTF-FEL will help to overcome the limitations of present experiments. In addition to the atomic fluorescence lines recently fluorescence continua emitted by atomic electrons virtually excited by charged projectiles have been predicted and detected (see, e.g., [19] and references therein). This polarizational or so called "atomic" bremsstrahlung is expected in the regions of the giant resonances in the outer core level spectra. In comparison to the excitation by external electrons the excitation by internal atomic photoelectrons due to its selectivity should provide for much more stringent tests of the existing models. The photoexcitation by the intense TTF-FEL radiation would furthermore allow for dynamical relaxation studies by exploiting the sequential multiple ionization. Atomic Xe and Ba in the range of the 4d-4f/εf excitations are ideal candidates to start these investigations. The power densities achievable by focusing the TTF-FEL beam are expected to be high enough to produce, for example, fully stripped Li ions. The plasma will emit the Lyman line of H-like Li ions and depending on the geometry and an eventual preionization by a laser amplification of the line may be observed. Thus the TTF-FEL opens a new access for the investigation of laser plasma based VUV laser schemes (see, e.g., [20,21] and references therein).

d.) Laser Excited, Aligned or Oriented Atoms

Transition metal atoms embedded in solids are of great basic and practical importance. This rests with the partially unoccupied outer d or f-shells which strongly influence

the optical, electrical and magnetical properties of the solids. Due to the local character of these orbitals the adequate treatment of the intra-atomic interactions in many cases is essential for description of transition metals/rare earths and transition metal/rare earths compounds [22]. Recently inner shell angular resolved photoelectron spectra of magnetically oriented solids, multilayer systems and surface layers excited with linearly or circularly polarized VUV radiation (linear/circular magnetic dichroism in the angular distribution of photoelectrons LMDAD/CMDAD) were proved to be very sensitive probes for the electronic structure ([23-26] and references therein). Atomic models have been successfully invoked for explaining the origin of the dichroism [27-29]. Experiments on the corresponding free atoms can substantially help to disentangle the intraatomic and the interatomic effects. By laser pumping the atoms can be prepared in a well defined oriented state. Determining the energy and angular distribution of the electrons excited by linearly polarized VUV radiation provides very detailed information on the states and the many electron dynamics of the open shell transition metal atoms. Combining laser and VUV undulator radiation test experiments on alkali atoms have successfully been performed [30-32]. Due to the low count rates most of these investigations were limited to resonant processes. Recently the investigations have successfully extended to atomic Cr. First data on the 3p photoemission on unoriented Cr atoms have been obtained. In order to prevent the destruction of the orientation by radiation trapping, the atomic density in the interaction has to be kept below 1 x 10^{10} atoms/cm^3. For the undulator stations available at present this results in very low count rates. The TTF-FEL seems to be well suited to overcome this problem. A schematic drawing of the envisaged experimental arrangements is presented in figure 3.2.2.

There is another range of experiments the combination of lasers with the TTF-FEL will make feasible. The laser/s can be used to prepare the atom in an excited state of various angular momenta which is probed by the TTF-FEL radiation. These experiments are of special interest for threshold studies, for the investigation of special inner-shell excitations which are very sensitive to changes of the valence occupation (see e.g. [33]), for laser induced changes of autoionizing resonances [34] and for the stabilization of atoms in strong laser fields [3,4].

e.) Multiphoton Processes

The design parameters of the TTF-FEL with about 2*10^{13} photon/pulse at 200 eV photon energy in pulses with 400 fsec duration in a highly coherent beam will, for the first time, allow the investigation of non-linear light matter interaction processes at photon energies that high. According to the short wavelength of the laser radiation it preferentially couples to inner shell electrons of atoms. The simplest non-linear process possible is 2-photon absorption transferring an inner shell electron to the ionization continuum. The 2-photon ionization process will usually be non-resonant, i.e. no unoccupied level of the atom will be near the virtual state reached after the absorption of one photon. But the tunability of the TTF-FEL radiation may even open the possibility to study resonant or near resonant processes in suitably chosen atoms.

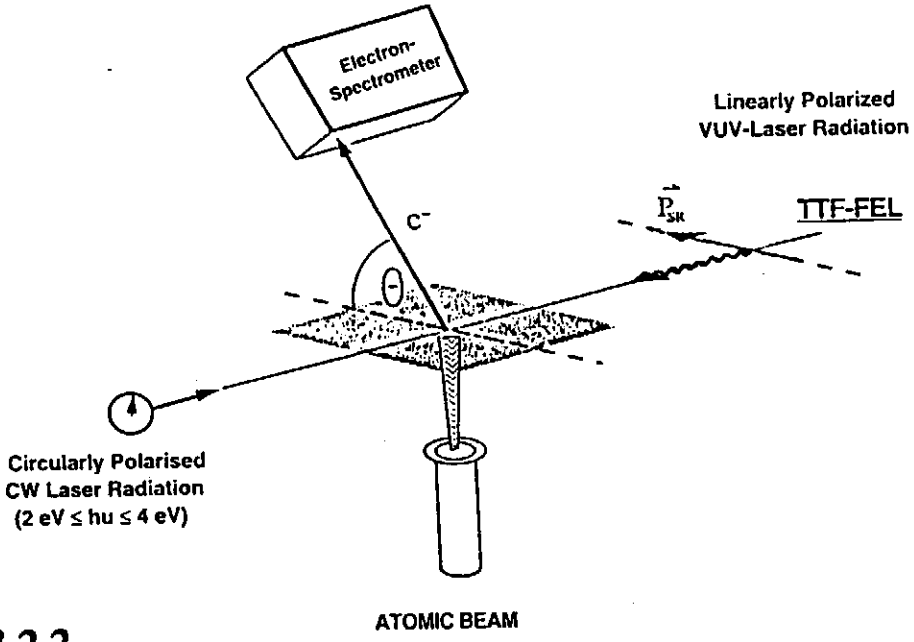

Figure 3.2.2

Scheme of the experimental arrangement for studies of laser excited, aligned, oriented atoms.

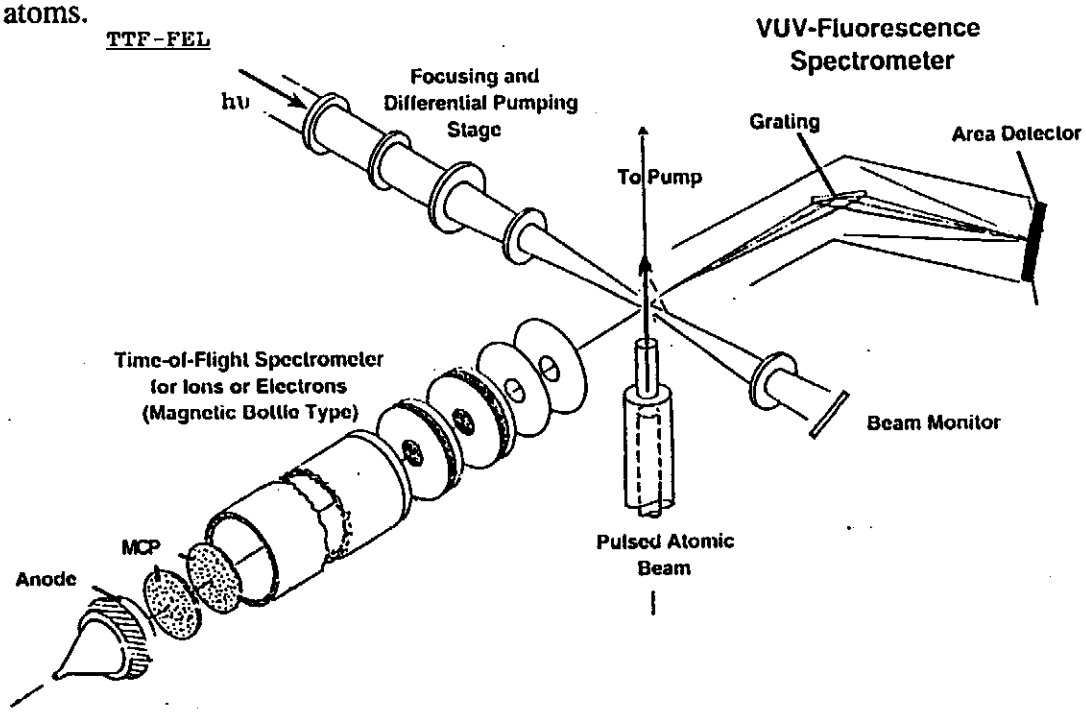

Figure 3.2.3

Scheme of the experimental arrangement for ion, electron and fluorescence spectroscopy on free atoms.

Atoms with giant resonances e.g. Xe 4d-εf are a good choice for first test experiments. The photon energy can be chosen that either $4d^9$ εf resonance forms the intermediate state or the final state in the two photon excitation processes. Atomic giant inner shell resonances are probably also the best candidates for first exploratory experiments on above threshold ionization and higher harmonic generation (see e.g. [3-5]). To make a crude estimate for the power densities required to observe non-linear effects the energy of the VUV laser field inside the volume occupied by the Xe4d orbital has been set equal to the Xe4d ionization energy. This resulted in a power density greater than $1 \cdot 10^{15}$ W/cm^2, a value within the reach of the TTF-FEL. Possible candidates for K-shell ionization with 200 eV photons are atomic carbon with a binding energy of 284 eV or atomic nitrogen with a binding energy of 399 eV. The photoelectron excess energy then amounts to 116 eV and 1 eV, respectively. If, as it is the case in 1-photon ionization, the 2-photon cross section is also largest at the K-shell, atomic nitrogen is the target which should be preferred. In the case of C it would also be possible to use molecules containing this atom as for example CO, or hydrocarbons. The chemical shift of the K-edge is only small so that two TTF-FEL photons are sufficient also for ionization of these compounds which are already either gases or may be evaporated easily. In the case of nitrogen the situation is worse. In N_2 or NO for example the K-electron binding energy is about 410 eV which is larger than 2 hν. Ionization with the TTF-FEL beam thus is not possible if it cannot be tuned to at least 205 eV photon energy.

A candidate for L-shell ionization not too far above threshold is the Ar atom with ionization potentials of 320 eV when a $S_{1/2}$ hole is created and 245 eV and 247 eV when a $P_{3/2}$ and $P_{1/2}$ hole is created respectively. The excess energy of the photoelectrons then is 80 eV, 135 eV, and 133 eV, respectively.

In all cases the ionization process will probably be non resonant. No unoccupied states will be in or near resonance after absorption of the first photon.

The photon absorption process will leave the ion formed in a highly excited state which will decay either already during the 2-photon absorption process or immediately after. For light atoms the process will usually be accompanied by emission of Auger electrons. Since the time scale for decay is of the same order as the lifetime of the virtual intermediate state after absorption of one photon, the question arises whether it will be possible to detect for example Auger emission from this virtual state before the second photon is absorbed. An Auger process of this type should be distinguishable from the usual Auger process because the electron primarily excited in the 2-photon absorption process will be near the ion which emits the Auger electron. The process mentioned here should be distinguished from the already widely investigated photoelectron/Auger-electron interferences or post collision interactions which influence the photoelectron spectra after the interaction with the radiation field is completed. A very interesting question is whether it will be possible to observe laser assisted Auger decays, manifesting itself by side bands which accompany the main line (35). In multiphoton ionization (MPI) processes one important question is whether it is possible to observe correlated two-electron emission, as for example in 1-photon 2-electron ionization of He. The dominant ionization process in MPI is sequential emission of elec-

trons. The TTF-FEL may allow the search for correlated 2-electron emission in 2-photon 2-electron ionization of an atom. This is the simplest MPI process where correlated emission may be investigated. Experiments done up to now use intense visible / UV radiation to investigate processes like this. At these wavelengths many more than 2 photons have to be absorbed to emit two electrons, thus making correlated emission much more improbable than in a 2-photon process.

In extrapolating the experiments performed with high power lasers (3-8) one has to keep in mind that the ponderomotive energy E_p scales with $1/\omega^2$ so it is in the meV range for TTF-FEL compared to eV - keV for conventional high power lasers. The Keldysh Parameter γ_k will be much larger than one in most cases. The situation may change dramatically if a Rydberg state or an inner-well potential barrier state is probed. The nonperturbative regime depicted in figure 3.2.1 could then be easily accessible.

Figure 3.2.3 shows a scheme of the experimental arrangement envisaged for the first series of experiments. The atoms are prepared in a pulsed beam in order to achieve the target density required but still allow for excellent UHV conditions outside the sample environment. The UHV is essential because the intense TTF-FEL beam will excite and ionize atoms and molecules along the path giving rise to intolerable background counts. The intensity of the laser and the target density have to be carefully matched in order to prevent collisions inside the target region to influence the spectra and the formation of space charges resulting in deteriorated electron spectra. Time of flight detectors are probably the best choice for detecting the outgoing electrons and ions. The fluorescence yield in most cases is very small ($\leq 10^{-4}$) in the VUV.Therefore, the entrance slit has to be mounted very close to the interaction region in order to accept a high fraction of the emitted radiation. An integrating area detector with a fast read-out system should allow for the simultaneous registration of ideally the full spectral range of interest. Later on, more detectors and more advanced systems should be implemented to allow for higher angular and energy resolution and for coincidence experiments.

References :

1. V. Schmidt, Rep. Progr. Phys. 55, 1483 (1992)

2. B. Sonntag and P. Zimmermann, Rep. Progr. Phys. 55, 911 (1992)

3. Atoms in Intense Laser Fields, edited by M. Gavrila, Academic Press, New York 1992)

4. Super-Intense Laser-Atom Physics, eds., B. Piraux, A. L' Huiller and V. Rzazew ski (Plenum Press, New York, London, 1994)

5. K.J. Schafer, Barui Yang, L.F. DiMauro and K.C. Kulander, Phys. Rev. Lett. 70, 1599 (1993)

6. B. Walker, B. Sheehy, L.F. DiMauro, P. Agostini, K.J. Schafer and K.C. Kuland er, Phys. Rev. Lett. 73, 1227 (1994)

7. P.B. Corkum, Phys. Rev. Lett., 71, 1994 (1993)

8. Baorui Yang, K.J. Schafer, B. Walker, K. C. Kulander, P. Agostini and L.F. Di Mauro, Phys. Rev. Lett. 71, 3770 (1993)

9. P. Lablanquie, I. Mazeau, L. Andric, P. Selles and A. Huetz, Phys. Rev. Lett. 74, 2192 (1993)

10. J.M. Rost, Phys. Rev. Lett. 72, 1998 (1994)

11. J. Berakdar and H. Klar, Phys. Rev. Lett. 69, 1175 (1992)

12. O.Schwarzkopf, B. Krässig, J. Elmiger and V. Schmidt, Phys. Rev. Lett. 70, 3008 (1993)

13. L.M. Kiernan, J.P. Mosnier, E.T. Kennedy, I.T. Costello and B.F. Sonntag, Phys. Rev. Lett. 72, 2359 (1994)

14. L.M. Kiernan, M.K. Lee, B.F. Sonntag, P. Sladeczek, P. Zimmermann, E.T. Kennedy, J.P.Mosnier and J.T. Costello, J. Phys., B 28 L161 (1995)

15. F.J. Wuilleumier, J.-M. Bizau, D. Cubaynes, B. Rouvellou, L. Journel, Nucl. Instr. Meth., B 87, 190, (1994)

16. M. Oura, S. Kravis, T. Koizumi, Y. Itoh, T. M. Kojima, M. Sano, T. Sekioka, M. Kimura, K. Okuno and Y. Awaya, Nucl. Inst. Meth., B. 86, 190, (1994)

17. E.T. Kennedy, J.T. Costello, J.-P. Mosnier, A.A. Cafolla, M. Collins, L.M. Kier nan, U. Köble, M.H. Sayyad, M. Shaw, B.F. Sonntag and R. Barchewitz, Opt. Eng. Vol. 33, No. 12, 3984, (1994).

18. A. Ehresmann, V.A. Kilin, H. Schmoranzer, K.H. Schartner and M. Ya. Amusia, J. Phys., B 28, 965 (1995)

19. A. V. Korol, A.G. Lyalin, A. S. Shulakov and A.V. Solovyov, J. Phys., B28, L155 (1993)

20. Y. Nagata, K. Miderikawa, S. Kubodura, M. Obara, H. Tashiro, Phys. Rev. Lett. 71, 3774 (1993)

21. A. McPherson, B. D. Thompson, A.B. Borisov, K. Boyer and C.K. Rhodes, Natu re, Vol. 370, 631 (1994)

22. L.C. Davis, J. Appl. Phys. 59, 25 (1986)

23. L. Baumgarten, C.M. Schneider, H. Petersen, F. Schäfers and J. Kirschner, Phys. Rev. Lett. 65, 492 (1990)

24. Ch. Roth, F.U. Hillebrecht, H.B. Rose and E. Kisker, Phys. Rev. Lett. 70, 3479 (1993)

25. F. Sirotti and G. Rossi, Phys. Rev., B49, 15682 (1994)

26. F.U. Hillebrecht, Ch. Roth, R. Jungblut, E. Kisker and A. Bringer, Europhys. Lett. 19, 711 (1992)

27. B.T. Thole and G. van der Laan, Phys. Rev., B 44, 12424 (1991)

28. N.A. Cherepkov, Phys. Rev., B50, 13813 (1994)

29. B.T. Thole, H.A. Dürr and G. van der Laan, Phys. Rev. Lett. 74, 2371 (1995)

30. M. Pahler, C. Lorenz, E.v. Raven, J. v. Raven, J. Rüder, B. Sonntag, S. Baier, B. Müller, M. Schulze, H. Staiger, P. Zimmermann and N.M. Kabachnik, Phys. Rev. Lett. 68, 2285 (1992)

31. S. Baier, M. Schulze, H. Staiger, P. Zimmermann, C. Lorenz, M. Pahler, J. Rüder, B. Sonntag, J.T. Costello and L. Kiernan, J. Phys., B27, 1341 (1994)

32. B. Sonntag and P. Zimmermann, Phys. Bl. 51, 279 (1995)

33. V.K. Dolmatov, J. Phys., B26, L 585 (1993)

34. O. Faucher, D. Charalambidis, C. Fotakis, J. Zhang and P. Lambropoulos, Phys. Rev. Lett. 70, 3004 (1993)

35. J.M.Schins, P. Breger, P. Agostini, R.C. Constantinescu, H.G. Muller, G. Grillon, A. Antonetti and A. Mysyrowicz, Phys. Rev. Lett. 73, 2180 (1994)

3.2.3. Spectroscopy on Clusters and Radicals

Research on clusters has become a very important and active field of interdisciplinary interest in the past years. Clusters, while bridging the gap between molecular and solid state physics, allow the study of how the macroscopic properties of matter are formed by the interaction of their microscopic units. The transition from the atom to the solid is not a smooth transition at all but rather interesting variations can occur. The size of clusters is a new parameter which can be used to control the variation of their properties, namely geometrical and electronic structure, magnetic properties and chemical reactivity. The investigation of these properties as a function of size is a central issue of cluster science and an intellectual challenge. In addition, a thorough understanding of these properties is also of fundamental interest for applications of clusters, especially deposited clusters which can be regarded as "new materials".

Most important fields of applications are catalytic materials and devices in microelectronics. Furthermore, cluster matter which consists of clusters with a narrow size distribution and noncrystalline materials are interesting candidates for future applications.

The study of free clusters in a molecular beam is the natural choice in order to obtain information on their properties. In the past mass spectroscopy with electron impact ionisation, laser spectroscopy, and also synchrotron radiation-based-research were the most powerful scientific techniques. While synchrotron radiation (SR), thanks to the selective excitation with photons of nearly any desired energy, is in principle the most suitable source of excitation, it has the severe disadvantage of only moderate photon flux. Typically, at the sample position a flux of 10^{10}-10^{12} photons/s is obtained which is much lower than the flux of intense lasers delivering 10^{16}-10^{18} photons/s. As a result, worldwide only very few groups are using SR for cluster spectroscopy, most of them working at BESSY and HASYLAB [1-4]. So far, experiments were only performed on clusters in a molecular beam with its natural, rather broad size distribution. The size of the clusters is usually controlled by the source conditions and preferentially only loosely bound systems like van der Waals clusters could be studied. Other interesting systems like metallic or covalently bound clusters could not be produced so far in sufficient quantities - apart from a few exceptions [5] - in order to do spectroscopy with SR. In several experiments using SR, e.g. photoionisation, the size of clusters is determined with a mass spectrometer. Usually the size measured this way differs considerably from that of the neutral clusters which have absorbed the radiation, since fragmentation takes place. Therefore, it is highly desirable to preselect clusters of well defined size before the excitation or ionisation.

Laser sources on the other hand allow the properties of size selected clusters of various materials to be explored since the photon flux is usually several orders of magnitude higher. For many applications, however, the energy of photons from a conventional laser is not sufficient to excite or ionize clusters, at least with a single photon. This is a severe limitation.

The short wavelength and extremely high brightness of the radiation from the TTF-FEL for the first time combines both the advantages of SR and conventional lasers. In contrast to experiments on solid samples, research on clusters, radicals and reactive species in a beam can take full advantage of the high flux and peak power because of the continuous replenishment of the sample. Thanks to the unprecedented flux and brightness, experiments on mass selected species of nearly any desired material become feasible. As a result of these perspectives, a considerable number of studies have been already proposed [6]. They fall into four separate groups:

A) Investigations on the electronic structure of occupied and unoccupied levels with photoelectron spectroscopy (UPS, XPS) and absorption spectroscopy (near edge absorption, NEXAFS).

B) Studies of the geometrical structure (XANES, EXAFS).

C) Experiments to obtain information on the dynamics (vibration, dissociation), the energy flow and the relaxation dynamics (e.g. Coulomb-explosion). Pump-and-probe and coincidence techniques are the experimental methods of choice.

D) Investigations on the chemical, electronic and dynamic properties of clusters deposited on surfaces and of cluster matter.

In order to illustrate the potential of applications, a few selected types of experiments will be discussed below in more detail.

A) Investigation on the Electronic Structure

The level structure and the bonding mechanism of metallic or covalently bound clusters can be studied with valence shell photoelectron spectroscopy (UPS). There are nearly no limitations regarding binding energy of the valence levels under discussion since the energy of the TTF-FEL-radiation can be varied between 30 - 200 eV. This is of considerable importance for adsorbate systems like CO on metallic clusters which might play a role in catalytic processes. In this particular case the relevant levels are 7-12 eV below the Fermi-level of the metal. It should be noted, however, that an extension of the operating range and the tunability of the TTF-FEL down towards 20 or even 10 eV would be of great interest, allowing to dose the gap to the range of tunable optical laser radiation. Mass selective experiments are essential since the level structure of small clusters containing up to 100 atoms varies substantially with cluster size. Valence (UPS) and inner-shell photoelectron spectroscopy (XPS) offers an elegant way to study changes in the binding mechanism [7-9]. A transition from non-metallic to metallic behaviour can be directly seen in the screening of inner-shell photoelectron spectra [10]. Thus the TTF-FEL with high energy photons opens up a very new field of activities.

In addition, inner-shell photoelectron spectroscopy (XPS) is particularly useful for the

study of heteroclusters since the environment of the different elements can be investigated separately by choosing the desired inner-shell level. Thanks to the local character of inner-shell excitations, information on the electronic and geometrical structure can be obtained simultaneously. This is an important aspect. Usually, information on the geometrical structure is difficult to obtain and a comparison with sophisticated theoretical work is often needed.

At lower energies not yet accessible with conventional laser systems (E < 24 eV) clusters with high ionization potentials (e.g. He) could be used as transparent host media for molecules and small clusters. Finally, pump-and-probe photoemission combining a resonant excitation with TTF-FEL-radiation into an unoccupied level and subsequent ionisation with a conventional laser allows site selective photoemission to be studied. Well defined atoms of the cluster, e.g. surface atoms, can be selectively excited by the choice of the energy of the TTF-FEL-photon. Site-specific two-colour photoelectron spectra should contain a wealth of information on the electronic and geometrical structure of clusters which can be interpreted in a more direct way than valence shell data.

B) Studies of the Geometrical Structure

The analysis of oscillatory structures (XANES, EXAFS) in the inner shell ionisation continua of condensed matter is a very direct method to obtain information on the geometrical structure, especially bond distances.

At present, only few experiments have been performed on clusters which demonstrate the feasibility in principle [11,12]. Detailed information, however, is difficult to obtain because the variations in the systems studied so far are small or averaging of clusters with various sizes is unavoidable. Again, with TTF-FEL radiation a breakthrough can be achieved, assuming that a sufficiently large scanning range of at least 200 eV above the inner-shell edges will be provided. For this class of experiments either the third harmonic of the TTF-FEL which can be tuned to 600 eV or a higher energy of the Linac (see chapter 16) is needed. The major drawback of present studies, namely the averaging over different sizes can be overcome using mass selected beams which require very high photon fluxes due to the very low target density. In addition, selectivity concerning different isomers can be achieved with various annealing techniques.

C) Dynamical Processes

One of the most important advantages of radiation from the TTF-FEL compared to conventional SR is the short pulse length of ≈ 500 fs. This is close to typical vibrational periods and dissociation times. Furthermore, the high peak power in the GW range make TTF-FEL radiation ideally suited for all kinds of pump-and-probe experiments, e.g. in combination with fs-optical lasers. Several different modes can be used :

- pumping with the high energetic TTF-FEL-photon and then probing with the optical laser "two-colour" experiment), or reversing the assignment of pump

and probe radiation

- splitting the TTF-FEL beam in some way and probing with the same wave length ("one colour" experiment)
- using harmonics of the TTF-FEL to yield different well synchronized wave lengths for pumping and probing

There is an enormous potential of applications for these types of experiments on dilute samples. Metal and semi-conductor clusters, covalently and van der Waals bound systems, radicals and complexes which play an important role in atmospheric processes and finally a large number of fullerenes and their derivatives, particularly endohedral species, are all of great interest in this context. By synchronizing the two light pulses and varying the delay time information on dynamical processes like vibration, dissociation and coulomb explosion can be obtained in real time. Photoelectron, ion and fluorescence signals as well as combinations of these (electron-ion : PEPICO, ion-ion (PIPICO, for studies of fragmentation etc.) can be used as a monitor.

In addition, pump and probe methods can be applied to get information on chemical reaction pathways. In such a scheme, a first ultrashort laser pulse triggers a chemical reaction in a cluster of reactants by either creating a reactive photofragment, or by detaching an electron from one of the cluster constituents. The time-delayed pulse from the TTF-FEL then probes the progress of the reaction. In contrast to experiments with low photon energy from optical lasers, site and element specific studies become feasible by choosing the suitable excitation energy.

D.) Deposited Cluster and Cluster Matter

The unique properties of free clusters (ionization potentials and electron affinities varing with the number of atoms, clusters of metal atoms can develop a very specific "band" structure, being accompanied with several "bandgaps", etc.) should have an interesting influence upon contact with a surface (deposited clusters). Also, the aggregation of clusters to form a thin film or a three dimensional body (cluster material) could give rise to a new class of material with special properties, e.g. single electron conductivity. The physical understanding of this interaction of clusters with an environment is not well developed.

The time structure of the TTF-FEL in combination with the accesible photon energy range open up two groups of experiments : Firstly, deposited metal clusters could be analyzed by time of flight photoelectron spectroscopy excited by the short pulses of the TTF-FEL. The feasibility has recently been demonstrated by the use of 9.9 eV laser light pulses [15] (length : 10 ns, sum frequency mixing of dye-laser light in a mercury cell.)

There the development of high-lying valence states of lead clusters on a semiconductor surface could be followed up to the bulk although the energy resolution of the experiment was poor due to the pulse length. With the high energy TTF-FEL pulses the

whole valence band is accessible with a resolution enhancement by some orders of magnitude. Many other studies of the electronic structure of the cluster-surface system will be possible similar to those as discussed in the section 3.2.4. Secondly, the high flux in combination with the time structure could be used to manipulate the cluster material. Especially the extreme high power VUV pulses might be suitable to micro-machine the material. The locally confined radiation could serve to selectively carve or build up microstructures at a relatively low overall heat transfer.

The experimental techniques needed to perform these types of studies are already available or have to be only slightly modified. Sources for mass selected cluster ions which are in use for photoelectron spectroscopy [13] or pump-and-probe experiments [14] deliver a particle density of 10^4 - 10^6 clusters/cm^3. It is expected that only small improvements in the quality of the vacuum conditions prevailing in a typical cluster beam apparatus should be necessary in order to reduce the background signal which is due to the ionization of residual gas. The counting rates are expected to be of the same order of magnitude as in experiments with conventional lasers because the flux of the TTF-FEL is somewhat higher while absorption coefficients at higher energies are lower than the respective values in the optical range. In addition it is expected that the availability of TTF-FEL-radiation in the VUV-range will stimulate the development of new sources for size selected clusters which can also be of interest in view of applications e.g. cluster deposition for preparing "new materials".

In summary, radiation from the TTF-FEL will open up very new and exciting possibilities for research on dilute samples as clusters and radicals. Experimental approaches needed to fully take advantage of the high flux, brightness and short-pulse length are already in part available or could be realized with some modifications.

References :

1. M. Fieber, G. Bröker, A. Ding, Z. Phys. D20, 21 (1991)

2. W. Kamke, J. de Vries, J. Krauss, E. Kaiser, I.V. Hertel, Z. Phys. D14, 339 (1989)

3. E. Rühl, C. Heinzel, A.P. Hitchcock, H. Baumgärtel, J. Chem. Phys. 98, 2653 (1993)

4. J. Stapelfeldt, J. Wörmer, T. Möller, Phys. Rev. Lett. 62, 98 (1989)

5. C. Brechignac, M. Broyer, Ph. Cahuzac, G. Delacretaz, P. Labastie, J.P. Wolf, L. Wöste, Phys. Rev. Lett. 60, 275 (1988)

6. Workshop on Scientific Applications of VUV and Soft-X-Ray Radiation from the TESLA-Free Electron Laser at DESY, April 27-28, 1995

7. Chia-Yen Cha, G. Ganteför, W. Eberhardt, J. Chem. Phys. 100, 995 (1994)

8. B. Kaiser, K. Rademann, Phys. Rev. Lett. 69, 3204 (1992)

9. G. Ganteför, M. Gaussa, K.H. Meiwes-Broer, H.O. Lutz, Z. Phys. D9, 253 (1988)

10. G.K. Wertheim, Z. Phys. D12, 319 (1989)

11. E. Rühl, C. Heinzel, A.P. Hitchcock, H. Schmelz, H. Baumgärtel, W. Drube, R. Frahm, J. Chem. Phys. 98, 6820 (1993)

12. F. Federmann, O. Björneholm, A. Beutler, T. Möller, Phys. Rev. Lett. 73, 1549 (1994)

13. Chia-Yen Cha, G. Ganteför, W. Eberhardt, Rev. Sci. Instrum. 63, 5661 (1992)

14. S. Wolf, G. Sommerer, S. Rutz, E. Schreiber, T. Leisner, L. Wöste, R.S. Berry, Phys. Rev. Lett., in press

15. R. Hector, K.H. Meiwews-Broer, Surf. Sci., to be published

3.2.4 Reaction and Relaxation Dynamics in Photochemistry and Surface Science

The TTF-FEL is a completely new type of radiation source offering unique properties in terms of flux, brightness and time structure in the photon energy range of 50-200 eV in the first harmonic of the undulator. These properties will make the TTF-FEL ideally suited for a wide range of new experiments aiming at an improved understanding of relaxation and reaction dynamics as well as reaction kinetics in molecular photochemistry and surface science. An extension of the energy range to lower energies is under discussion and might also be of considerable interest.

Firstly, the very high flux and brightness of the source - two orders of magnitude higher than that of 3rd generation synchrotron radiation sources - make highly state resolved experiments of the complete dynamics of photoinduced reactions feasible which have so far not been possible due to intensity limitations. They also offer possibilities for an improved understanding of reaction pathways, site selectivity and kinetics of reactions on well defined surfaces and real catalysts. The high photon density will even allow the preparation of "exotic" highly excited states of adsorbates and surface layers where all atoms or molecules on a surface can be excited within one pulse of the FEL.

Secondly, the high peak power and the short pulse width (~ 350fs) will open up the possibility to perform pump-probe experiments to study the real-time dynamics of excited states of free and adsorbed molecules in a photon energy range which has so far not been accessible to such experiments. Hence the use of the FEL pulse as pump or probe pulse in a two pulse correlation experiment makes possible the use of well established inner-shell spectroscopies as diagnostic tools for the time evolution of excited molecules. This results in the possibility for studying the motion of individual atoms or the change in electronic structure in the course of a half-collision or full-collision reaction. It will also be feasible to investigate the evolution of electronically excited states of adsorbates or even of a laser induced plasma in real-time.

In the following these exciting new opportunities will be explained in somewhat more detail using a short description of experimental proposals put forward by twelve groups from four European countries. The discussion starts with experiments aiming at an understanding of the microscopic dynamics of excited molecular states followed by a short description of those proposals dealing with the reaction and adsorption kinetics on surfaces.

Dynamics of Photoinduced Reaction and Relaxation Processes

One of the major advantages of using the TTF-FEL in the study of photoinduced processes, in the gas phase or at surfaces, will be the possibility to determine the complete microscopic dynamics of these processes. This can either be achieved by performing experiments aiming at a complete determination of all final states of a photoinduced process or by doing time-resolved experiments and thereby following the evolution of these processes. While the former will rely on the unprecedented high flux of the FEL, the latter will make use of the high peak power and the short pulse width.

Competing relaxation and dissociation processes in molecules in the gas phase can be explored by measuring the angle-resolved time-of-flight spectra of the resulting Auger electrons and ion fragments in coincidence or non-coincidence after core electron excitation and ionization *(Relaxation and dissociation of small molecules)* [1,2]. The coincidence technique allows a complete determination of the fragmentation pattern and the dynamics of photoinduced reactions [3]. The results will be very interesting by itself but also for comparison with experiments on photoinduced processes at surfaces as recent studies have revealed striking differences between the photochemistry of free and adsorbed molecules.

In this context it is interesting to look at the interaction between the excited electronic states of the adsorbed molecule and the surface or molecular layer [4,5], the modification of the molecular post-dissociation dynamics by the surface or molecular layer, or the opening of new molecular excitation channels via interaction with hot electrons photoexcited in the surface or molecular layer [6] *(Surface photodynamics and surface modification in the VUV)*. For this purpose a number of highly state resolved experiments concentrating on the photoinduced desorption of molecules is suggested. The number of desorbing molecules in specific channels will be substantially increased by the high flux which is easily 10^2 - 10^5 times more intense than common sources.

While the former two experiments infer the complete microscopic dynamics of a photoinduced reaction process from a complete determination of the final state distribution, the following experiments will all try to make use of pump-probe techniques correlating two laser pulses to obtain time-resolved information on the microscopic reaction dynamics and the evolution of the electron structure in photodynamical processes.

The considerable efforts made to follow the motion of individual atoms during a chemical reaction by ultrafast electron diffraction revealed serious problems with respect to sensitivity, timing, and space charge effects [7]. It is intended to circumvent these difficulties by using time-dependent EXAFS *(Photodissociation dynamics from time dependent EXAFS and photoelectron diffraction)* and thus generating the electrons in the target and restricting the area in which coherence of the interfering electron waves is required to the spatial interval between the constituents of the target [8]. Dissociation of a diatomic molecule will be studied to develop the method. It is triggered at t=0 with an optical laser synchronised to the TTF-FEL [9]. After a time delay Δt a free electron wave with a kinetic energy of typical 50 to 200 eV is generated by the FEL in one of the target atoms. The interference with the back-scattered part of the wavefield from the other atom shows up in the absorption coefficient for the FEL light which will be monitored via transmission or via the emission of electrons or ions. The difference in the EXAFS signal with and without trigger laser will be recorded with a high repetition rate in slowly scanning Δt for some fixed FEL energies. EXAFS on the 3d shell of Br_2 (70 eV binding energy) represents a promising candidate due to the slow motion, the large scattering cross section and the low binding energy. An extension to larger molecules and to surface reactions, as well as to more general photoelectron diffraction schemes using photoselection [8], will be considered after demonstration of the feasibility of the method.

Complementary information can be obtained in studies of the changes in the electronic structure of molecules during the course of a reaction *(Time resolved studies of the electronic structure of molecules during chemical reactions).* The experiments are also of pump-probe type where an initial laser pulse starts a reaction (defining the start time) and a second pulse subsequently (at a well-defined time during the reaction) induces electron or photon emission or further excitations. Hence one would be able to map the variation in electronic structure during a chemical reaction, i.e. the formation and breaking of chemical bonds could be studied with time resolution. These experiments are therefore complentary to experiments where the nuclear pathways on potential energy surfaces are tracked [10].

The reaction dynamics of adsorbates is of major importance for the understanding of chemical processes at surfaces [11]. Catalytic reactions at metal and semiconductor interfaces are of particular interest *(Time-resolved reaction dynamics at semiconductor surfaces)*. Until now, time-resolved experiments to observe chemical reactions at surfaces have only been performed in a very limited number [12,13]. For the realisation of such experiments ultra-short light pulses in the subpicosecond regime are needed with photon energies that are sufficient for core level excitation. The oxidation of silicon is in this context an interesting model system to study reactions in real time. Laser light of 5-10 eV is used to start the reaction, here to induce the dissociation of molecular oxygen and to provide oxygen atoms. Then the reaction products will be detected at the surface with a time delay by the FEL light in the picosecond regime. Furthermore, the dynamics of the oxidation can be studied for each oxidation state separately using the high energy resolution of the FEL beam. By varying the delay time the course of the reaction can be observed.

Of considerable interest in the area of photoinduced reaction processes at surfaces are investigations of the electronic structure and evolution of the respective electronically excited states *(Photoinduced dynamics in surface layers)* in chemisorbed, physisorbed and condensed layers and their interaction with the substrate, co-adsorbates and resonantly excited neighbors (dependent on excitation density, lifetime) by monitoring electrons [14] and reaction products [15]. In the cases where lifetimes in the sub-ps regime are expected, pump-probe techniques synchronizing laboratory lasers to the TTF-FEL will give new insight in the dynamics of these excited states.

Similar two-pulse correlation and pump-probe experiments can be used to study state selective desorption of molecules *(Time-resolved studies on photoinduced processes at surfaces)* in order to measure the partial energy dissipated in single rovibronic states of the desorbing molecules after the rupture of the surface bond [16, 17]. The energy distribution is characteristic for the dynamics of the photostimulated processes. Local effects can be explored via photoelectron emission microscopy of photostimulated processes on complex surfaces where the surface can have different domain structures simultanously [18].

The high photon density of the focused beam of the TTF-FEL will reach intensities sufficient for real time diagnostics of highly excited states of solids; e.g. plasmas induced by a synchronized laser pulse of a second laser. The desorbing species of such plasmas are used in vapor deposition techniques. The study of these plasmas is a

scientific area in itself, because many of the processes going on in the plume are not completely understood *(Study of the chemical dynamics of compounds in laser ablation plumes)* [19]. To obtain more detailed information on these processes on a femtosecond timescale, the atoms or compounds in the plasma which can be excited element specifically via core level excitation from the FEL probe pulse will be detected by secondary processes like photoemission, fluorescence or ion mass spectroscopy. By scanning the small focus of the FEL radiation from the surface of the material along the plume, aggregation processes can be studied.

Reaction Kinetics at Surfaces

The understanding of reactive processes is of central interest in the physics and chemistry of surfaces. Among the most powerful tools to study adsorbed species such as atoms, molecules, radicals or reaction intermediates are electron spectroscopies utilizing synchrotron radiation in the VUV and soft x-ray region from 2nd or 3rd generation sources. Due to the limited flux from these sources it is up to now only possible to study the static properties of adsorbates. Using the high intensity and also the well-defined and adjustable time structure of the TTF-FEL it will be possible to follow reactive processes on time scales reaching from 100 ms down to 100 ns and thus to study their time evolution in great detail. In the following, the potential to study reactive processes on surfaces will be illustrated by discussing four different experiments addressing various aspects in this area.

Studies of the *Selective Photochemical Decomposition of Adsorbed Molecules* can provide detailed insight in the photochemisty on surfaces. A powerful means for the activation of controlled chemical reactions involves electronic excitation of adsorbates by VUV photons: Selective bond breaking by selective photon excitation of molecules adsorbed on silicon surfaces has been demonstrated by recent photodesorption experiments [20]. Photodesorption does, however, not allow to study the products left on the surface. Due to the limited photon flux of existing synchrotron radiation sources, previous studies to characterize photoreaction products by electron spectroscopies used the broadband white light of synchrotron radiation for the VUV excitation [21,22]. The increased photon flux of the TTF-FEL would open up the possibility to combine selective monochromatic photon excitation (in the range 30-150 eV) of adsorbed molecules with UPS and XPS analysis of the deposited products. In addition, selectivity in the area could be tested by using scanning UPS and XPS microscopy.

In a somewhat different approach the *Reaction and Relaxation Dynamics at Core Level Thresholds* can be investigated by selective excitation. The induced chemical modifications can then be studied *in situ* by means of high resolution core level photoelectron spectroscopy [23]. The excellent spectral width of the monochromatized FEL radiation connected with the high flux makes a chemical shift selectivity possible and allows to follow the reaction kinetics. These studies are a link between surface reactions on pure surfaces and cluster experiments. Mass selected clusters can be studied first in the beam and later on their structural and electronic modifications during deposition on surfaces. Further experiments are high resolution photoelectron spectroscopy on biomolecules, ion beams and time resolved experiments of reactions on surfaces by scanning the probe through the focal spot.

The superior qualities of the FEL radiation also allow the implementation of *Time Resolved Electron Spectroscopies of Chemical Reactions on Surfaces*. These measurements should allow the study of the evolution of the chemical state of adsorbates on single crystal surfaces and ultra-thin layers during the reaction in great detail. Of particular interest are the dissociation of molecules and the formation of intermediates or new species by the reaction of two adsorbed species or one adsorbed species and a second species provided from the gas phase via a pulsed supersonic molecular beam [24]. The reactants will be atoms and/or small inorganic and organic molecules. The FEL light is used to do photoelectron spectroscopy in the core region (XPS) and in the valence region (UPS) [25], as well as x-ray induced Auger electron spectroscopy and near edge x-ray absorption spectroscopy of the starting and ongoing reaction on a time resolved basis.

A complementary project focusses *on Time Resolved Photoelectron Spectroscopy with Real Catalysts*. Up to now photoelectron spectroscopy which is most relevant to catalysis has been widely excluded from this development due to the high-vacuum requirement, low signal intensities and associated high signal accumulation times [26-28]. The project aims at the development of time-resolved photoelectron spectroscopy for the investigation of transient processes involving adsorbed species and/or components of the catalyst surface: The surface previously studied under steady-state conditions is charged with a pulse of gaseous material. Spectra are recorded during and after the interaction of the pulsed substance with the catalyst. Adsorbate spectra are isolated by difference and interpolative approaches. Such a methodology becomes possible only with the high photon flux supplied by the TTF-FEL which should give the chance to acquire well-resolved photoemission spectra in very short times.

References

1. O. Hemmers, F. Heiser, J. Eiben, R. Wehlitz, and U. Becker, Phys. Rev. Lett. **71**, 987 (1993)
2. A. Menzel, O. Hemmers, B. Langer, R. Wehlitz, and U. Becker, in "Sixteenth International Conference on X-Ray and Inner-Shell Processes", ed. L. Sarkadi, D. Berényi (Debrecén, 1993), p 202.
3. N. Saito, F. Heiser, O. Hemmers, K. Wieliczek, J. Viefhaus, and U. Becker, Phys. Rev. A, Rapid Communications, in press (1995)
4. R. E. Palmer, Surf. Sci. **307-309**, 335 (1994)
5. R. E. Palmer, Prog. Surf. Sci. **41**, 51 (1992)
6. R. E. Palmer, and P. J. Rous, Rev. Mod. Phys. **64**, 383 (1992)
7. J. C. Williams, M. Dantun, S. B. Kim and A. H. Zewail, Chem. Phys. Lett. **196**, 529 (1992)
8. D. P. Woodruff and A. M. Bradshaw, Rep. Prog. Phys. **57**, 1029 (1994)
9. B. Kohler, V. V. Yakovlev, J. Che, J. L. Krause, M. Mesina, K. Wilson, R. M. Withnell, Y. Yan and N. Schwentner, Phys. Rev. Lett., in press.
10. J.C.Polanyi and A.H.Zewail, Acc.Chem.Res. **28**, 119 (1995) and references therein.
11. H. Zacharias, International Journal of Modern Physics, **B 4**, 45 (1990)

12. L. Schroeter, Chr. Trame, J. Gauer, H. Zacharias, R. David and W. Brenig, Farad. Discussion **96**, 55 (1993)
13. F. Budde, T. F. Heinz, M. M. T. Loy, J. A. Misewich, F. de Rougemont and H. Zacharias, Phys. Rev. Lett. **66**, 3024 (1991)
14. W. Wurth, and D. Menzel, in "Application of Synchrotron Radiation, High-Resolution Studies of Molecules and Molecular Adsorbates on Surfaces", ed. W. Eberhardt, Springer Verlag Berlin 1995, p. 171
15. P. Feulner, and D. Menzel, in "Laser Spectroscopy and Photochemistry on Metal Surfaces", ed. Hai-Lung Dai and Wilson Ho, World Scientific Publishing Co., Singapore, in press
16. K. Al-Shamery, I. Beauport, H.-J. Freund, H. Zacharias, Chem. Phys. Lett. **222**, 107 (1994)
17. M. Menges, B. Baumeister, K. Al-Shamery, H.-J. Freund, C. Fischer, P. Andresen, J. Chem. Phys. **101**, 3318 (1994)
18. "Adsorption on ordered surfaces of ionic solids and thin films", eds. H.-J. Freund, and E. Umbach, Springer Series in Surface Science **33**, Springer Verlag, Berlin 1993
19. J. Cheung, and J. Horwitz, J. Mat. Res., Febr. 1992, p. 30
20. G. Dujardin, G. Comtet, L. Hellner, T. Hirayama, M. Rose, L. Philippe and M. J. Ramage,
    Phys. Rev. Lett. **73**, 1727 (1994)
21. F. K. Perkins et al., J. Appl. Phys. **69**, 4103 (1991)
22. R. A. Rosenberg et al., Appl. Phys. Lett. **58**, 607 (1991)
23. N. Mårtensson, A. Nilsson, in "Application of Synchrotron Radiation, High-Resolution Studies of Molecules and Molecular Adsorbates on Surfaces", ed. W. Eberhardt, Springer Verlag Berlin 1995, p. 171
24. A.V.Hamza, H.-P.Steinrück and R.J.Madix, J.Chem.Phys. **86**, 6506 (1987).
25. H.-P.Steinrück, Appl.Phys. **A 59**, 517 (1994).
26. W. Grünert, A. Yu. Stakheev, W. Mörke, R. Feldhaus, K. Anders, E. S. Shpiro, Kh. M. Minachov, J. Catal. **135**, 269 (1992)
27. W. Grünert, R. Schlögl, H. G. Karge, J. Phys. Chem. **97**, 8638 (1993)
28. W. Grünert, M. Muhler, K.-P. Schröder, J. Sauer, R. Schlögl, J. Phys. Chem. **98**, 10920 (1994)

3.2.5. High Resolution Photoelectron Spectroscopy of Excited Solids

Application of the TTF-FEL offers new perspectives in the study of the electronic structure of solids and solid surfaces by photoelectron spectroscopy. This is particularly the case for instance in the investigation of the momentum resolved electronic structure around the Fermi-level, studies of impurities, both of which require exceptionally high photon fluxes (not achievable with conventional synchrotron radiation sources). The investigations of phenomena related to highly excited electronic systems open up to a completely new field.

High angle and energy resolved photoemission with variation of photon energy has emerged as a powerful tool to investigate the electronic structure of solids. In recent years progress has been made in studying the *band structure of solids* including the effects of *many body interactions* [1,2] in the photoemission process. The measurement of *photoemission line shapes* [3] together with the theoretical determination of spectral functions will give a detailed microscopic understanding of electronic excitations and macroscopic properties which can be correlated with results from highly sophisticated quasiparticle / many body theories [1,2]. In particular, the *spectroscopy at and close to the Fermi surface* [4], which is important for the understanding of transport, magnetic phenomena and superconductivity, requires exceptionally high angle and energy resolution of the photoemission spectrometers. It would then be possible to determine Fermi surfaces and to investigate e.g. the nature of the normal state and the gap anisotropy of high temperature super conductors [5], Kondo resonances in heavy Fermion systems, metal-insulator-transitions. The current generation of photoelectron spectrometers, even those under development at third generation synchrotron sources like BESSY II, will only achieve an overall energy resolution of ~ 10 meV at relativeley low count rates due to limitations of the primary photon flux. A total energy resolution of the order of 1 meV, which is desirable and in many cases essential for the above mentioned studies, will not be achievable with acceptable data acquisition times due to the limited flux of the current synchrotron radiation sources. The high intense TTF-FEL, however, together with an appropriate monochromatization (goal $\leq$ 1 meV) will provide excellent experimental conditions.

A second class of interesting new experiments requiring high flux is the study of very *dilute concentrations* of atoms in solids, or on surfaces, and at interfaces, such as dopants, submonolayer adsorbates and defects. The spectroscopy of related electronic states, in particular in the fundamental band gap of semiconductors, a region hardly accessible so far, needs also high resolution together with a high dynamic range.

Thirdly, it will become possible to study the electronic structure of highly excited solids using the extremely high photon flux provided by the TTF-FEL. At first there are *pump and probe* techniques which are suitable to study the occupied and "unoccupied" electronic states of the redistributed electron system on one energy scale using as a probe the same photoelectron spectroscopy methods as are being used today. First

experiments already performed in a limited photon intensity range using gas discharge lamps have revealed photon induced band bending effects at semiconductor surfaces. Of particular interest are *changes in the band structure and non-linear effects* induced by the high photon intensity. Due to changes in the potential and especially breaking of the original crystal symmetry new or modified electronic states will emerge as a function of photon intensity. Moreover, by controlling the population of the orbitals at special symmetry sites a large variety of potentials may be generated which probe besides the one-particle structure also the density dependent ansatz for the correlation functional and the more general assumptions for the self energy. A quantitative theoretical understanding will become possible when the photon intensities can be adjusted over several orders of magnitude. Summarizing the conditions for this class of experiments there is a definite need for a *continuous, calibrated attenuation of the light beam*. This would permit studies of the continuous transition of the electronic structure of solids from the normal state through varying degrees of excitation up to the transformation into the liquid/gas phase.

References :

1. P. Fulde, Electron Correlations in Molecules and Solids, Springer Series in Solid State Sciences **100** (1991)

2. E. Dagotto, Rev. Mod. Phys. **66**, 763 (1994)

3. R. Claessen, R.O. Anderson, J.W. Allen, C.G. Olson, C. Janowitz, W.P. Ellis, S. Harm, M. Kalning, R. Manzke, M. Skibowski, Phys. Rev. Lett. **69**, 808 (1992)

4. M. Skibowski, L. Kipp, J. Electron Spectr. Rel. Phen. **68**, 77 (1994)

5. H. Ding, J.C. Campuzano, A.F. Bellmann, T. Yokoya, M.R. Norman, M. Rande ria, T. Takahashi, H. Katayama-Yoshida, T. Mochiku, K. Kadowaki and G. Jen nings, Phys. Rev. Lett. **74**, 2784 (1995)

3.2.6 Magnetic Materials, Dichroism

The table below gives an overview on experimental methods and special experiments which seem to be feasible with the TTF-FEL in various states of its development. In the beginning many of the experiments shown below can be started at low photon energy (20 eV) with considerable advantage over 3rd generation synchrotron radiation facilities by making use of the ultra-high brightness and the time structure of the projected e-beam and of the emitted radiation. Some experiments (magneto-optical microscopy, dichroitic microscopy) would benefit dramatically from having tuneable radiation in the transition metal 3p threshold range (50 - 70 eV). Some of the experiments are described in more detail below emphasizing the necessity to use the TTF-FEL.

Get Information / on: Experiment		Domains, Domain Walls	Spin Correlations (T)	Electronic Structure	Phonons Spin-Phonon-Coupling
A	single e-bunch transmission	one-shot			one-shot
B	Magneto-optical microscopy in the XVUV	one-shot Quasi-CW	one-shot (subsequent bunches) pump-probe		
C	Spin-resolving spectroscopies	Quasi-CW C1	one-shot pump-probe	one-shot Quasi-CW (ultra high energy resol.)	one-shot pump-probe C2
C3	Spin-resolved scanning photoelectron microscopy	Quasi-CW		Quasi-CW	
D	Dichroitic spectroscopies and microscopies	Quasi-CW			
E	Evaluation of fluorescence radiation	Quasi-CW		one-shot (subsequent bunches)	

a.) Single e-bunch transmission through magnetic thin films

Very recently, H.C. Siegmann et al. [1] made use of the ultrashort magnetic field pulse connected with the single e-bunch. The pulse is shorter by an order of magnitude than field pulses obtained by ordinary current flow. The experiment has been performed in transmitting the bunches from the final focus test facility of the Stanford linear accel-

erator through a thin magnetic film made of an uniformly pre-magnetized magnetic recording material. The goal was to observe if the ultrashort magnetic pulse of 6 ps duration produced thereby is able to flip the magnetisation of the film . After exposing the film to the beam, the film was examined by high-resolution magnetic domain imaging microscopy. It was found that due to the high power of the e-beam material was evaporated in the region where the beam had hit the film. Thereby, a spatial image of the beam shape was obtained showing more structure than was known previously. In the outer regions of the film, regions of reversed magnetisation were observed, indicating that the spin had rotated according to the Landau-Lifshitz equation [2] describing spin rotation induced by a magnetic field pulse. The specifications of the TTF-FEL are somewhat different than in the experiment described above. The bunches are much shorter, but the energy is only 1 GeV compared to 50 GeV at SLAC. This provides additional possibilities to study magnetic switching phenomena. We propose to insert a facility for this kind of experiments downstream of the undulator to use the beam before it is dumped. This additionally might serve for beam diagnostics.

b.) Magneto-optical microscopy in the XUV spectral regime

We propose to extend the magneto-optical microscopy towards the XUV regime. Especially, it has been shown recently by F.U. Hillebrecht et al. [3] that the optical reflectivity for p-polarized light depends strongly on the direction of the sample magnetisation at 3p core level thresholds. The change in reflectivity is more than 20 % upon reversing the sign of the magnetisation and more than an order of magnitude larger than the corresponding transverse magneto-optic Kerr effect in the visible. The effect can be used either for a scanning magnetic domain microscope or for an imaging microscopy if suitable optics will be available. This would allow for element specific imaging of magnetic structures in the nm scale regime. This technique immediately can be extended to time-resolution making use of the bunch-structure of the radiation. The time scales of interest range from seconds to at least picoseconds. Information on the switching behaviour of magnetic films and on critical fluctuations when approaching the ferromagnetic phase transition can be obtained.

c.) Spin-resolved photoelectron spectroscopy on magnetic surfaces

Electronic structure investigations

Spin-resolved photoemission from magnetic surfaces can either yield magnetic - or electronic structure information, preferably both if the intensity is allowing. Using a pump- probe technique, a first conventional laser beam for heating the sample, and as the second beam the FEL radiation, one could cause a thermal expansion of the lattice by the first pulse and could probe the change in the spin-split electronic structure by the spin-resolved valence band photoemission using the FEL laser. High or very high energy resolution (< 100 meV) would allow to investigate the changes which occur

close to the Fermi energy.

Dynamics of the Spin Relaxation in Magnetic Systems

Upon raising the temperature of a ferromagnet above its Curie Temperature the macroscopic spin orientation and alignment is destroyed. This phase transition has been investigated for many bulk and thin film magnetic systems using quasi static experiments, where the temperature is only raised adiabatically. Very little, however, is known about the dynamics of the spin-lattice coupling and the exact mechanisms leading to the spin disorientation. Here we propose to investigate these phenomena using a laser pulse from an external synchronised fsec laser to heat the system and a second time correlated TTF-FEL-pulse to probe the magnetic state of the system. Spin lattice relaxation times extracted from similar experiments are quoted to vary from a few psec in Gd [4] to somewhere between a few psec and 20 nsec in Fe [5]. These questions are not only of basic scientific interest, but also establish the fundamental limit for magneto-optical recording processes. In magneto-optical recording a focused laser beam is used to raise the temperature of the recording medium, typically a rare earth transitions metal magnetic alloy, above the Curie temperature, and subsequently the medium is allowed to cool down in the presence of a fairly weak external field. The direction of this field is thus transcribed onto the medium spatially restricted to the spot where the temperature exceeded the critical temperature.

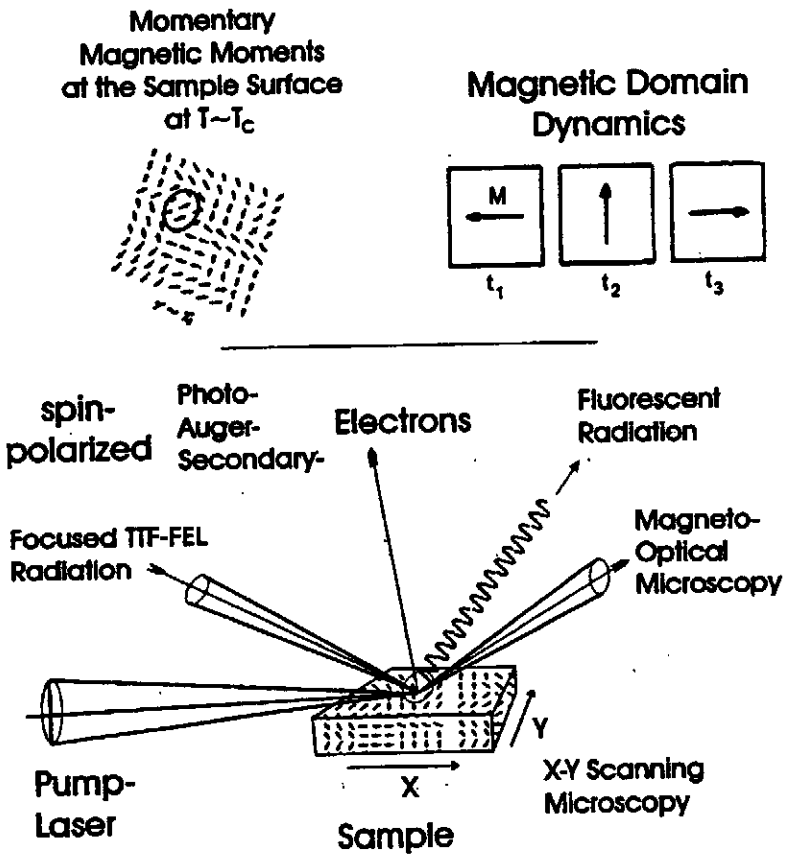

Fig. 3.2.4: Experiments with TTF-FEL radiation on Magnetism.

The processes of short high power electronic excitations in solids have been mostly investigated for semiconductor systems [6]. Fewer studies have been carried out for metals [7]. Initially in the photoabsorption process electronic excitations are created by the intense laser field of the pump pulse. Subsequently the excited carriers cool down by electron-electron and electron-phonon scattering processes. Thus the temperature rise is transferred from the electronic system to the lattice. This generally happens on the psec timescale. The main question for the magnetic systems remains on what timescale this rise in the lattice temperature (phonon population) will destroy the macroscopic orientation of the magnetic moments.

We propose a pump-probe experiment to study these effects using the TTF-FEL pulses to probe the magnetic state of the sample whereas a second external synchronised f-sec laser will be used to "heat" the sample. The high photon energy of the TTF-FEL is essential for the probe beam to excite Auger electrons of the sample, which will be recorded with an electron energy analyser and a subsequent Mott detector. The macroscopic spin polarisation recorded in the Auger spectra serves as element specific information about the orientation of the magnetic moments of particular atoms within the sample [8]. Thus even for complex multi element samples, like the magnetic alloys used for magneto optical recording, the magnetic orientation of one particular atomic species may be selectively probed on a timescale limited by the accuracy of the synchronisation and by the inherent pulse widths of the TTF-FEL and the pump laser.

A few experiments addressing these questions have been carried out so far, mostly by scientists from ETH Zürich. They used a 20 nsec laser beam to heat the sample and a psec probe pulse to excite and observe either low energy (secondary) electrons or to observe the Kerr rotation of the reflected laser beam. The experiments proposed here, using the TTF-FEL facility, will first of all considerably improve the time resolution of these studies. Furthermore, the possibility to excite and detect Auger electrons adds a new dimension to this kind of investigations. The spin polarisation of the Auger electron will serve as an indicator of the orientation of element specific magnetic moments within the sample. The total (secondary) electron yield or the Kerr effect on the other hand, serve only as an indicator of the total magnetic state of the sample. Neither one of these signals is element specific or particularly surface sensitive.

The direct TTF-FEL beam can be used for these experiments without further monochromatization. Obviously, the intensity of the TTF-FEL beam has to be controlled carefully in order to not inflict any permanent changes or damage to the sample. The Auger electrons excited by the TTF-FEL pulse will be detected by an electron energy analyser with a Mott detector. As a secondary laser system we could bring a Ti-Sapphire f-sec laser system we are currently setting up in our laboratory. This system delivers 200 f-sec pulses at 800 nm wavelength with a pulse-energy of 2 Gd at a repetition rate variable between 10 kHz and 300 kHz. The peak power of this laser is more than sufficient for the heating, whereas on the other hand the probability to excite Auger electrons with such a beam is negligible, even taking multiphoton ionisation into consideration. The main problem that has to be solved is the sychronisation of this Ti-Sapphire laser to the FEL pulse, which possibly can be done by triggering the Q-switch of the f-sec amplifier with a trigger signal provided by the TTF-FEL. The repe-

tition rate of the pump laser also implies that only every third micro pulse of the TTF-FEL can be used.

Spatially and spin-resolved photoelectron spectroscopy

The high brightness of the FEL will make spatially spin-resolved photoelectron spectroscopy possible. The easiest method is to use a scanning technique with fine-focused radiation. This has a strong potential for the investigation of technical magnetic materials (magnets etc.) which generally are inhomogeneous. Furthermore, the ultimate goal might be to combine spatial resolution with time resolution in spin-resolved photoemission. This would be of strong interest in the physics of magnetic phase transitions, complementary to the information obtained from magneto-optical microscopy because of the different information depths of these spectroscopies.

d.) Dichroism spectroscopies and microscopies on magnetic surfaces

Dichroism in photoemission discovered in the past years [9, 10, 3] allows to investigate a subset of magnetic properties without the need of measuring the spin polarisaion (full information is only obtained by also measuring the spin polarisation). The linear polarisation obtained with a planar undulator can be used in photoelectron microscopy using a photelectron emission microscope (PEEM) to investigate magnetic structures element-specifically. In a static mode, one would use a fine-focused FEL beam of energy near the 3p thresholds (60 eV) of the ferromagnetic transition metals to improve the spatial resolution to the nm scale. Magnetic contrast is achieved e.g. by varying the photon energy by some eV.

Dynamics of magnetic domains at surfaces and in thin films

A number of studies in recent years have been devoted to the investigation of static domain patterns at surfaces and in low-dimensional systems. Mainly based on the use of scanning electron microscopy with a spin-polarization analysis (SEMPA) the aim of these investigations is an improved understanding of the micromagnetism [11]. Being a scanning type technique, however, SEMPA is hampered by its sequential data acquisition procedure and is thus inherently slow. Besides the structure of a static domain pattern, micromagnetic processes govern also the dynamic response of a domain system. Magnetic materials that are subjected to an external magnetic field show a characteristic hysteresis behaviour. The dynamic response of a magnetic material during magnetization reversal is tremendously important for many technological applications of ferromagnets. In order to decisively improve the performance of magnetic materials, it is therefore important to understand the fundamental physics behind a hysteresis loop.

Seen on a microscopic scale several processes contribute to a magnetization reversal

in an external field [12]. If we start from a single-domain state, there is first of all, the nucleation of magnetic domain walls. These domain walls may nucleate spontaneously or at defects in the sample. Also the edges of a sample of finite size may be seen as defects in that respect. The formation of a domain pattern is intimately connected to the magnetic anisotropies in the material. At somewhat higher field, the domain walls start to move, thereby increasing the size of the domains with a magnetization vector along the external field at the expense of those with a magnetization vector opposite to the external field. This process leads again to a single domain state, but with the magnetization reversed as compared to the starting point of the cycle. In cases in which the magnetization vector of the single domain state makes an angle with the external field, additionally a coherent rotation of the magnetization in the individual domains takes place.

The microscopic mechanisms involved in magnetization reversal have been extensively studied in both experiment and theory for bulk samples. Very little work, however, has been devoted to the domain dynamics at surfaces or in thin films. This must be seen on the background of an increasing importance of thin film systems in the field of magnetic recording. The main problem encountered in the application of conventional domain imaging techniques to the field of surface magnetism is the insufficient surface sensitivity. The classic magneto-optical Kerr microscopy which has been used to a great extent in bulk magnetism is no longer applicable in the monolayer regime. Scanning techniques, such as SEMPA, are too slow. As an alternative approach, photoemisssion microscopy techniques exploiting the effect of magnetic dichroisms are currently developed [13, 14]. In a photoemission microscope, the sample is illuminated with radiation in the UV, XUV, or soft X-ray regime. The spatial distribution of the emitted electrons from a small area of the surface is collected by means of an immersion lens objective and projected onto an electron multiplier unit. This way a magnified image of the sample surface is formed. By introducing an energy filter between objective and projective lens, the image can be generated by electrons of a defined kinetic energy, thereby containing element-specific information. This permits chemical analyses of a surface with a lateral resolution of currently 30 nm. An additional magnetic contrast can be introduced by means of magneto-dichroic effects. A magnetic dichroism appears as a change in the photoemission intensity distribution when the magnetization direction changes with respect to the direction of the incoming light. These phenomena have been observed with circularly and linearly polarized light, the latter being of particular interest for the use of the TTF-FEL radiation.

With photon energies in the range of 30 eV to 200 eV the light of the TTF-FEL provides access to both valence band electrons and shallow core levels. In the latter case we can combine magnetic and element-specific information. Of crucial importance for the experiment is both the peak intensity and the time-structure of the TTF-FEL radiation. The intensity in a single pulse must be high enough to permit the acquisition of an image with reasonable signal to noise ratio. The readout of the image processing system is synchronized with the sequence of pulses in a bunch. By this stroboscopic technique the fast magnetization changes can be recorded in "slow motion". With the projected maximum number of pulses in a bunch train (7200) an ultimate time resolution of the order of microseconds can be achieved. The photoemission microscope em-

ployed for these experiments will be optimized for a large field of view (>= 500 μm) at a moderate spatial resolution of about 100 nm.

Intrinsic dynamics of magnetic domain walls at surfaces and in small particles

These studies will focus on the magnetization dynamics *inside* the domain walls of a ferromagnet. In order to access the details of a domain wall, a photoemission microscope with a very high spatial resolution of better than 10 nm is needed. The sample is subjected to a weak DC or AC magnetic field. The response of the magnetization in the domain walls is observed by a similar stroboscopic imaging technique as already proposed above. Of particular interest are the conditions under which the domain walls start to move or under which a rotation of the magnetization inside the wall takes place. Closely related to the latter issue is the behaviour of the magnetization in small particles. If these particles are smaller than typical domain wall widths (approx. 100 nm), no domain walls are formed and therefore a coherent rotation of the magnetization should prevail. Two aspects of this project should be emphasized. First, the experiments at surfaces aim at the very basis of micromagnetism. We can expect new insights into the physical processes governing the magnetism on a microscopic or even mesoscopic scale. This offers a unique possibility to test the validity of current micromagnetic theories and give suggestions for their improvements. Second, theses investigations will give a completely new view into the micromagnetism of small particles. This knowledge is of considerable importance for the understanding of the magnetic behaviour of granular materials and thus of great technological relevance.

e.) Nonlinear magneto-optics with the TTF-FEL radiation

Nonlinear optical effects in connection to magnetism have been observed only very recently in the regime of visible light [15, 16].They are a consequence of the fact that the tensor of the nonlinear susceptibility contains a number of elements which depend on magnetic fields. As a consequence, the polarization and the intensity of the frequency-doubled light depends on the magnetization in the sample. This finding is currently used to develop a method called nonlinear magneto-optical Kerr effect (non-linear MOKE) for the investigation of magnetic materials. Of particular importance is the fact that the process of second harmonic generation is bound to regions in the sample where the crystalline symmetry is broken, e.g., at surfaces and interfaces [7]. Because the information depth is essentially limited by the absoption of the 2ω light in the sample, buried interfaces can be probed this way. This effect has therefore a great potential for the magnetic investigation of technological magnetic structures.

So far non-linear MOKE is limited to the visible and UV region by the available lasers. Given a suitable light source, such as the TTF-FEL, an extension of this method to the XUV seems feasible. By accessing the shallow core-levels, the interface sensitivity could be combined with a chemical selectivity. This opens the pathway for a whole class of new and unique experiments in interface magnetism.

The short pulse length of 450 fs and the high peak power of the TTF-FEL radiation is

of particular importance for such an experiment, as the process of frequency-doubling requires the presence of a strong electric field in the sample. At the same time, the energy deposited in the system must be limited in order not to exceed the damage level of the sample or to destroy the magnetic order. Currently titanium sapphire lasers are used for this purpose. The energy range of the TTF-FEL light can be conveniently used to perform optical excitations involving the shallow core-levels in most of the ferromagnetic 3d and 4f materials. Using this type of optical transitions, the non-linear MOKE gains elemental specificity. This enables one to determine the magnetic properties of the various constituents in a magnetic multilayer at the interfaces. The only other method yielding a comparable information is Mößbauer spectroscopy [18]. It involves, however, very time-consuming measurements and the preparation of particular samples containing an appropriate isotope of the chemical element of interest. An element-specific version of the non-linear MOKE, which can be only realized with a dedicated light source, such as the TTF-FEL, will thus give a much better access to the magnetic phenomena occurring at buried interfaces.

f.) Fluorescence spectroscopy

In recent workshops on magnetism it was pointed out by B. Gyorffy (Bristol) that the study of fluorescence radiation after core electron excitation yields new information on the excitation dynamics in magnetic materials. Especially, *time-resolved* experiments would be feasible due to the outstanding brightness of the FEL. With the sub-ps time resolution available at the TTF-FEL the study of phonons related processes in finite temperataure magnetism would be possible.

References :

1. H.C. Siegmann et al., submitted to Phys. Rev. Lett. (1995)

2. L. Landau and E. Lifshitz, Phys. Z. Sov. 8, 135 (1935)

3. F. U. Hillebrecht et al., submitted to Phys. Rev. Lett. (1995)

4. A. Vaterlaus, T. Beutler, F. Meier, Phys. Rev. Lett. 67, 3314 (1991); A. Vaterlaus, T. Beutler, F. Meier, J MMM 104, 1693 (1992)

5. A. Vaterlaus, T. Beutler, D. Guarisco, M. Lutz, F. Meier, Phys. Rev. B46, 5280 (1992)

6. "Hot Carriers in Semiconductor Nanostructures", ed. by J. Shah Academic Press (1992)

7. R.W. Schoenlein, W.Z. Lin, J.G. Fujimoto, G.L. Easley, Phys. Rev. Lett. 58, 1680 (1987)

8. E. Kisker, K. Schröder , A. Bringer, Solid State Comm. 55, 377 (1985); M. Landolt, Appl. Phys. A41, 83 (1986)

9. L. Baumgarten et al., Phys. Rev. Lett. 65, 492 (1990)

10. Ch. Roth et al., Phys. Rev. Lett. 70, 3479 (1993)

11. H. P. Oepen and J. Kirschner, Scanning Microscopy 5, 1 (1991)

12. B.D. Cullity, Introduction to magnetic materials (Reading, Addison-Wesley) (1972)

13. J. Stöhr, Y. Wu, M.G. sarmant, B.D. Hermsmeier, G. Harpü, S. Koranda, D. Dunham and B.P. Tonner, Science 259, 658 (1993)

14. C.M. Schneider, K. Holldack, M. Kinzler, M. Grunze, H.P. Oepen, F. Schäfers, H. Petersen, K. Meinel and J. Kirschner, Appl. Phys. Lett. 63, 2432 (1993)

15. J. Reif, J.C. Zink, C.M. Schneider and J. Kirschner, Phys. Rev. Lett. 67, 2878 (1991)

16. J. Reif, C. Rau and E. Matthias, Phys. Rev. Lett. 71, 1931 (1993)

17. U. Pustogowa, W. Hübner and K.H. Bennemann, Phys. Rev. B 48, 8607 (1993)

18. M. Przybylski, J. Korecki and U. Gradmann, App. Phys. A 52, 33 (1991)

3.3 Interaction of Electron Pulses from the TESLA-Test Facility with Condensed Matter

3.3.1 Introduction

The interaction of the high current low emittance 1 GeV electron beam from the TTF with matter presents attractive perspectives for research in various fields of physics, and material sciences. Several advantages in comparison with synchrotron radiation sources exist among which are that (i) materials can be brought into the electron beam and be studied with new interferometric methods, and (ii) that extremely high brilliant x-ray flashes can be produced which, in addition, can be triggered. In this contribution a research program is outlined which aims to explore, at the TTF, the physical background of such phenomena. This program is intimately connected with a research program already initiated at the Mainz Microtron MAMI. Processes under investigation here are (i) transition radiation in the x-ray region (XTR), (ii) parametric x-ray radiation, (iii) undulator radiation, and (iv) Smith-Purcell radiation (SPR). At the superconducting Darmstadt S-DALINAC also parametric x-ray radiation, and in addition (v) channelling radiation is being studied at somewhat lower beam energies. The main difference between the TTF and the 855 MeV MAMI accelerator, with a vertical emittance of 1 π nm rad (1σ), is that MAMI delivers an cw-electron beam with a current of up to 100 μA. The various aspects connected with high current electron pulses from the TTF to be discussed in the following section cannot be studied at MAMI.

3.3.2 Effects of the strong electric and magnetic fields in the interaction with matter

The TTF will deliver bunches with a charge of 1 nC, a duration of 400 fs, and a peak current of 2700 A. If such a bunch is radially focused to a radius R, a strong static electric field of E_0 = 16/ (R/μm) [V/Å] is produced at the periphery of the charge distribution which is assumed to be homogeneous over the whole bunch. Also a strong static magnetic field B = 540/ (R/μm) [Tesla] is associated with the bunch. Since the number of electrons per unit length in the bunch is high (dNe/dz = 5.6 10^3/Å) field fluctuations are rather small and the field can well be considered as static. The radial dependence of the fields inside the charge distribution is proportional to r and outside proportional to 1/r.

a.) Non-linear optics

During the passage of a high current bunch of the TTF through matter strong electric and magnetic fields act on the atoms or molecules. The electrical field strength of 16 V/Å is close to the critical field strength $E_{0crit} = e/a_0^2 = 51.4$ V/Å which the electron in a hydrogen atom experiences. The magnetic field strength is even higher than $B_{0crit} = 157.5$ Tesla which the Bohr electron in a hydrogen atom produces at the origin. If fields of this order of magnitude interact with matter, strong non linear polarization effects may be expected. In transparent media these effects can be studied with a pulsed probe laser beam which is synchronized with the electron beam pulse. Strong birefringence effects, even in isotropic media, are expected and can be studied with the probe laser by various kinds of interference phenomena. Some of these effects will be large, since electro-optical phenomena such as the Kerr or Faraday effect can already be observed with quite moderate field strengths in the laboratory. With high power lasers even second harmonic generation in isotropic media may be observable.

In addition, one may investigate depolarization of ferro-electric and ferro-magnetic matter [1] under the action of very short and strong electric and magnetic field pulses. The depolarization should depend on the fields multiplied by the time, i.e. on the action, and may be studied with one pulse or well defined trains of pulses.

b.) Non-linear x-ray optics

It is an interesting question whether or not non-linear phenomena due to the high static fields can be observed also at very high frequencies, i.e. in the soft x-ray regime. Very little is known in this field. Among the very few publications the paper of Eisenberger and McCall [2] should be mentioned in which observation of parametric down conversion of x-rays in crystals was reported. Since non-linear phenomena in the x-ray region are expected to be connected with inner shell electrons the critical field strength is $E_{crit} = Z^2$ 51.4 V/Å which scales with Z^2. Therefore, non-linear effects in the inner shells are expected to decrease rapidly with increasing Z. They are probably detectable only for very low Z materials. Possible experiments of this type include harmonic generation, and the measurement of the quadratic Stark shift of core levels in isotropic or anisotropic matter [3- 5].

3.3.3 Transition radiation as an intense hard x-ray source

If an electron passes a single interface between a medium and vacuum, broad band electromagnetic radiation is produced. The radiation characteristics resembles a Lorentz transformed dipole radiation pattern with maximum intensity at an angle $\theta = 1/\gamma$.

The energy spectrum extends up to a gradual cut-off energy $\gamma\hbar\omega_p$, with ω_p the plasma frequency and γ the Lorentz factor. Using beryllium as a radiator material the cut-off frequency at the beam energy of 1 GeV is as high as 51 keV. The radiation is emitted in a cone with an apex angle of about 1 mrad. Similar to the directional properties of synchrotron radiation transition radiation is strongly forward directed. In order to increase the number of photons produced a radiator may be chosen in which the electrons traverse many interfaces, i.e. a stack of thin foils. In this case interference effects of the individual interfaces must be taken into account leading to a modulation of the energy and angular distribution from a single interface which has been observed experimentally [4].

Calculations based on these experimental results show that a hard x-ray beam with photon energies up to about 40 keV can be produced from a stack of 30 beryllium foils with 30 μm thickness and 70 μm separation. At a photon energy between 30 and 40 keV a spectral brilliance B = 10^{15}/ (s mrad^2 mm^2 10^{-3} BW) should be reached at a mean beam current of 100 μA. This number compares well with the brilliance from bending magnets of a synchrotron radiation source like the ESRF with an energy of 6 GeV [6].

A number of about 10^5 photons/10^{-3} BW is emitted from one micro-pulse filled with a charge of 1 nC. A pulse train of 6400 micropulses forms a macro-pulse with a duration of 0.8 ms. About 10^9 photons/10^{-3} BW are emitted from such a macro-pulse. These very high photon fluxes may be applied for imaging of ultra-fast and fast processes, repectively.

The x-ray spectrum is superimposed on a high energy bremsstrahlung background which extends up to the energy of the electron beam. The intensity is about one order of magnitude lower as the numbers quoted in the last paragraph. One might take advantage from this highly brilliant hard gamma-ray beam as well. As an example, positronium life-time measurements in condensed matter are mentioned. Detailed information about material fatigues are expected from such measurements [7]. Since the positronium life-time is in the 100 ps range the sensitivity strongly relies on a good time resolution which is about 300 ps when using radioactive positron sources. If the start signal is taken from the accelerator instead of from a gamma-ray a considerable improvement of the sensitivity can be achieved.

3.3.4 Conclusion

To implement the research program outlined above a dispersion free beam line is needed in which the electron beam can be focused on the target to a spot of about 1 μm diameter. Downstream from the target chamber, an additional bending magnet is required which deflects the beam into the dump. In this arrangement the radiation from the target is separated from the electron beam and can be detected in forward di-

rection. Since the background at the detector position must be kept to a minimum the observation direction downstream from the target should not be coincident with the accelerator beam axis. Consequently, upstream from the target chamber at least one additional bending magnet is required.

Finally it should be mentioned that parts of the community working in this field of physics want to use the pulsed beam from the 20 MeV injector for various kinds of experiments including experiments on channelling and Smith-Purcell radiation.

References:

1. H.C. Siegmann et al., submitted to Phys. Rev. Lett. (1995)
2. P. Eisenberger, S.L. McCall, Phys. Rev. Letters 26 (1971) 684
3. H.A. Bethe, E.E. Salpeter, Quantum Mechanics of one- and two- elctron atoms, Springer-Verlag Berlin, Göttingen, Heidelberg (1957) 233
4. H. Backe et al., Z. Physik A 348 (1994) 87
5. H. Backe et al., to be published
6. R. Haensel, Phys. Bl. 50 (1994) 1039
7. A. H. Walenta, Universität Siegen, private communication

4 Experimental Techniques

The TTF-FEL radiation can be used for very different types of experiments exploiting the high intensity and brightness to produce extremely high power densities in a small area or to filter out a narrow energy band for spectroscopic studies at ultra-high energy resolution. Most experiments will require optical elements to focus or diffract the photon beam. The FEL beam could be used more efficiently by switching between two separate beamlines using plane mirrors as far upstream as possible. It appears thus necessary to start with a brief discussion of possible damage to mirrors and other matter due to the extreme power density of the FEL radiation. The results of this discussion will aid in finding appropriate concepts for a possible optical layout of the experimental hall and for a high resolution monochromator.

4.1 Radiation damage

The average thermal power of approximately 70 W can be handled using standard cooling techniques similar to those employed on modern undulator beamlines. However, the extraordinary high density of $3.5*10^{13}$ photons within a 400 fsec long pulse, corresponding to a peak power of 2.7 GW at the minimum design wavelength of 6.4 nm, poses a very serious problem for all optical components. The situation is even more difficult because the FEL beam is highly collimated, resulting in very high power densities even at large distances (see table 1). These power levels are much larger than threshold values for laser ablation at optical wavelengths (~0.1 to several hundred GW / cm^2 depending on the material and on the pulse length), thus the interaction between the FEL soft x-rays and matter has to be considered in more detail.

distance (m)	**diameter** (mm)	**peak power** (GW/cm^2)	**photon density** ($phot./cm^2$)	**energy** (J/cm^2)
5	0.26	5100	$6.6*10^{16}$	2.1
10	0.48	1500	$1.9*10^{16}$	0.6
30	1.41	170	$2.2*10^{15}$	0.07

Table 1: Photon beam diameter, peak power and photon density per pulse (for 6.4 nm photons) at different distances behind the undulator.

In the VUV region the primary process is photoionisation. Typical photoionisation cross sections and penetration depths for some elements are given in table 2. Obviously the situation becomes worse at lower photon energies: The cross sections increase (except when crossing an ionisation threshold), and at the same time also the number of photons increases since the peak power of the FEL photon beam is expected to be nearly independent of energy. Therefore, for many chemical elements

	σ (Mb) 50 eV	λ (nm) 50 eV	ε (eV/at.) 50 eV	σ (Mb) 100eV	λ (nm) 100eV	ε (eV/at.) 100eV	σ (Mb) 200eV	λ (nm) 200eV	ε (eV/at.) 200eV
C	1.8	50	23	0.48	185	6	0.1	780	1.5
Si	0.4	546	5	5.4	37.6	70	3.3	61.3	42
Ni	9.0	12	119	6.4	17.2	84	2.6	42.9	33
Ge	4.7	49	62	7.3	30.8	97	5.5	41.7	70
Au	16.8	10	215	3.7	46.7	48	2.4	73.5	30

Table 2: Photoionisation cross section, σ, penetration depth, λ, and average amount of absorbed energy per atom, ε, at photon energies of 50 eV, 100 eV and 200 eV in 5m distance from the undulator where one would like to put the first mirror (1 Mb = 10^{-18} cm^2).

the probability for photoionisation is near unity if an atom is put into the photon beam at a distance of 5 m from the undulator. This is also reflected in the average amount of energy, ε, absorbed per atom in the absorption volume (table 2). In general ε is several tens of eV per atom, only in selected cases such as carbon below the ionisation threshold for a 1s electron and Si below the 2p threshold values below 5 eV per atom are found. Even for a metal it is not obvious whether the surface will not evaporate if nearly all atoms within the absorption volume are ionised at the same time. (Note that the lifetimes of core levels are significantly shorter than the pulse width of 400 fsec. In the VUV, however, particularly low cross sections are found for elements where only valence electrons can be ionised, such as C and Si. These states may have lifetimes of the same order as the pulse length.)

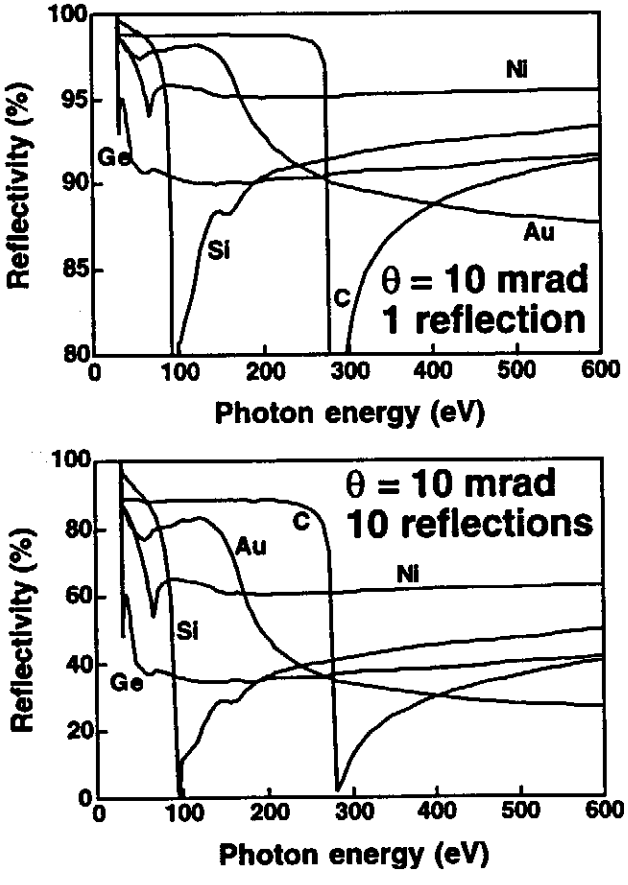

Figure 1: Reflectivity of mirrors with different coatings at grazing angles of 10 mrad. Top: 1 reflection; bottom: 10 reflections.

In order to minimize the problem of laser ablation one has to use coatings with low absorption cross sections on all critical components and grazing angles of incidence, θ, for all reflectors. A small angle θ not only dilutes the photon density on the mirror surface but also leads to a high degree of total reflection reducing the absorbed power density by several

orders of magnitude. The reflectivity of some possible mirror coatings for the energy range of the TTF-FEL is shown in fig. 1 for $\theta = 10$ mrad. A value of approximately 99 % is calculated for carbon below 240 eV, and even slightly more for Si below 60 eV. In order to reach a similar level for energies above the carbon K-edge one could use Ni at $\theta = 2$ mrad. The density of absorbed photons can thus be reduced to some 10^{12} per cm^2, i.e. less than 1 GW / cm^2. Even in the worst case, if all these photons would be absorbed in the topmost surface layer, only about every 1000th surface atom would be ionised initially. It is difficult to estimate at which distances and angles mirror degradation is acceptably low; it will be necessary to determine this experimentally.

4.2 Layout of the experimental hall

If it turns out to be possible to use mirrors at distances not larger than about 10 m from the undulator, then also other optical elements for focussing and diffraction further down-stream will survive, hence the deflected beam could pass through a monochromator for high resolution spectroscopy. In order to obtain a useful separation between an experimental area behind the monochromator and another one in the straight forward direction, an angle of approximately 10 degrees between the two lines would be desirable (fig. 2). This could be achieved by a series of 10 mirrors, each deflecting by an angle of 20 mrad. However, if it should be necessary to work at significantly lower angles, correspondingly more mirrors and space would be required. This would make the deflection into a seperate beamline much more difficult and in particular it would become impossible to build a high resolution monochromator within a distance of 40 m from the undulator.

All initial test experiments and photon beam diagnostics will be done in the direct FEL beam without any further deflection. Photon diagnostics includes the characterisation of the FEL photon beam with respect to all relevant parameters, i.e. total intensity, beam size and divergence, spectral distribution, intensity profile of a single pulse, time jitter between pulses and coherence. The direct beam is also ideally suited for all experiments which need the highest possible power density on the sample. An ellipsoidal mirror in a distance of approximately 30 m behind the undulator could focus the source into a spot of 1 µm thus giving peak densities of the order of $4*10^{21}$ photons / cm^2 or $3*10^{17}$ W / cm^2 or 0.1 MJ / cm^2 in a single pulse. At a sufficiently grazing angle the degradation of the mirror surface should be acceptably small.

4.3 High resolution monochromator

The most difficult task is the design of a monochromator with highest possible energy and spatial resolution despite of the high power levels. The design strategy is determined by trying to minimize the power density on the diffraction grating and the exit slit, keeping in mind that the situation becomes more critical towards longer wavelengths.

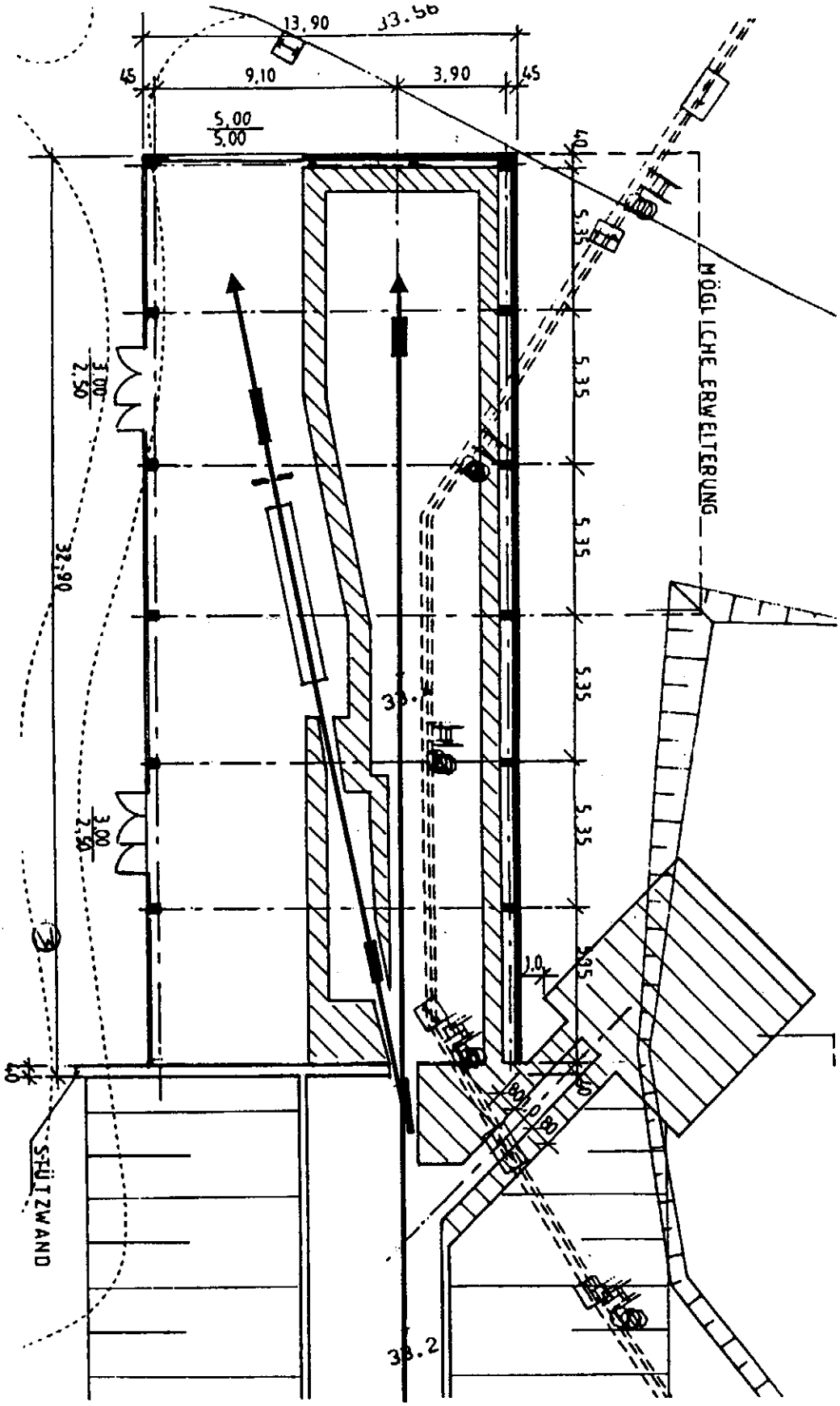

Figure 2; Possible layout of the experimental hall with two beamlines. The deflected beam passes through a high resolution grating monochromator and is focussed on the sample.

In order to reduce the power density on the diffraction grating as much as possible, it is necessary to use a pre-optics to diverge the photon beam and thereby distribute it over a large area of several tens of cm^2. Since at grazing angles of incidence on the grating a different beam divergence is required within and perpendicular to the dispersion plane, it suggests itself to use two separate plane-elliptical mirrors to demagnify the source by factors of the order of 10 and 100 in the vertical and horizontal direction, respectively (assuming a vertically dispersing grating). This also provides a small intermediate focus of ~10 μm which serves as the entrance slit for the monochromator. Moreover, a large number of grooves are covered by the photon beam making sure that the energy resolution will not be diffraction limited.

The angle of incidence on the grating itself, α_g, should be as grazing as possible, and in addition one should use the grating in positive first order to make this angle even smaller for longer wavelengths. Therefore a plane grating monochromator with constant focal distance such as the SX-700 [1] would not be the first choice since the overall deflection and hence α_g increase with increasing wavelength.

The second critical element is the exit slit of the monochromator since most of the power is contained in the already fairly narrow laser line, $\Delta\lambda / \lambda \sim 1$ %. Hence the dispersion of the monochromator should be large and it should not decrease for longer wavelengths. A Rowland circle design which has a constant dispersion, would be appropriate; the dispersion of a SX-700 type monochromator, in contrast, decreases with increasing wavelength. In addition the beam size perpendicular to the diffraction plane should be several cm at the exit slit. Consequently, a very long mirror is required to refocus the monochromatic beam into a spot of some μm diameter. The refocussing can also be done separately for the vertical and horizontal plane, similar to the pre-optics.

As a first approach and without further optimisation a Rowland circle monochromator with constant length similar to an instrument planned for BESSY II [2] has been chosen in order to obtain a rough idea about the possible performance of such an instrument and the power levels encountered for the optical elements. The results of this preliminary study are summarized in table 3. Also included in this table are some realistic parameters for a single focussing mirror in the direct FEL beam far downstream in the experimental hall (see fig. 2).

References:

1. H. Petersen, Opt. Commun. **40**, 402 (1982).
2. F. Senf, F. Eggenstein and W. Peatman, Rev. Sci. Instrum. **63**, 1326 (1992).

Monochromator (deflected beam)	
plane mirror	at 10 m, 10 mrad, power density ~15 GW / cm^2
vert. focussing mirror	at 14 m, 10 mrad, focus at 15 m, power density ~11 GW / cm^2
hor. focussing mirror	at 14.25 m, 10 mrad, focus at 14.4 m, power density ~11 GW / cm^2
grating	at 18.3 m, $2\theta = 8°$, R = 71.68 m, $\lambda = 6$ nm ($\alpha = 87.3°$), power density ~0.4 GW / cm^2
exit slit	at 25 m, power density ~5 GW / cm^2
hor. refocussing mirror	at 26 m, $\theta = 4°$, power density ~1 GW / cm^2
vert. refocussing mirror	at 28.6 m, $\theta = 2°$, power density ~1 GW / cm^2
energy resolution	$\lambda / \Delta\lambda \geq 20000$
focal dimension at the sample	≤ 10 µm
Focussing mirror (straight through beam)	
ellipsoidal mirror	at 30 m, 10 mrad, power density ~1.7 GW / cm^2
focal dimension at the sample	~1 µm (for 10 cm focal distance)
intensity per pulse at the sample	$4*10^{21}$ photons / cm^2, $3*10^{17}$ W / cm^2, 0.12 MJ / cm^2

Table 3: Possible parameters of the two beamlines (all distances measured from the source). The power densities are peak values of incoming radiation; a large fraction (up to 99 % depending on the angle of incidence and the coating material) will be totally reflected.

5 RF gun

5.1 Introduction

Both small emittance values and high phase space densities in all three dimensions are mandatory for achieving micro bunching and saturation within an undulator of reasonable length. To achieve a photon wavelength λ_{ph}, the transverse beam emittance ε_t (or normalized emittance ε_n, respectively) must not exceed a critical value given by, (see eq. 2.2):

$$\varepsilon_t = \frac{\varepsilon_n}{\beta\gamma} \leq \frac{\lambda_{ph}}{4\pi}$$

As will be discussed in section 11, this condition is not very strict. A Gaussian phase-space distribution is assumed in chapter 11, although it is not yet clear to which extent the beam from the gun will fit to this assumption. Preliminary simulations with other phase-space distributions have shown, however, little effect on the saturation length as long as the rms emittance is not changed. We aim for an rms emittance of 1 π mm mrad at 1 nC at the gun which gives us a safety factor of 2 for emittance dilution between gun and undulator.

Since no radiative damping occurs in the linac, the electrons have to be produced with the required emittance at the gun.

Thermionic guns are not able to supply the required phase-space densities. An essential break-through was the development of the RF gun by Fraser and Sheffield [1] in the mid-80s and the space charge emittance compensation scheme invented by Carlsten [2]. Table 5.1 compares TTF FEL design parameters with measured values obtained at other facilities.

	unit	TTF FEL gun	APEX	AFEL
charge	nC	1	1	1
norm emittance	π mm mrad	1	3.3	2.1
long emittance	keV mm	20	10.8	55.4
rf frequency	GHz	1.3	1.3	1.3
rf pulse duration	ms	1	0.1	0.01
repetition rate	Hz	10	1	10

Table 5.1: Comparison of TTF FEL gun parameters with gun parameters achieved at other laboratories. The product of rf pulse duration and repetition rate contributes to the heat load of the cavity.

Several recently developed rf gun designs achieve 1 π mrad mm in simulations, and measurements are on the way. A careful simulation of the gun performance has to include a number of small effects which can contribute to the emittance at the level of 1 π mrad mm, e.g. rf field asymmetries, wakefields.

Beside the emittance requirements of the TTF FEL gun, the heat load of the cavity due to the long rf pulse has to be considered. Since the TTF linac is based on

superconducting technology it allows the acceleration of long bunch trains at a high duty cycle (1%). Thus the average FEL radiation power is increased and a great flexibility with respect to the time structure can be offered. For the gun, normal conducting technology is more suitable since higher gradients can be achieved and normal conducting photocathodes can easily be integrated. Also focusing with external magnetic fields is impossible inside a superconducting cavity. The high duty cycle demands a powerful cooling of the gun. Cooling channels have to be integrated especially into the iris of the cavity. A gun with comparable heat load has been developed at BNL [3].

5.2 Basic principle

In an rf gun electrons are photo-emitted from a cathode which is placed in the split plane of an rf cavity. Hence the electrons experience a high electric field from the very beginning (typically about 30 MV/m in an L-band gun) and are rapidly accelerated, thus reducing space charge forces as quickly as possible. Since electrons start with nearly zero velocity, some phase slippage occurs with respect to the rf wave. The start phase ϕ_0 is chosen in a way that the electrons travel near the crest of the wave at the exit of the cavity. The start phase is an important parameter to trade off transverse versus longitudinal emittance. With a fine adjustment of the phase either the minimum transverse emittance or the minimum longitudinal emittance can be optimized.

The emittance of the electron beam is mostly affected by two contributions: rf field induced emittance and space charge induced emittance.

To first order both effects relate in the transverse plane to focusing or defocusing forces varying over the length of the bunch. Hence, the phase space ellipses at the center and the tails of the bunch rotate with different velocities in phase space and the projected emittance is increased.

Since in a FEL longitudinally separated slices of the bunch act independently of each other, the so-called slice-emittance, referring to particles within a longitudinal slice of the bunch, seems to be a more appropriate parameter than the projected emittance. However, in the TTF FEL three stages of bunch compression will be performed thus leading to a longitudinal mixing of slice emittances.

Note, that the rf force acts like a steadily increasing or decreasing force from the head to the tail of the bunch, while the space charge force is strongest in the middle of the bunch and decreases to both ends. Therefore Carlsten's emittance compensation technique works only for the space charge induced emittance and not for the rf induced emittance. For this reason the bunch charge and the bunch length have to be chosen in a way that the gun operates in a space charge dominated regime.

Due to the difference of the space charge forces in the middle and the tails of the bunch a fan-like structure opens up in phase space. This opening can be reversed by means of a focusing kick in a solenoid field. In the drift space behind the solenoid the phase space fan closes up again. When the projected emittance reaches its minimum value, a rapid acceleration will prevent it from growing again. Figure 5.1 shows schematically phase-space plots at the different stages of the beam line.

At the level of a few mm mrad the normalized emittance can be affected by a number of small contributions rather than being dominated by a single effect. Besides the thermal emittance, which will be discussed in connection with the photocathode, field asymmetries have to be considered.

The conventional way to couple into a cavity is to feed in power from a rectangular wave guide through a small hole in the outer cavity wall. This leads to a small field asymmetry which can cause emittance growth. Measurements at the BNL/SLAC/UCLA #3 rf gun indicate an emittance contribution of 1 π mm mrad [4] due to field asymmetries of a single asymmetric coupler. These measurements where done at a S-band gun. At L-band the field asymmetry is smaller due to the larger cavity dimensions. On the other hand also the beam dimensions tend to be larger in an L-band gun.

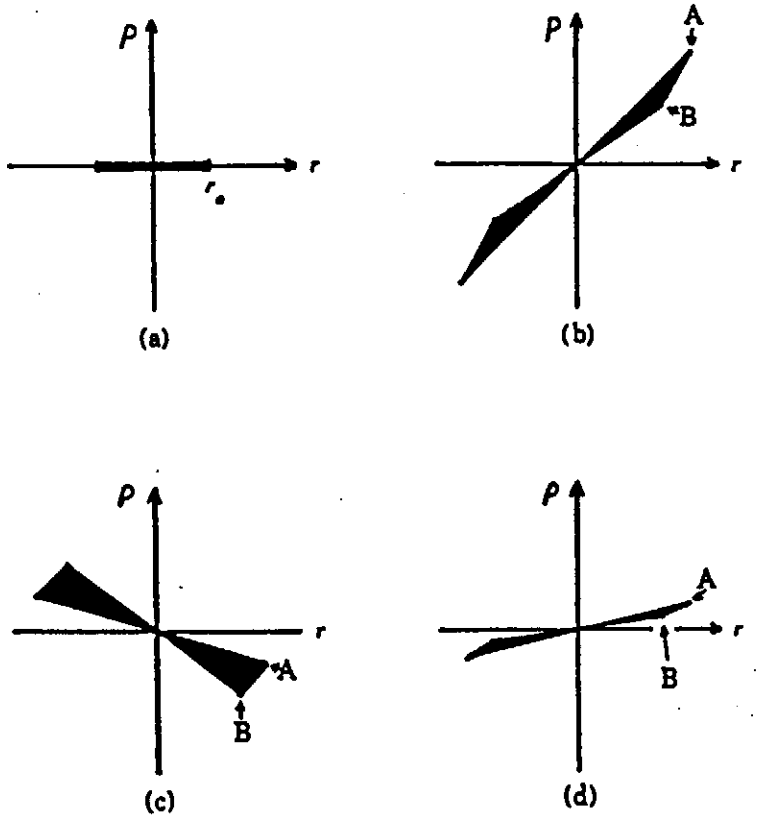

Figure 5.1: Transverse phase-space plots showing schematically transverse emittance growth and reduction. (a) initial phase-space with small emittance at the gun. (b) Phase-space after transport up to the lens, showing the emittance growth due to the different rotation velocities of the beam center (point A) and the tails (point B). (c) Phase-space immediately after the linear lens, showing rotation due to the lens. (d) Phase-space after drift behind lens, showing emittance reduction due to different velocities of rotation of the beam center and the tails, thus compensating the corresponding effect shown in (b).

5.3 The gun

We have started optimization of a 1 1/2 cell L-band, π-mode cavity. A gun with more cells would require a klystron with higher power and a longer drift space between gun and booster cavity. On the other hand emittance control in the booster cavity might be easier with a more energetic beam from a multi-cell gun. In order to reduce field

asymmetries we consider a coaxial input coupler as shown schematically in figure 5.2. The laser and the electron beam pass through the inner conductor. This scheme avoids field asymmetries and offers more flexibility in the positioning of the solenoid. The rotational symmetry of the structure is preserved, thus the mechanical stiffness of the cavity is increased and cooling is somewhat simplified.

The geometrical dimensions of the cavity have been optimized in order to minimize the emittance growth caused by the rf field. Transverse non-linear fields are sufficiently suppressed since the thick iris approximates the optimum aperture shape near the iris hole, prescribed by [5]:

$$r(z) = \sqrt{a^2 - \left(\frac{4d}{\pi}\right)^2 \ln\left(\sin\frac{\pi z}{2d}\right)}$$

(z = the longitudinal co-ordinate, d = length of half cell, a = aperture radius at z = d and r(z) = iris radius at position z)

Figure 5.3 shows a plot of the electric field in the gun. The field in the region of the input coupler is smooth and comparable to the field propagating into a tube. Table 5.2 lists rf parameters of the gun.

Optimization of the beam dimensions as well as the focusing solenoid field, its position and strength is underway.

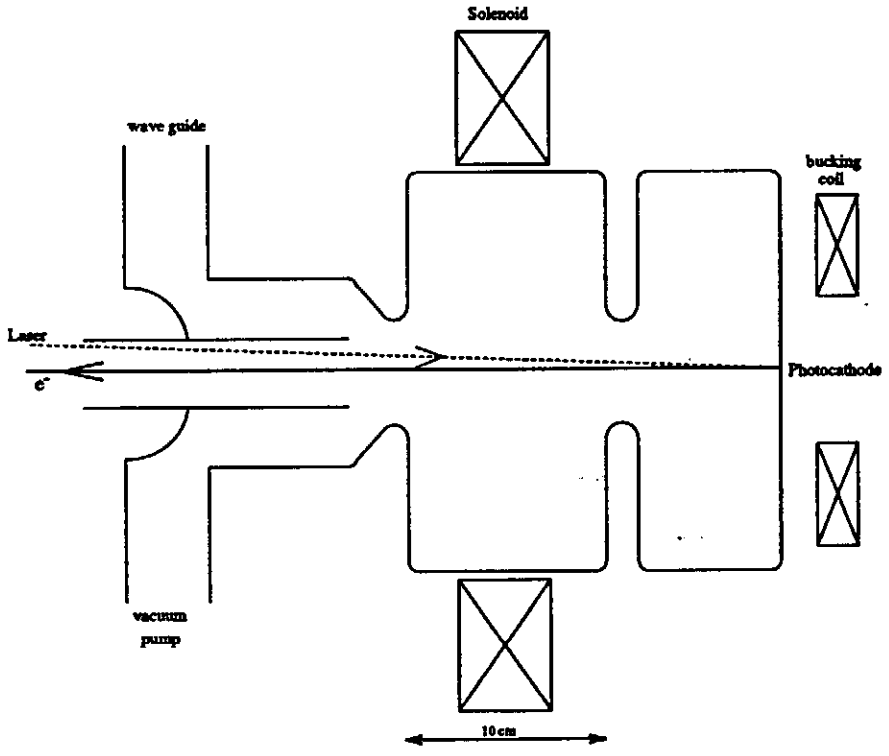

Figure 5.2: Schematic drawing of the TTF FEL rf gun with a coaxial input coupler.

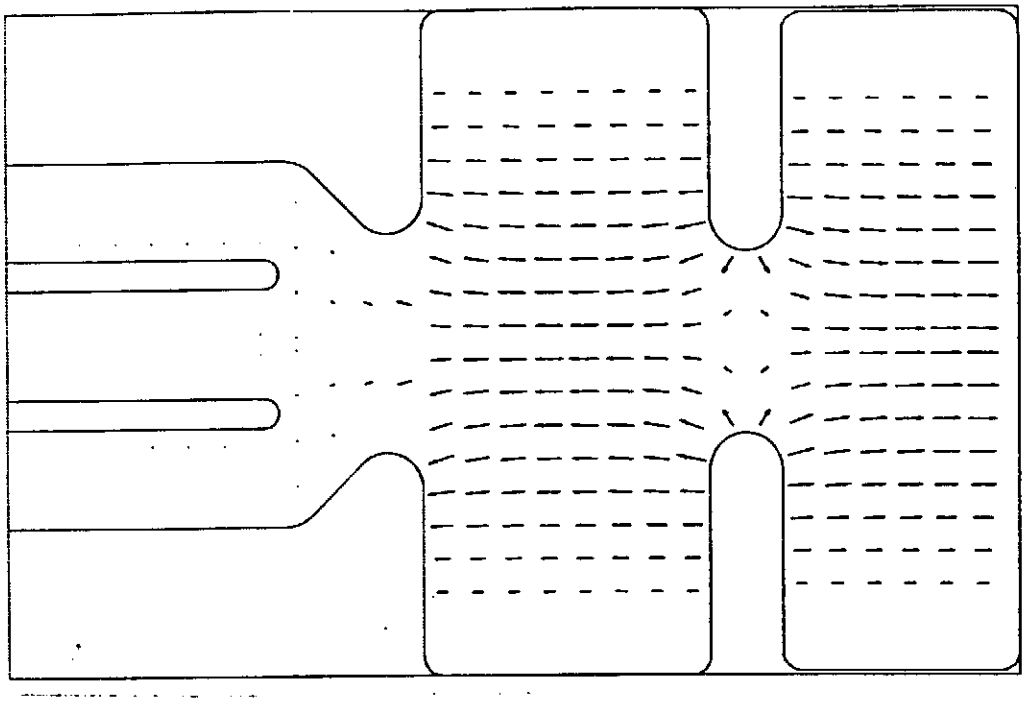

Figure 5.3: Electric fields in the TTF FEL rf gun

input power	4.5 MW
Q value	22700
max. gradient on cathode	50 MV/m
max. energy gain for a particle starting with β=0 on the cathode	5.68 MV

Table 5.2: RF parameter of the TTF FEL gun

A bucking coil will be used to adjust the solenoid field at the cathode. A zero field at the cathode is necessary in order to avoid emittance growth of the beam when it leaves the solenoid field.

The gun is followed by a drift space of about 1m length which includes the laser port. The super conducting booster cavity has to be protected from dark current from the gun. Hence clean up collimators will be included in the drift space as proposed for the TTF gun.

In order to reduce the production of dark currents the cavity will be cleaned by means of high pressure rinsing. In addition hot isostatic pressuring (HIP) of the copper for the gun is considered. Experiments at KEK have shown a great improvement of cavities treated with HIP in high gradient tests [6].

The rms emittance of an rf gun is in general increased by a halo of particles in long non-gaussian tails. By clipping ~5-10% of the total charge in a bunch the rms emittance can be significantly improved. In this case a higher charge has to be launched at the gun. Therefore the laser will be designed to deliver photons for up to 1.5 nC. Longitudinal scraping could be performed in the first bunch compressor while transverse scraping

could be done in the drift space. However, it is not yet clear whether these halo particles would affect the performance of the FEL.

5.4 The Photocathode

The time structure of the bunch train of the TTF as well as the TTF FEL calls for photocathodes with quantum efficiencies higher than 1%. Such values are needed to keep the mean power of the laser below 2 Watts which is a reasonable number for a solid state laser. Very robust metallic photocathodes cannot be used because the maximum quantum efficiency achieved so far is less than 10^{-3}.

Semiconductor photocathodes offer a quantum efficiency higher than 1%. Caesium Antimonide cathodes can achieve a quantum efficiency up to 10% in the visible light spectrum. Unfortunately the life time of such photocathodes in the rf gun environment does not exceed several hours. Caesium Telluride (Cs_2Te) and Caesium Iodide (CsI) cathodes can survive operating inside an rf gun more than a month with a quantum efficiency greater than 2%. The photo-emission cut-off for Cs_2Te occurs at a longer wavelength (~260 nm) than in the case of CsI (~210 nm). The latter wavelength is impractical for operation. In contrast, a wavelength of 262 nm can be chosen as fourth harmonic of the Nd:YLF laser. For this reason we believe that Cs_2Te is the better choice despite the fact that CsI cathodes can withstand a short exposure to air. Other photocathode materials such as GaAs or Si have also been considered for rf gun applications. However it has not been demonstrated yet that such materials can have a response time compatible with the TTF FEL photo injector requirements and can work properly in the high field rf environment.

An additional advantage of semiconductor cathodes as compared to metallic cathodes is the possibility to reduce the thermal emittance of the photoemitted electrons.

In metallic cathodes the electrons lose energy due to electron-electron scattering. Thus in order to get a reasonable quantum efficiency the photon energy has to exceed the work function of the material by some amount. The difference between photon energy and work function contributes to the thermal emittance of the electrons. For the wavelength of 262 nm the normalized thermal emittance of electrons from a copper cathode can be estimated as:

$$\varepsilon_t^n \cong \sigma_t \cdot 1\,\pi\,\text{mrad}$$

where σ_t refers to the transverse spot size of the beam.

On the other hand electrons scatter elastically from phonons in semiconductors. Thus the quantum efficiency is already high in the vicinity of the photo emission cut-off.

The properties of a thin Cs_2Te layer can be affected by the material of the cathode holder as indicated by the difference of CERN results (copper holder) and LANL results (molybdenum holder). An investigation of this effect is on the way at INFN Milano. The measurement of the thermal emittance of a Cs_2Te cathode is underway.

The Cs_2Te cathode for the TTF and the TTF FEL will be deposited on a molybdenum holder. Several holders will be kept in a high vacuum container. The container will be an integral part of the photo injector therefore photocathodes can be replaced without

breaking the vacuum. The photocathodes will be produced at DESY. A transport chamber will carry the photocathode holders in a high vacuum environment from a preparation chamber to the photo injector. Such a system will minimize disturbances of the FEL operation due to exchange of photocathodes.

The development of the technology of the preparation and the transport chamber for the TTF and the TTF FEL will be done at INFN Milano. The work will be carried out in the frame of the TTF collaboration for the TTF Injector II.

After a test run at INFN the preparation and the transport chamber will be sent to Fermilab in 1996 for the Injector II tests and will then be installed at DESY for the TTF and TTF FEL operation.

5.5 The Laser System

The electron bunch structure to drive the FEL demands an unusually long macro pulse with high average power and extreme stability in amplitude and time. Especially the generation of the long train of up to 7200 short pulses, spaced by 0.11 μs at a repetition rate of 10 Hz, requires a sophisticated laser design. In general, the design of the laser must aim for long-term stable operation together with a high degree of reliability. Detailed specifications are listed in table 5.3. A laser which fulfils these specifications is not commercially available.

Researchers from the Max-Born-Institut, Berlin (MBI) have made a proposal for a laser system for the Tesla Test Facility (TTF) [7]. Since the specification for the TTF laser [8] is very close to the demands in the FEL case, only an upgrade is required to match the FEL specifications. The MBI has established a project group which will develop the laser system in cooperation with DESY. The laser system will initially be used for the Tesla Test Facility. This gives the opportunity of testing the system and to optimize it for the FEL application.

Before presenting the design of the laser system, the two most important items of the requirements on the laser system are discussed: the time structure of the micro pulses and the mean power requirement, which depends on the required energy per micro pulse and on the macro pulse structure.

In this section, it is assumed, that the photo injector uses a Cs_2Te-cathode which has to be illuminated by UV light ($\lambda \leq 275$ nm) in order to achieve a reasonable electron extraction efficiency.

5.5.1 Time Structure of Micro Pulse

The required time structure of the micro pulses has a considerable impact on the choice of the laser gain medium. Once chosen, the minimal achievable rise time is fixed by physical constraints.

Optimizations of the present photo injector design indicate a reasonable performance if the rise time of the laser pulse is in the order of 5 ps and if a flat-top temporal profile for the electron bunches is used. The width is not yet fully optimized, but will be in the range from 5 to 20 ps.
This motivates the use of a system based on Nd:YLF as the gain medium. Nd:YLF is a solid Yttrium Lithium Fluoride crystal doped with 1% Nd^{3+}-ions. A pulse width of 8 ps

at the fundamental wavelength of 1047 nm after amplification has already been achieved by commercially available lasers [9][10]. Frequency quadrupling is expected to further shorten the pulse by a factor of 2. A reduction to 3 ... 4 ps in the fundamental wavelength is probably possible. With a bandwidth of $\delta\nu$ = 300 GHz [11], the pulse width is limited with Nd:YLF to δt = 1 to 2 ps ($\delta\nu\,\delta t \geq \frac{1}{2}$).

Item	Specification
gain material pumping wavelength	Nd:YLF as far as possible with diodes 4th harmonic (262 nm)
pulse train	800 micro pulses spaced by 1 μs option: up to 7200 micro pulses spaced by 0.11 μs
repetition rate	10 Hz
micro pulse energy on cathode	0.75 μJ (4th harmonic)[1]
micro pulse rise time (10% ... 90%; at 4th harmonic) micro pulse length (FWHM; at 4th harmonic)	5 ps; option: down to 2 ps 5 ... 20 ps[2]; option: down to 2 ps
longitudinal micro pulse form flat-top homogeneity	flat-top, whenever possible ±10% peak-to-peak
transverse micro pulse form flat-top homogeneity on cathode	flat-top ±10% peak-to-peak[3]
energy stability – pulse to pulse – integrated over 100 μs phase stability – first micro pulse – drift until end of train	 ≤ ±5% peak-to-peak[4] ≤ ±1% peak-to-peak[4] ≤ 1 ps rms ≤ 1 ps rms
beam dimension at cathode pointing stability	12 mm (flat-top diameter)[5] 5 μrad or equivalent 5% of rms spot size on the cathode[3]
synchronization	to reference signals from the Master Oscillator: 9.027775 MHz and higher harmonics
total power consumption	< 5 kW

[1] This energy corresponds to 20 μJ per micro pulse at the fundamental wavelength (reasonable loss factors assumed, including a safety factor of 4).
[2] The final pulse length has still to be optimized. However, it will be in the range given.
[3] This should be achieved using the relay imaging technique and overfilling the cathode.
[4] 10% peak-to-peak means that 90% of 1000 measured value are within ±10% of the nominal value.
[5] To optimize the performance of the gun, the beam radius should be adjustable.

Table 5.3: Specifications for the laser system

5.5.2 Estimation of required laser power

The required laser power in the infrared region depends strongly on the choice of the photocathode material, on the losses due to feedbacks, spatial filtering and harmonic generation, and on losses on the optical elements due to scattering and absorption.

Table 5.4 summarizes a conservative estimate of the losses from various sources. In order to produce an electron beam of 1.5 nC in the gun, a laser energy of $E_0 = 7.4$ nJ for a photon wavelength of 262 nm, and an ideal cathode efficiency of 100% is required. The required laser energy E_{IR} per micro pulse in the infrared is then simply given by $E_{IR} = 7.4\ nJ/\eta$ with η being the overall efficiency. To calculate the overall mean laser power, the full train of 7200 micro pulses with a repetition rate of 10 Hz is assumed. The estimation yields a reasonable mean laser beam power of 0.34 W.

The critical points are clearly the harmonic generation and cathode efficiencies. A safety factor of 4 has to be included to cope with the associated uncertainties. The electron extraction efficiency of the cathode is defined as the number of electrons measured at the gun exit divided by the number of photons illuminating the cathode. Efficiencies obtained so far with a Cs_2Te-cathode at CERN and LANL range from 1% to 3% and were stable over several weeks.

The efficiency of generating the fourth harmonic at 262 nm from the fundamental laser line at 1047 nm depends on the non-linear material chosen and in addition on the square of the laser pulse power, the beam diameter, and on the transverse and longitudinal beam shapes. For gaussian shaped beams an efficiency of 10% is obtained. Transverse flat-top beams may reach up to 30%.

Item	Efficiency	
9 mirrors	0.8	reflectivity = 98%
2 splitters for monitoring	0.98	
3 lenses	0.88	loss = 2% per lens surface
vacuum window	0.9	
feedback Pockels cell	0.7	
spatial filter	0.9	
harmonic generation	0.2	
cathode	0.02	
overall efficiency η	$1.6\ 10^{-3}$	
$\rightarrow E_{IR} = 7.4\ nJ/\eta$	4.6 μJ	per micro pulse
$\rightarrow$ mean power P	0.34 W	7200 micro pulses at 10 Hz
$\rightarrow$ total mean power P_{tot}	1.2 W	including a safety factor of 4

Table 5.4: Estimated efficiencies of optical elements, harmonic generation and cathode from the infrared output of the laser to the cathode.

5.5.3 Choice of gain medium

The advantage of Nd:YLF compared to other materials, that are suitable for producing short pulses in the sub-picosecond range, is its high induced-emission cross-section and its long fluorescence lifetime of 480 μs. Both are well suited to produce a long pulse train of high average power. The thermal load of the Nd:YLF rod can be significantly reduced by pumping it with semiconductor diode arrays. Their wavelength can be tuned

to be optimally absorbed by the pump levels of the Nd^{3+}-ions and be transferred to inversion with almost no losses.

The fundamental wavelength of Nd:YLF is 1047 nm. Frequency quadrupling to 262 nm is necessary to produce an output in the UV.

5.5.4 Basic Laser Design

In general, the design of the laser system concentrates on stability and reliability. A high degree of automatization is aimed for. A computer based control and monitoring system will be an integral part of the laser. Several feedback stabilization systems and phase-locked loops are incorporated to assure a highly effective stabilization in energy and phase. A schematic drawing of the laser is shown in figure 5.4.

The pulse train is generated by a so called injection-locked pulse-train oscillator (ILPTO). The round-trip time in the oscillator is a harmonic of the required micro pulse spacing of 1 μs.

A seed pulse from an external master oscillator is injected into the ILPTO. The seed pulse is produced from a commercially available diode-pumped mode-locked Nd:YLF laser running at 217 or 108 MHz. The seed pulse length is typically 8 ps (FWHM) at 1047 nm and has an energy of about 0.5 nJ. The seed pulse is synchronized with the rf. It will have a timing module incorporating a phase-locked loop to synchronize the laser with an external reference signal. Experience at CERN with such a laser is promising and shows a phase jitter of less than 1 ps rms.

The seed pulse will be trapped in the ILPTO by switching a Pockels cell. One cavity mirror is partially transparent allowing the formation of the pulse train. While the seed pulse oscillates in the cavity, a diode-pumped Nd:YLF rod first amplifies the pulse to the required energy. The pumping continues to form the train. In this phase, only the losses due to the train formation and normal resonator losses are compensated for. To achieve this special pumping scheme, the pump diode lasers will be driven by a computer controlled pulse-forming system.

The low-signal gain of the amplification process is kept low in order to conserve as much as possible full bandwidth and thus to keep the pulses short.

Diode pumping is chosen to obtain excellent stability and high reliability. Flash lamps have the disadvantage of high pulse-to-pulse fluctuations in the pumping power and short lifetimes. Due to the high pumping efficiency, diode pumping significantly reduces the heat load in the Nd:YLF rod.

Acousto-optical modulators preserve the pulse length of 8 ps during the several thousand round-trips required to form the train.

A critical point is the stabilization of the resonator length, which directly determines the pulse-to-pulse spacing. This will be done with a piezo-driven mirror incorporated in a phase-locked loop. The correction rate will be up to the kHz level. The stabilization method will be very similar to the timing stabilization in the external oscillator. As mentioned above, a phase jitter of less than 1 ps is achievable.

However, kHz correction will not allow stabilization within the pulse train, where the correction rate must exceed 1 MHz. Phase errors from micro pulse to micro pulse would occur, if the ILPTO were subject to external vibration, mechanical or acoustic noise during the train evolution.

To prevent this, a feedback method is going to be developed, which works at 1 MHz or above. For this purpose, a crystal is placed inside the ILPTO which allows the modulation of its refractive index and thus a fine tuning of the effective resonator length.

The bunch spacing of the train generated by the ILPTO will be a multiple of 1 MHz (36 MHz is considered). Otherwise, the resonator would be simply too long. Before the amplification stages, a pulse picker running at 1 MHz will pick out every 36^{th} pulse to form the train structure of 800 micro pulses spaced by 1 μs. The pulse picker consists of a Pockels cell in combination with a polarizer.

In the case of 7200 micro pulses per train, two pulse pickers would be combined to pick out every 2^{nd} pulse each. Due to the high picking rate of 18 MHz for the first and 9 MHz for the second pulse picker, the Pockels cells will be driven by a sinusoidally modulated voltage in a resonance circuit.

The micro pulse energy after the pulse picker will be between 1 and 3 μJ. Two or three Nd:YLF single pass amplification stages are foreseen to amplify the pulses to the required energy of 20 μJ per micro pulse.

The first amplifier as well as the ILPTO will be diode-pumped. For stability reasons, it is preferred to pump the last two amplifiers with diodes as well. However, the pumping power required would result in considerable costs for the laser diodes. Flash lamps would easily provide the power at reasonable cost. A careful study on the comparison of both methods has been started. As a first step, a simulation program to optimize the geometrical arrangement of the pump diode arrays has been developed.

The laser system uses the relay imaging technique in combination with spatial filtering to produce a homogeneous flat spatial intensity distribution (a flat-top profile) on the photocathode surface.

Two non-linear crystals, KD*P and BBO, will provide the 2^{nd} and 4^{th} harmonic (262 nm). A pulse stretcher is foreseen, if longitudinal flat-top pulses longer than 5 ps are required. The pulse stretcher will be based on the method of splitting and delayed overlaying of the pulses.

There will be a feedback loop to stabilize the pulse energy. The energy of each micro pulse is monitored after harmonic generation at 262 nm, and is used to correct the amplification inside the ILPTO directly. Since the ILPTO generates more pulses in the train than are actually used, these pulses serve for the regulation process. With this scheme, regulation oscillations in the train itself will be avoided.

5.5.5 Controls and Monitoring

The laser system will include all necessary controls and monitoring, as well as an interlock system for safe operation.

Beam shape and pointing stability will be measured using CCD cameras. The spatial beam shape will be analyzed at different locations and appropriate corrective action will be taken automatically. For this, critical mirrors will be equipped with stepping motors to suppress long term drifts in pulse shape and position.

The laser pulse length is measured by second-order auto-correlation. This is a standard technique and appropriate auto-correlators are commercially available.

The mean energy is measured by a joule-meter integrating over a part of the train. The energy variation from micro pulse to micro pulse is monitored by fast photo-diodes. The

signals can be displayed on an oscilloscope and are in addition digitized for further analysis.

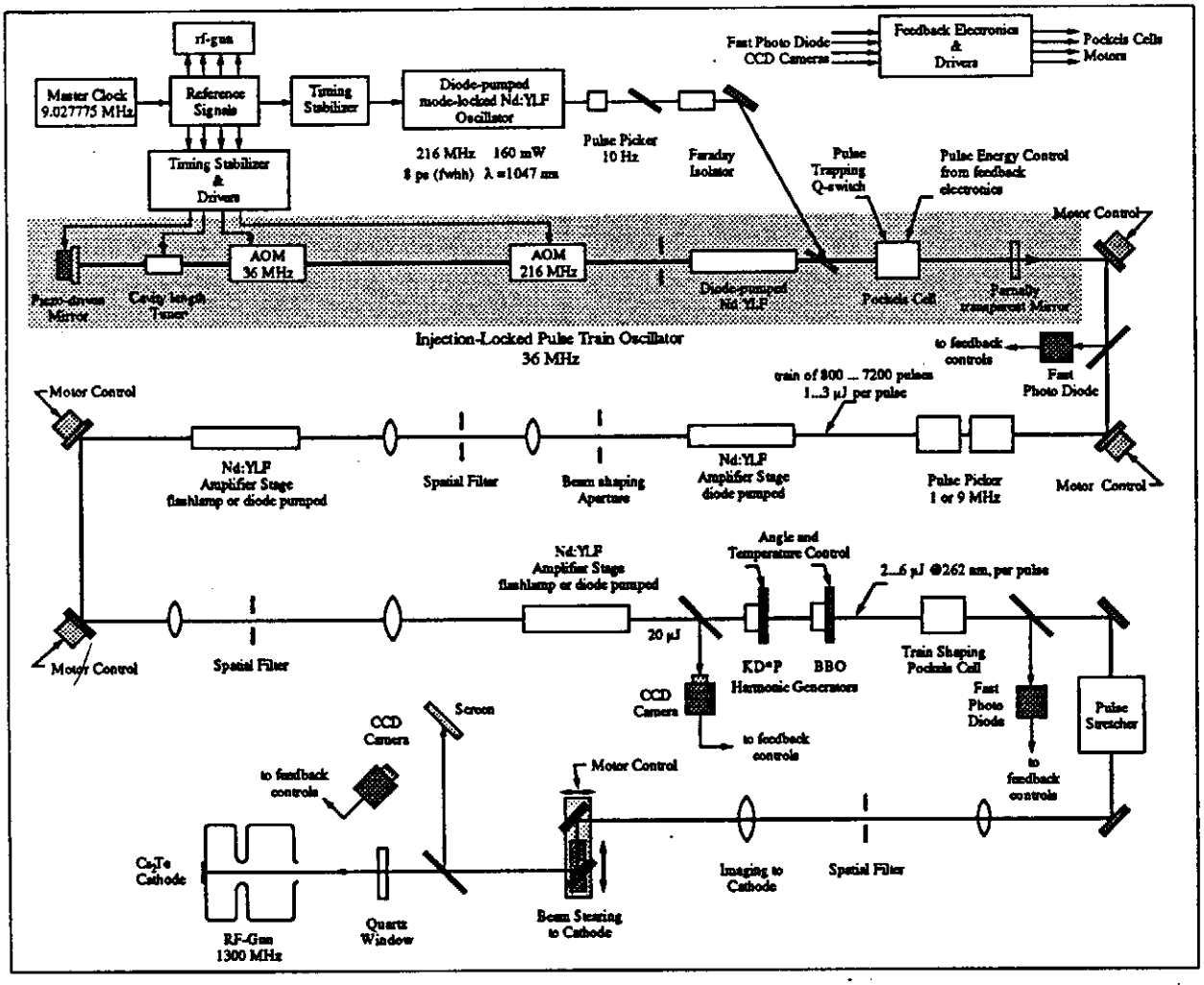

Figure 5.4: Schematic layout of the proposed TTF/FEL Photo Injector Laser System.

References

1 J.Fraser, R. Sheffield, Nucl. Instr. Meth. **A250**, (1986)71.

2 B. E. Carlsten, *New Photoelectric Injector Design For The Los Alamos National Laboratory XUV FEL Accelerator* , Nucl. Instr. Meth. **A285**, (1989) 313.

3 I. Lehrman, et al, *The Gruman/Brookhaven High-Brightness, High-Duty Factor RF Gun* , Linear Accelerator Conference, Ottawa, 1992

4 D. T. Palmer, et al, *Microwave Measurements of the BNI/SLAC/UCLA 1.6 Cell Photocathode RF Gun* , Particle Accelerator Conference, Dallas, 1995

5 K. T. McDonald, *Design of the Laser-Driven RF Electron Gun for the BNL Accelerator Test Facility* , DOE/ER/3072-43, 1988

6 H. Matsumoto, et. al, *High Gradient Experiment by ATF,* KEK Preprint 91-161, 1991

7 I. Will, P. Nickles, W. Sandner, *A Laser System for the TESLA Photo-Injector* , Internal Design Study, Max Born Institut, Berlin, October 1994

8 Tesla-Collaboration, ed. D. A. Edwards, *Tesla Test Facility Linac-Design Report* , DESY Print March 1995, TESLA 95-01

9 Lightwave Electronics Corporation, Series 130, Users Manual 1991, *Introduction to Diode-Pumped Solid-State Lasers* , Technical information by Lightwave Electronics Corp. (1993), pp.14, and references therein

10 S. Schreiber, *The Synchro Laser System for the CLIC Test Facility,* Proc. of the Workshop 'Lasers for Rf-Guns', Anaheim, CA, USA, May 1994, and CERN AT/94-32 (DI)

11 D. W. Hughes, J. R. M. Barr, Appl. Phys **25**, (1992), 563.

6. The Bunch Compression System

6.1 Introduction

Space charge effects prevent electron guns from producing bunches considerably shorter than 1mm while maintaining the brightness necessary for a SASE-FEL. A bunch compression system is needed to compress the bunch down to its final length of less than 100 mm, thus providing the necessary high peak intensities at the undulator.

Figure 6.1 shows the principle of bunch compression in longitudinal phase space. The uncorrelated energy spread of the beam leaving the gun is around 25 keV, its length 2 mm. The SASE process requires less than 1000 keV energy spread at the undulator. The initial longitudinal emittance of around 50 mm·keV is already close to the finally tolerable emittance, so emittance blow up during compression has to be kept small.

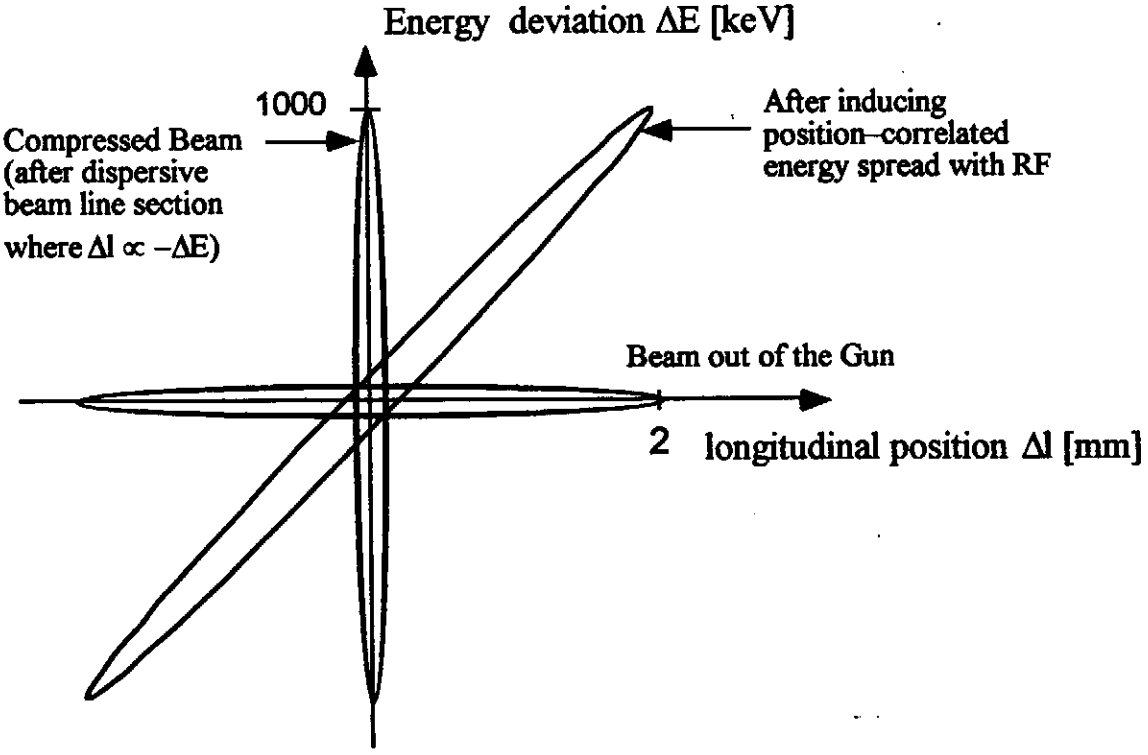

Fig.6.1: Principle Scheme of Required Bunch Compression

In an ideal bunch compressor, a linear correlation between energy and longitudinal position is induced in the bunch, for instance by passing a high gradient RF structure at the zero-crossing phase. Then follows a sequence of bending magnets where particles with different energies have different path lengths; mostly because they travel on circles with different radii through the bending magnets with dispersion. The dependence between path length and particle energy is therefore, to very good approximation, linear and with the right choice of parameters an ideal full compression as shown in Fig. 1 can be achieved. The final bunch length is basically determined by the ratio of initial to induced energy spread.

Compressing the bunch in the TTF-FEL will be done in stages to negotiate two effects limiting the achievable bunch length: On the one hand, a long bunch traveling through the whole linac accumulates too much non-linear, although correlated, energy spread from the cosine-like accelerating RF field. We looked into compressors with non-linear dependence between path length and energy spread to compensate for that, but found that introducing these non-linearities gives rise to other non-linear terms like higher order dispersion which then dilute the emittance.

On the other hand, space charge effects scale with $1/\gamma^2$ and prevent bunch compression resulting in very short bunches if the energy is still too low. Also, longitudinal wake field effects get stronger if the bunches are shorter. The following chapter describes the resulting layout of the bunch compression system in the TTF-FEL.

6.2 Layout of the TTF-FEL Bunch Compression System

As shown in Figure 6.2, the bunch compression will be done in three stages. The first compressor might be considered part of the electron injector since it is located directly after the first 15 MeV acceleration section and compresses a 2 mm bunch down to 0.8 mm.

In the next step, after the first RF module, the bunch is further compressed to 0.25 mm at an energy of 144 MeV and the third step reaches the final value of 0.05 mm.

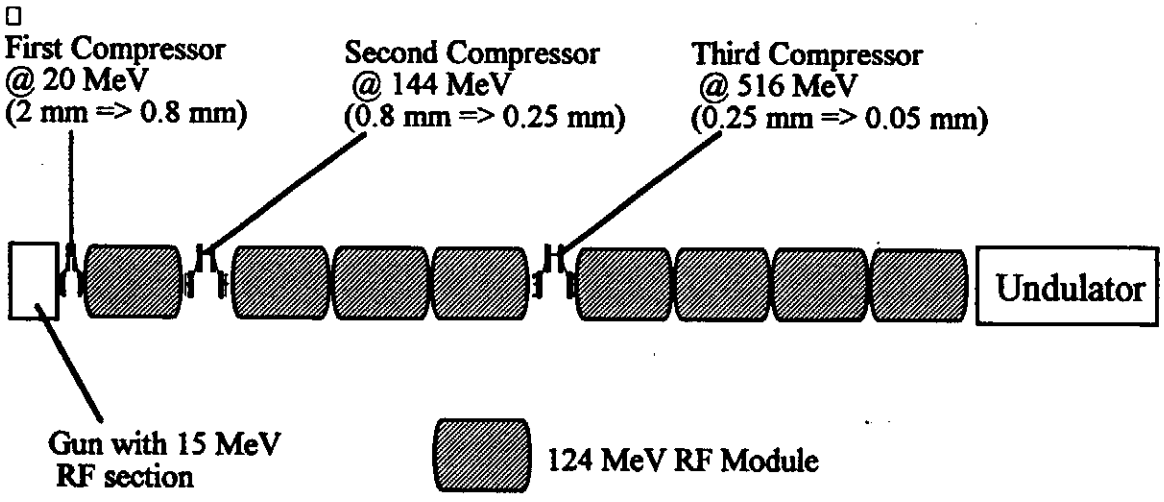

Fig. 6.2: Layout of the TTF-FEL Bunch Compression System

The bunch compressors two and three are shown in Fig. 6.3. The stage 1 compressor looks essentially the same but for being half as long. The bending magnets are rectangular magnets which do not have net focusing in the horizontal plane and therefore do not generate higher order dispersion that would increase transverse emittance. They do focus the beam vertically, the focal length being inversely proportional to the tangent

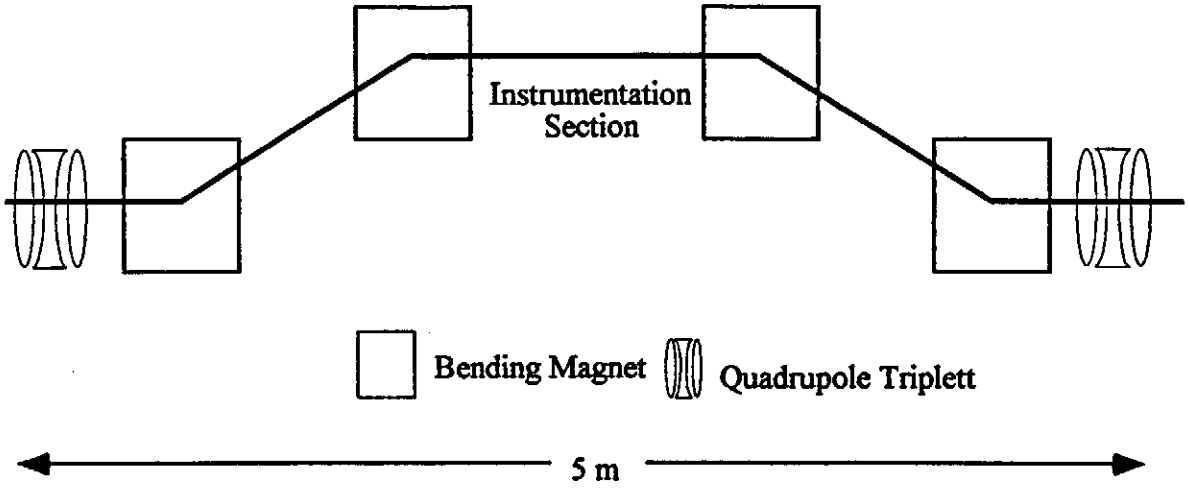

Fig. 6.3 : Layout of the Bunch Compressors at Stage 2 and 3

of the entrance angle of the beam. For bending (and entrance) angles of more than 30 degrees, additional quadrupoles have to be considered between the bending magnets to avoid too densely focused beams in the vertical plane, which would cause emittance growth due to space charge effects. For the proposed bunch compression system

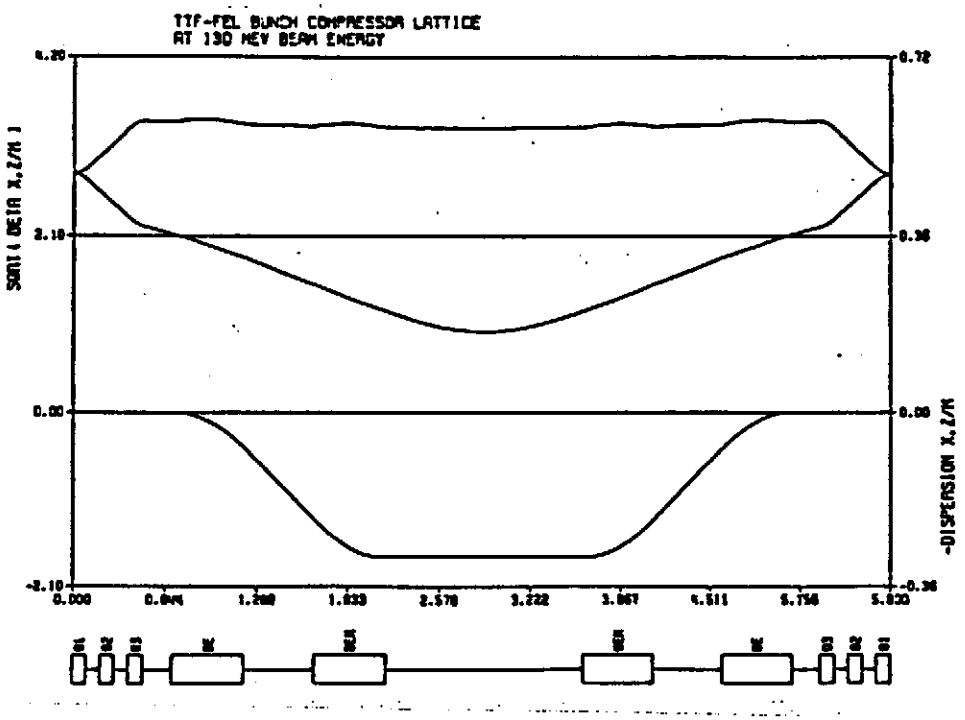

Fig. 6.4: Optical Parameters in the Compressor Section

however, deflection angles of up to 25 degrees are sufficient. The quadrupole triplet strengths are chosen to match the incoming optics parameters to the outgoing, to make the compressor section transparent and to keep it symmetric around the mid-plane. Fig. 6.4 shows the horizontal and vertical beam sizes (normalized with respect to transverse emittance) and the dispersion function across the compressor section.

In Figure 6.5, the maximum horizontal dispersion and the resulting 'longitudinal dispersion' R56 are shown. The path length difference Δl of an off-energy particle is given by

$$\Delta l = -R56 \times \Delta E.$$

The choice of the necessary tuning range for the longitudinal dispersion determines the width of bending magnet gaps and vacuum chamber. For a very comfortable R56 tuning range of 0.1–0.3, the aperture in the middle bends and the instrumentation section must be 170 mm for the difference in beam orbit plus twice the dispersion dominated beam size of 20 mm (4 sigma of a beam with 1% energy spread at 0.5 m dispersion) which is 210 mm. The final choice of apertures will depend on magnet cost estimates.

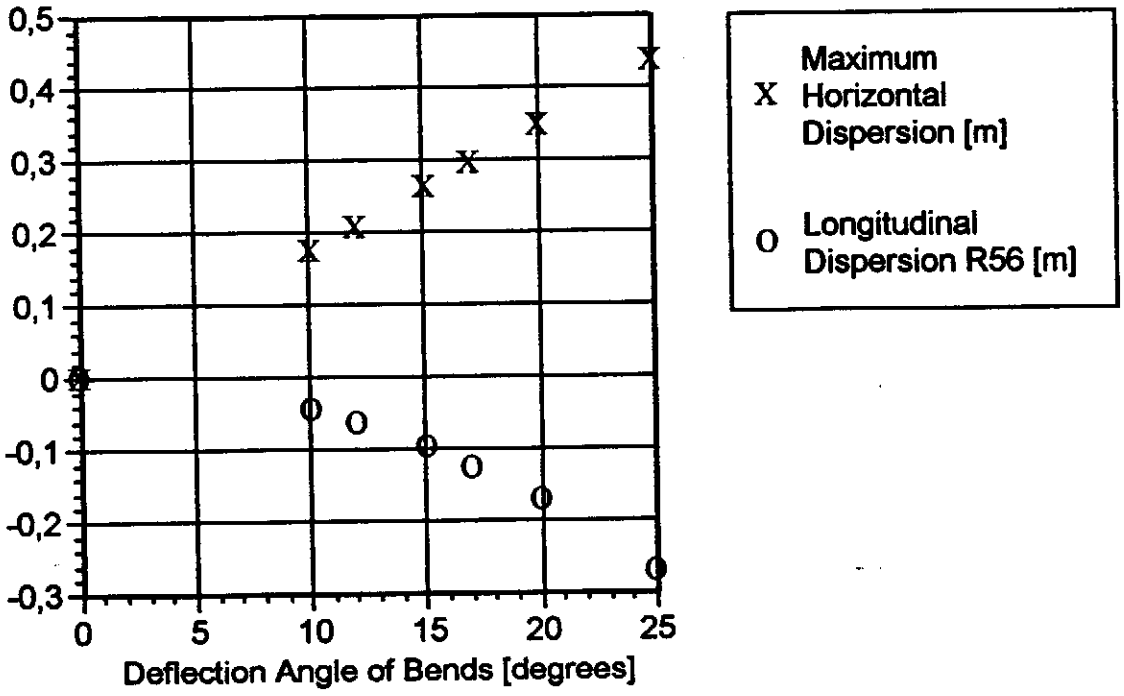

Fig. 6.5: Maximum Horizontal Dispersion and Longitudinal Dispersion R56 vs. Bending Magnet Deflection Angle of the Bunch Compressors two and three.

6.3 Computer Simulations

Bunch compression has been simulated in two different ways. A one-dimensional model including the nonlinear RF and longitudinal wake fields was used to do a first optimization of RF phases and the longitudinal dispersion R56 of the compressor sections. To study space charge effects and subsequently re-optimize the compression scheme, three-dimensional calculations using the code PARMELA were carried out.

Calculations with a One-Dimensional Model:

In the one-dimensional model, it was assumed that the bunch leaves the injector with 0.8 mm bunch length and a random energy spread of 25 keV. Figure 6.6 shows the bunch in longitudinal phase space before and after compression stage 2 at a beam energy of 145 MeV. Note that the bunch is not fully compressed to avoid problems with space charge effects.

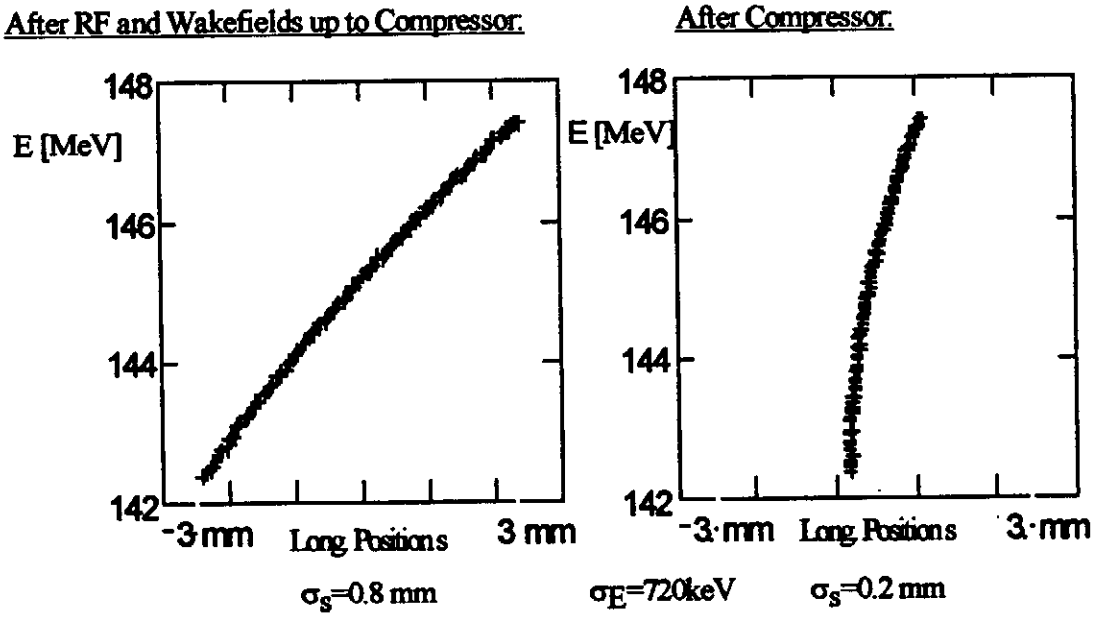

Fig. 6.6 : Longitudinal Phase Space before and after Bunch Compressor #2

The bunch then passes through three RF modules, where it experiences the non-linear shape of the RF pulse as well as longitudinal wake fields. The phase of the bunch has to be optimized to achieve the best cancellation of both effects. Figure 6.7 shows the result of such an optimization: the bunch entering the final compression stage 3 has a nearly linear correlation between energy and longitudinal position over a wide range and can therefore be compressed down to 54 μm.

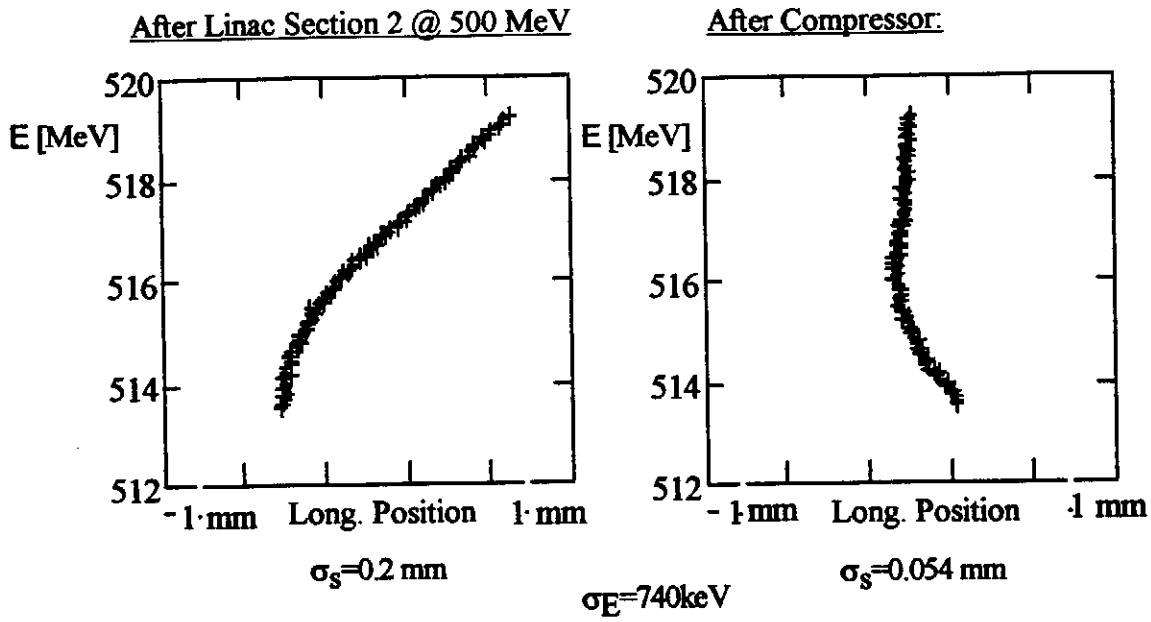

Fig. 6.7 : Longitudinal Phase Space before and after Bunch Compressor #3

In the last part of the linac, where the bunch is accelerated to 1 GeV, its longitudinal distribution does not change anymore. Its energy spread, however, will be increased by RF non-linearities and wake fields. Here again the RF phase has to be adjusted to minimize growth in energy spread. The bunch gains another 130 keV of energy spread on its way to the undulator, see figure 6.8.

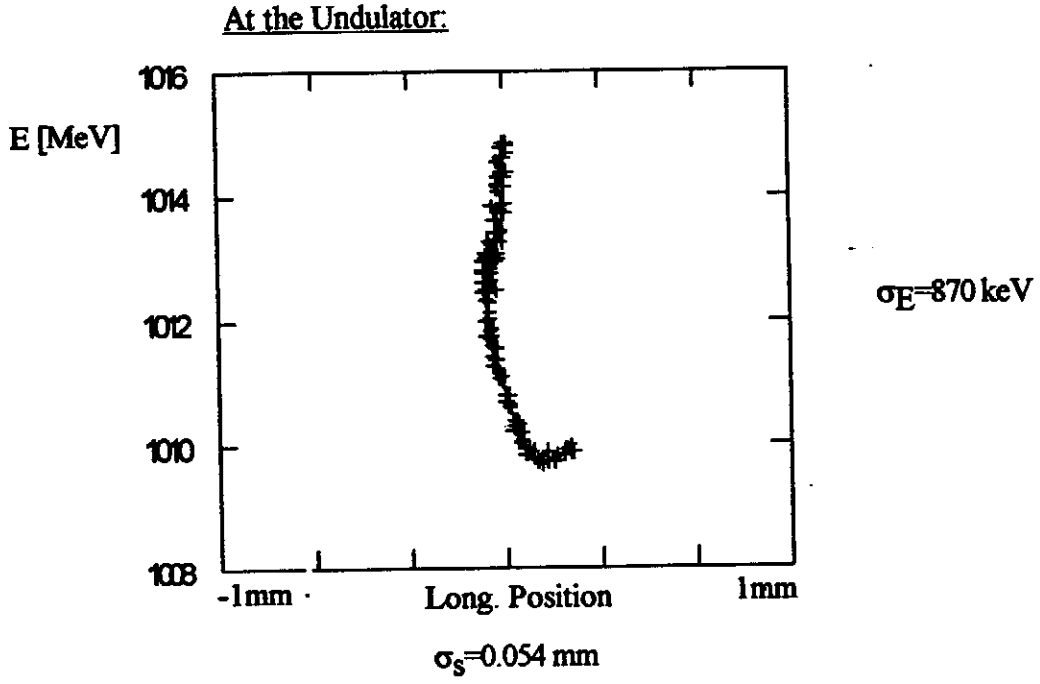

Fig. 6.8: Longitudinal Phase Space at theEntrance oj the Undulator

3-Dimensional Calculations with PARMELA:

The computer code PARMELA was used with a point-to-point algorithm to calculate space charge effects, since inside the compression sections the beam is not cylindrically symmetric. For these calculations all three bunch compressors were modeled with their optical elements. Figure 6.9 shows a PARMELA run without space charge. The RMS-value for bunch length is 0.075 mm but is dominated by the tails of the distribution. More than 70% of the charge is within a window of ±0.05 mm, supplying the necessary peak current.

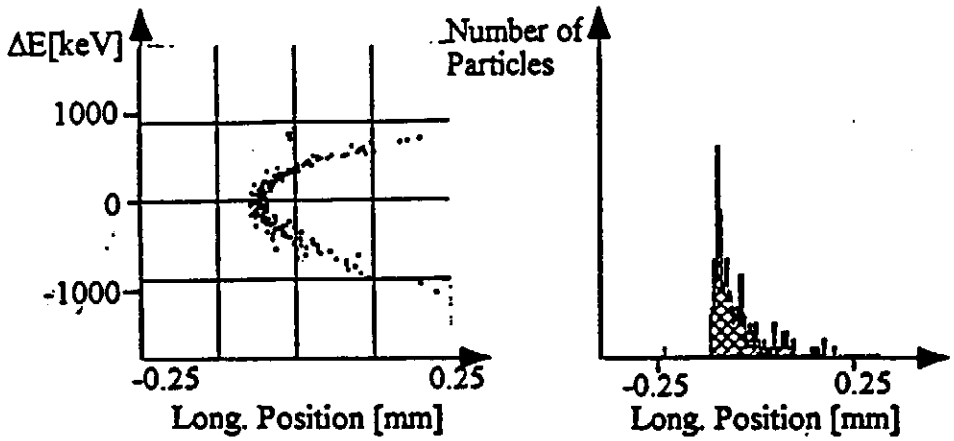

Fig. 6.9 Longitudinal Phase Space and Longitudinal Bunch Distribution after Bunch Compressor #3 without Space Charge Effects

If space charge effects are included (Figure 6.10), the distribution broadens, the RMS-value is nearly unchanged, but the charge contained within ±0.05 mm drops to about 60% , which is still within specifications.

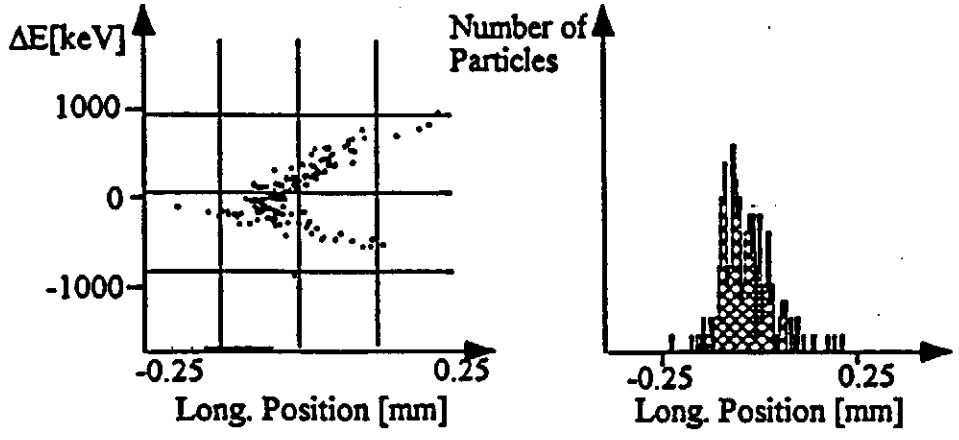

Fig. 6.10 Longitudinal Phase Space and Longitudinal Bunch Distribution after Bunch Compressors #3 with Space Charge Effects (bunch charge ≈1 nC)

The energy spread in both calculations is of the order of 500 keV, but wake fields are not yet included in these calculations, so it is expected to be closer to 1 MeV at the undulator as in the one-dimensional calculations.

7 Accelerator

This chapter gives a short overall description of the TESLA Test Facility Linac (TTFL) design. Therefore it can be used as a basis for discussing the extension of the TTFL to higher energies as they are needed for driving the above described Free-Electron Laser. Since the complete TTFL design is given in the Conceptual Design Report (CDR)[1] in detail, here the main emphasis is placed on the description of the necessary modifications of the linac.

7.1 The 500 MeV TTF-Linac

The TESLA Test Facility is located in Building 28 (Halle 3) at DESY; a plan view of the layout is shown in Fig. 7.1. The linac itself is within a shielded enclosure in the upper part of the figure. The operating parameters are given in Tab. 7.1 where the two columns Inj I / Inj II already list the scenarios for two different injectors to be described below.

[1] *TESLA Test Facility - Conceptual Design Report*, TESLA Report 95-1, DESY 1995

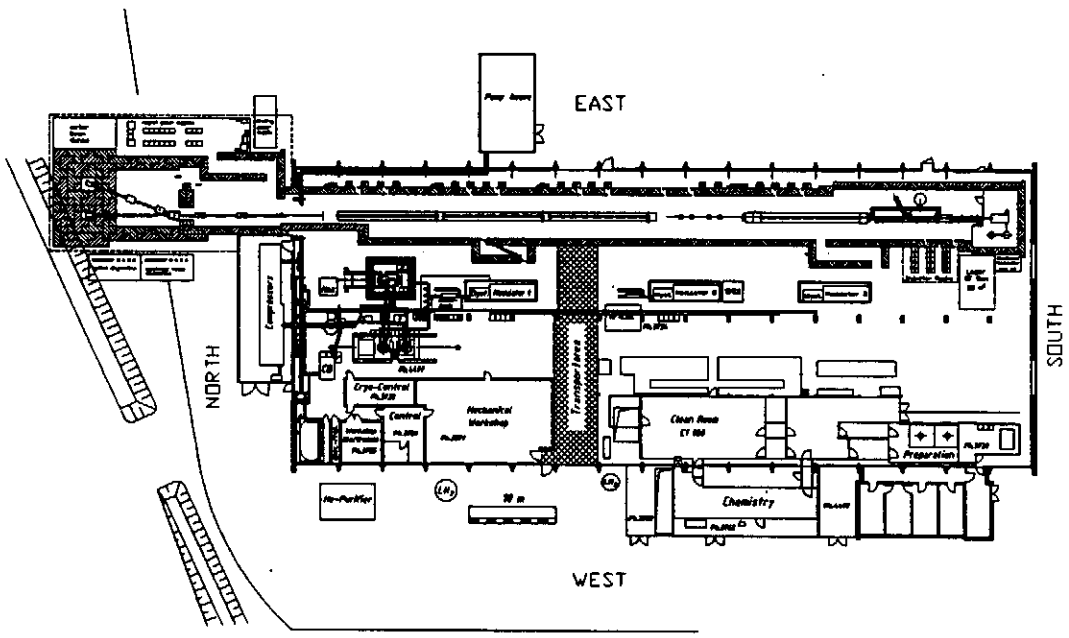

Figure 7.1: Layout of the TESLA Test Facility

Table 7.1: TTFL operating parameters.

Parameter	TTFL	
Linac Energy	500 MeV	
RF frequency	1.3 GHz	
Accel Gradient	15 MV/m	
Q_0	3×10^9	
# Cryo modules	4	
Energy spread, single bunch rms	$\approx 10^{-3}$	
Energy variation, bunch to bunch rms	$\approx 2 \times 10^{-3}$	
Bunch length rms	1 mm	
Beam current	8 mA	
Beam macro pulse length	0.8 ms	
Lattice β typical	12 m max	
	Inj I	Inj II
Injection Energy	10 MeV	20 MeV
Normalized Emittances (x/y), $\gamma\sigma^2/\beta$	$\approx 5\mu$m	$\approx 20\mu$m
Beam size σ, end of linac	250μm	500μm
Beam size σ, injection	1.7 mm	2.5 mm
Bunch frequency	217 MHz	1MHz
Bunch separation	4.6 ns	1μsec
Particles per bunch	2.3×10^8	5×10^{10}

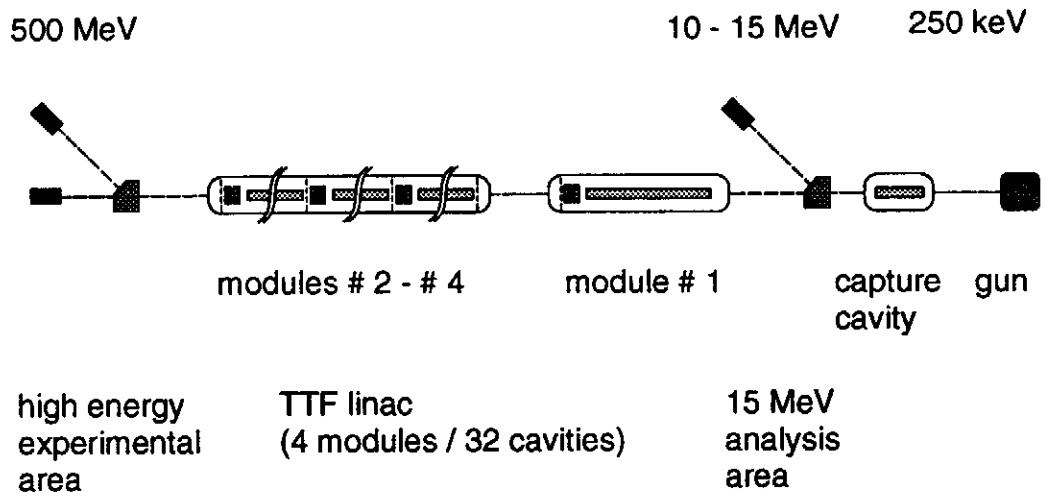

Figure 7.2: Schematic Layout of the TTF-Linac

An expanded view of the linac is shown in Fig. 7.2. The TTFL contains three major regions: the injector area, the main body of the linac, and the high energy beam analysis area. In the first stage of installation the injector area includes a thermionic electron gun, a subharmonic prebuncher, the superconducting capture cavity, focusing lenses, and beam diagnostic equipment. The capture cavity is identical to one of the nine-cell structures (see Tab. 7.2 below) in the main linac. The principal parameters of this injector (Injector I) are given in the CDR, together with a detailed technical description. The main difference to the final injector is a reduced bunch charge as well as bunch spacing, which will aim for an average beam current of 8 mA during the rf pulse. In the future, Injector I will be replaced by a high bunch charge injector (Injector II) based on a laser driven rf electron gun similar to the one which has already been described in one of the preceding chapters. This Injector II comes close to the requirements of the TESLA Linear Collider electron source. The new installation will be located in the same injector area but needs some additional space for the laser and for the klystron / modulator driving the rf electron gun.

The time structure of the Injector II electron beam will be as shown in Fig. 7.3. 800 bunches, 1 μs apart, forms a macro pulse which then will be repeated every 100 ms. For the accelerator operation the number of bunches is not fixed. Reduced bunch charge and spacing are the main differences to the final injector, which will aim for an average beam current of 8 mA during the rf pulse. The transverse emittance for Injector II, as given in Tab. 7.1, clearly does not meet the requirements for the FEL electron beam; the main difference to the FEL electron gun is described in section 5.

Four cryomodules, each 12.2 m in length, comprise the main body of the linac. Each cryomodule contains eight nine-cell π-mode cavities and a "quadrupole package". Depending on the finally achieved accelerating gradient (15 - 25 MV/m) the energy gain per cryomodule will be between 120 and 200 MeV. Each cavity has an input coupler for rf power, two higher-order-mode (HOM) output couplers, and

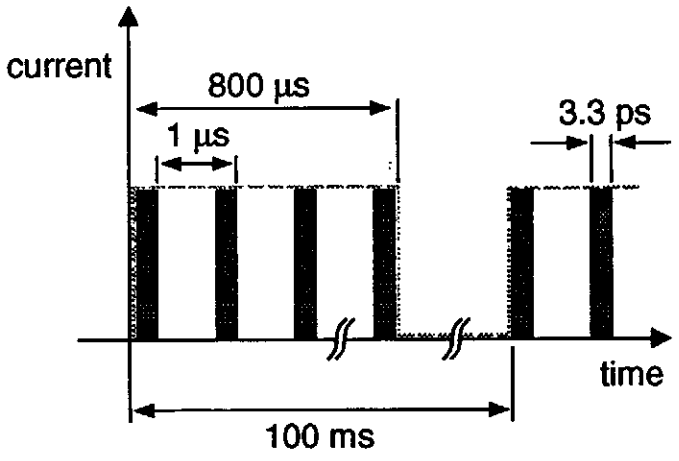

$E = 500 - 800$ MeV
$\bar{I}_{mp} = 64$ µA
$\bar{I} = 8$ mA
$n_{e^-} = 5 \times 10^{10}$ per bunch

Figure 7.3: Time Structure of the TESLA Test Facility Electron Beam

a tuning mechanism. Selected parameters of the cavities are given in Table 7.2. The quadrupole package includes a quadrupole doublet, transverse steering coils, a transverse beam position monitor and an HOM absorber.

Rf power for the main body of the linac will be provided by two klystrons and two modulators. Each klystron/modulator will deliver 4.5 MW with a pulse length of up to 2 ms. The cavities will operate at a temperature of 1.8 K, with refrigeration provided by a system of 100 W capacity at 1.8 K, which will be increased to 200 W capacity by the addition of a heat exchanger. A summary of the cryogenic system budget will be discussed below. Here it is worth mentioning that the 25 MV/m gradient already needs the 200 W capacity.

A summary schedule for the TTFL is shown in Tab. 7.3. Listed are all items of importance for the FEL plans.

Table 7.2: RF cavity parameters for the TTFL

Frequency	1.3	GHz
Cells per cavity	9	
Cavity length	1.036	m
Iris radius	35	mm
R/Q	1011	ohms/cavity
E_{peak}/E_{acc}	≈ 2.0	
RF power @ 25 MV/m	206	kW/m
HOM k_{long}/cavity	8.5	V/pC (1mm bunch σ)
HOM k_{trans}/cavity	18	V/pC/m

Table 7.3: Summary schedule for TTFL as of April 1995.

Item	Condition	Expected Date
1st cryomodule	start assembly	8.95
1st cryomodule	assembly complete	11.95
Feed can	delivery	7.95
1st cryomodule	cold test	11.95
Injector I	start test Saclay	3.95
Injector I	start oper DESY	10.95
Beam test 1st cryomodule	start	12.95
Final cavity order	release	
Final cryomodule order	release	
Assembly modules 2-4	start	5.96
Modules 2-4	install in linac	3.97
Beam tests, 4 modules	start	4.97
Injector II	start DESY operation	3.97
Beam, linac & Inj II	start	5.97

7.2 The TTF-Linac as a FEL Driver

The use of the TTFL as a driver for the SASE Free-Electron Laser requires modifications as well as an extension of the present design. The extension leads to electron beam energies above 1 GeV. In order to avoid too big changes, the actual design on which the construction is based already shows some differences compared to the originally proposed layout [2].

The most obvious difference is the change of the beam direction. The DESY site only allows an extension of the linac north of hall 3. Therefore the TTFL injector will be set up as close as possible to the south wall of hall 3. In addition to this the total space for the injector area has been increased, this is in order to allow for a bunch compressor at injection energy (approx. 15-20 MeV). Space for a second bunch compressor has been reserved between the first and second cryomodule. Here the beam energy is above 135 MeV. The distance between the two modules is exactly the length of such an 8 cavity module. Both bunch compressors have been described in chapter 6.

Due to the increase of length by the bunch compressor, the high energy experimental area which is needed for high quality beam analysis will be set up in an annex north of hall 3. This annex building will consist of a number of shielding concrete blocks, covered by a "rain coat". Thus, the operating conditions inside the shielding are equivalent to those in the hall which is doubtless necessary for the high quality diagnostic stations. The experimental area including the beam dumps will be set up in a way which later on allows for moving it further downstream easily. It is foreseen to add a third bunch compressor to the TTF Linac, now at energies above 500 MeV. This compressor shortens the bunch length down to the FEL requirements of $\sigma_z = 50$ μm. The compressor is then followed by another four standard cryomodules, i.e. 32 additional superconducting cavities. At an accelerating gradient of 15 MV/m this allows for the energy of 1 GeV; a gradient of 25 MV/m would result in a maximum energy of 1.6 GeV. The necessary changes in the shielding are possible; a first idea for the section between the two linac bodies is shown in Fig. 7.4.

The beam dump in the straight section of the experimental area has been removed and the shielding is modified. The second beam dump, located in the dispersive section of the former high energy experimental area, might have to remain behind some shielding until the activation level decays to a reasonable value. The wall thickness in the area behind the fourth cryomodule is 1.6 m, the distance between the fourth and fifth module is again 12.2 m including the cold/warm and warm/cold transition. The remaining length is approximately 6 m and will take up the bunch compressor with its necessary beam diagnostics. The corresponding power supplies can be placed in the area east of the shielding. Downstream of the bunch compressor region the cryomodules #5 and #6 are shown. The shielding can be continued as a longer tunnel which feeds into the undulator area. Parts of the former high energy experimental area will be placed behind this. The beam diagnostics as well as the beam dumps are described in chapter 9 below.

[2] *Proposal for a TESLA Test Facility*, TESLA Report 93-1, DESY 1992

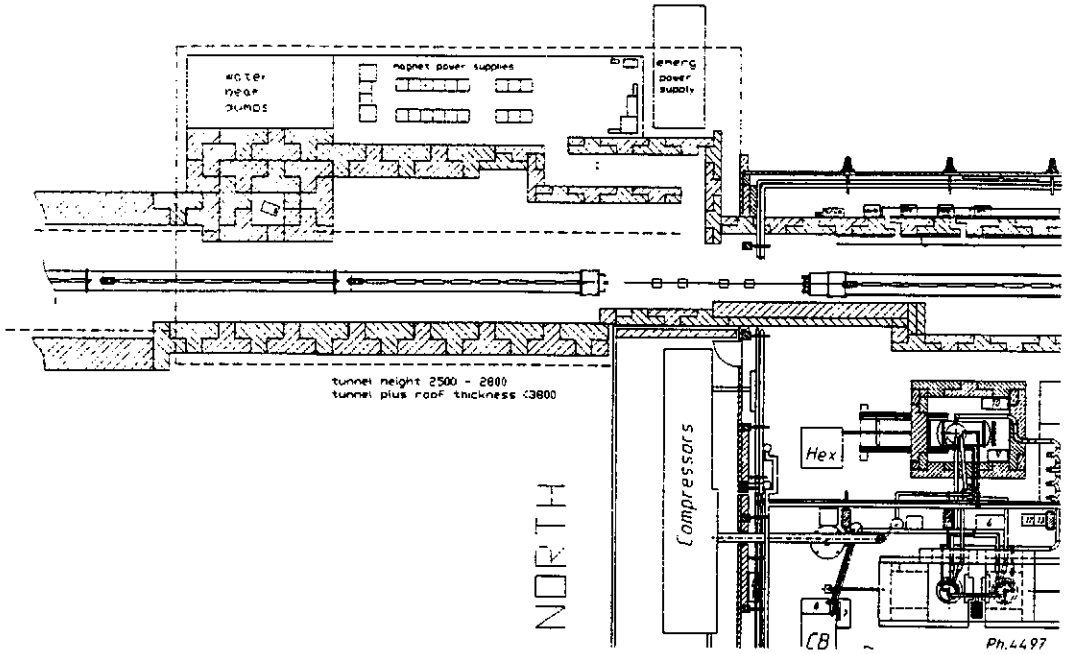

Figure 7.4: Draft of the Modified Experimental Area.

As the extended TTF Linac is twice as long, the cryosystem will have to be extended or even replaced. The operation has to be routine and independent of any test of further superconducting cavities, i.e. independent of the operation of the vertical and / or horizontal test cryostats in hall 3. Some preliminary consideration leads to two options. One is the replacement of the existing cryo plant, the other is the connection of at least the 4.5 K / 40–80 K supply to the HERA cryo plant. The first option would require a new 4.5 K coldbox which includes cold compressors and low temperature heat exchanger, a 2 MW screw compressor unit and a low pressure Helium purifier. The second option needs a long transfer line, feed boxes, the already mentioned coldbox, and cold compressors as well as warm pumping units. The costs for the two options are about the same. A summary of the requirements is given in Tab. 7.4.

Table 7.4: Cryogenic Load for the extended TTFL (1 GeV).

Heat Load Budget at 40 – 80 K	3	kW
Heat Load Budget at 4.5 K	800	W
Liquefying Rate at 4.5 K	5	g/s
Heat Load Budget at 1.8 K	400	W

The TTF Linac RF system has to supply the new modules in addition to the first 32 superconducting cavities. This has to be done according to the experience gained with the first modules. At the time of writing it is not clear if 32 cavities

can be supplied by one klystron or, even more difficult, can be controlled in one loop. This clearly has to do with the question of the maximum tolerable energy spread which is strongly coupled to the amplitude and phase jitter of single cavities. The amplitude and phase control has to be tried out before a detailed proposal for the cryomodules #5 - #8 can be made. The klystron might not be the problem since a 10 MW version, which is under development for the rf electron gun, will be available.

8 Beam dynamics in the TTF linac

The injector, based on a photocathode rf gun, is assumed to deliver a low emittance beam at an energy of about 20 MeV, with short bunches of rms length 1mm and charge 1nC. In order to achieve the necessary peak current and final energy of 1 GeV, the beam must be bunch-compressed and accelerated through the existing TTF linac, extended by four more accelerating modules. In addition to the peak current, small energy spreads and small transverse emittances are needed to satisfy the FEL requirements. The high phase space densities produced by the rf gun have to be preserved during the bunch compression and the acceleration in the long transport lines. The major sources of longitudinal and transverse dilutions are space charge forces, wakefields effects and dispersive errors. This section tackles more specifically the problems of longitudinal and transverse emittance dilution arising from dispersive and wakefield effects.

8.1 Longitudinal phase space

A two stage bunch compressor is used to decrease the rms bunch length from 1 mm to around 50 μm and produce a peak current of 2-3 kA. The first compression in the TTF linac is performed at 120 MV, after the first 8-cavity module, and the second compressor is located at the end of the TTF linac at 480 MeV. The effective longitudinal emittance is diluted by the combination of three effects : the curvature of the RF waveform, the longitudinal wakefields and the space charge forces. The compressions take place at an energy sufficiently high that space charge effects can be, at first order, neglected. However, when the bunch is very short, specially in the extended 0.5-1 GeV section, the longitudinal wakefields are strong enough to increase the energy spread at the linac exit significantly. On the one hand, the wakefields cannot be corrected by the accelerating RF curvature, because the bunch is too short. On the other hand, we could hope to add a correlated energy deviation, which would be removed by the induced wakefields during the subsequent acceleration. Unfortunately, this ideal energy correlation after the last compressor cannot be easily generated, because of the bunch wake shape, which is strongly peaked around the center.

The knowledge of the wakefields, which is not easy for such short bunches, is hence of primary importance to study the development of phase space through the entire compressor-accelerating system. Time domain cavity codes, like ABCI, allowed wake computations through the 1 meter long TESLA cavity (with outer beam tubes larger than the inner iris diameter) for bunches as short as 50 μm. A fit of the Green function of the longitudinal wake per cavity at very short distances, could be deduced from the computed loss factors for different bunch lengths (figure 1) :

$$W_{z(s)} = -\frac{2.83}{s^{0.5}} + \frac{12.39}{s^{0.35}} - \frac{29.8}{s^{0.1}} \quad (V/pC)$$

In order to optimize the energy correlations and the compressor parameters (cavity phase and R_{56} coefficient), a computer program, taking into account the effects of longitudinal wakefields and the curvature of the RF wave, was used. The longitudinal

wake of the bunch is re-calculated after the injector and after each compressor from the convolution of the Greens function with the bunch charge, whose distribution is not necessarily gaussian.

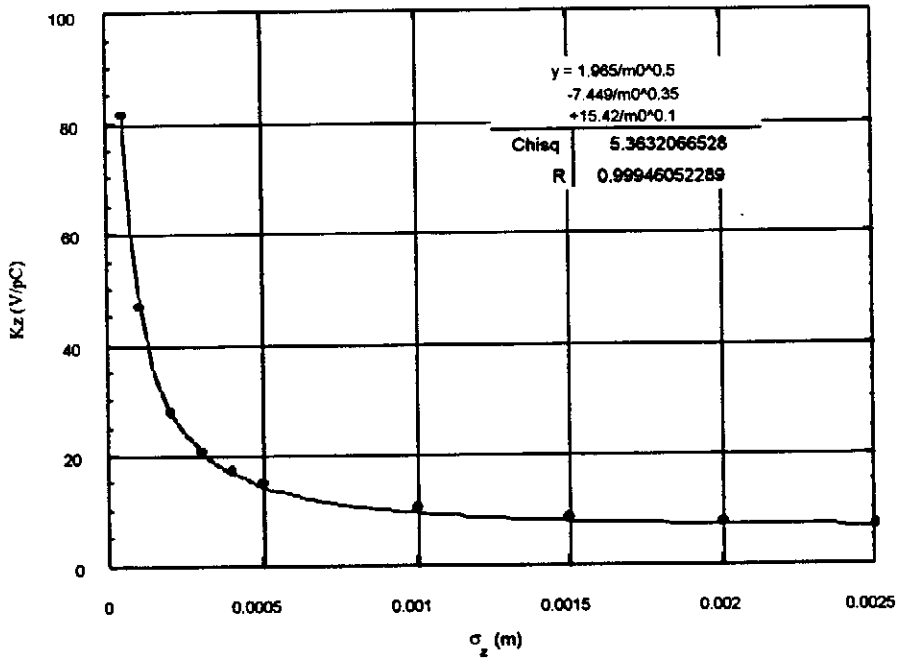

Figure 8.1 : Computed loss factor (V/pC) per cavity for different bunch lengths

As mentioned previously, the full compression-accelerating scheme has to be a compromise between the peak current and the energy spread. A possible set of parameters, which minimizes both final bunch length and energy spread, is listed in table 8.1. An uncorrelated rms energy spread coming from the injector of 3 10^{-3} was assumed. The two subsequent compression factors are slightly lower than 3 and 7.

modules	RF phase (deg)	R_{56}	bunchlength rms (μm)	energy spread rms (10^{-3})
1	8	- 0.20	385	3.1
2-to-4	14	- 0.14	56	2.6
5-to-8	0	...	56	1.4

Table 8.1 : set of parameters

Figure 8.2 shows the calculated longitudinal wake in the last 0.5-1 GeV section. The final beam phase space, energy distribution and bunch charge density are shown in Figures 8.3, 8.4 and 8.5. The apparent lines in Fig. 8.3 (only a few lines are drawn) give an insight into the phase space distortion due to the uncorrelated energy spread coming from the injector. The long energy tails are then removed at the exit of the linac to meet the energy spread requirement. Fig. 8.5 points out a gaussian shaped longitudinal distribution, with a peak current reduction of about 15 % after the energy tails are cut.

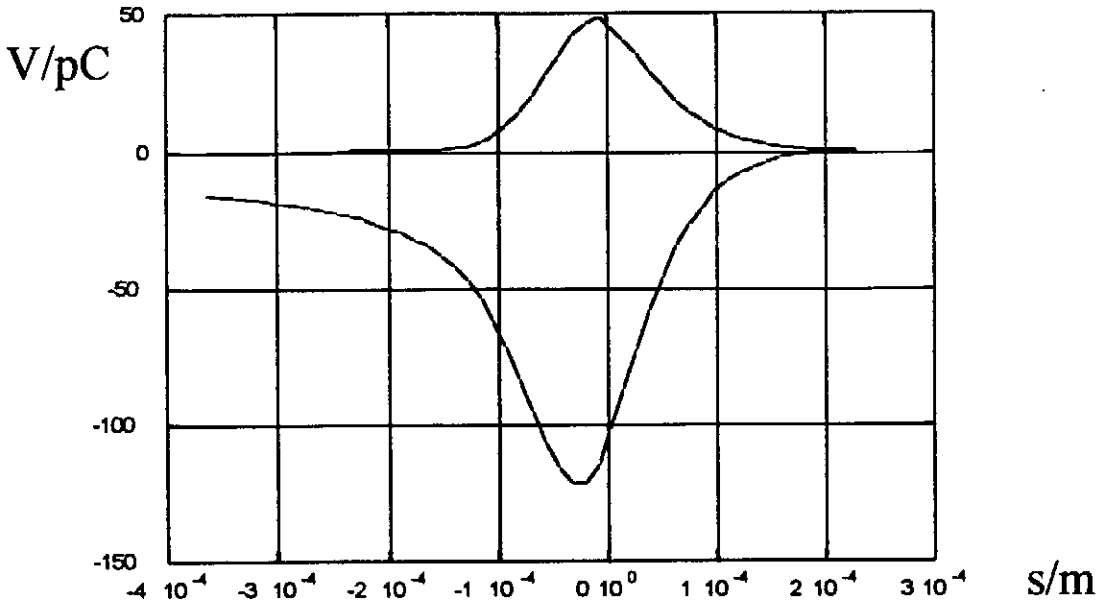

Figure 8.2 : Charge distribution (upper curve, arbitrary units) and bunch wake (V/pC) in the 0.5-1GeV section

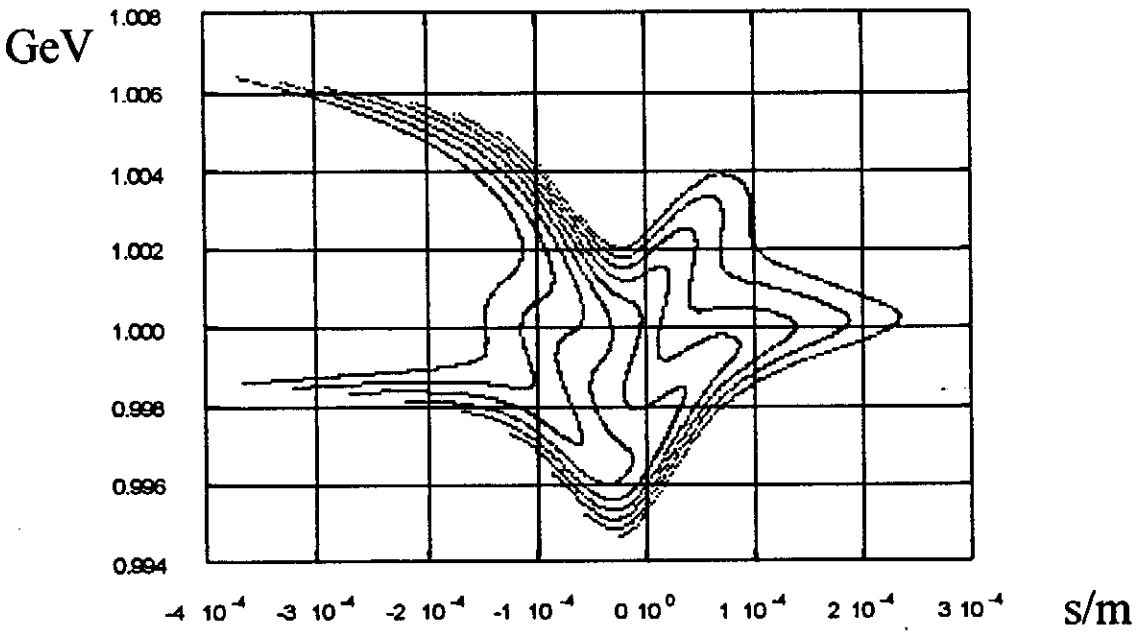

Figure 8.3 : Longitudinal phase space (GeV-m)

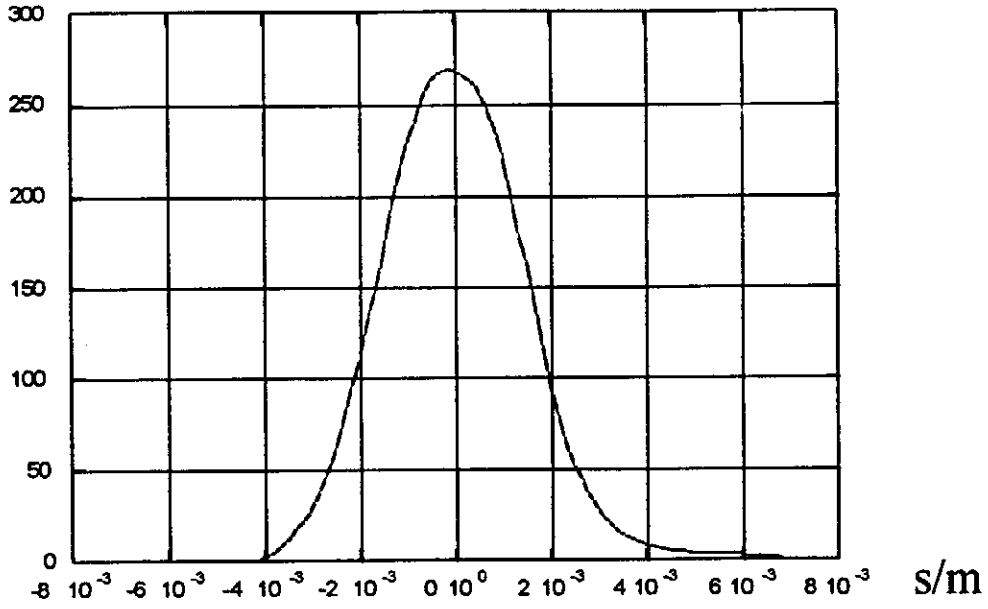

Figure 8.4 : Energy distribution before energy tails cut (arbitrary units)

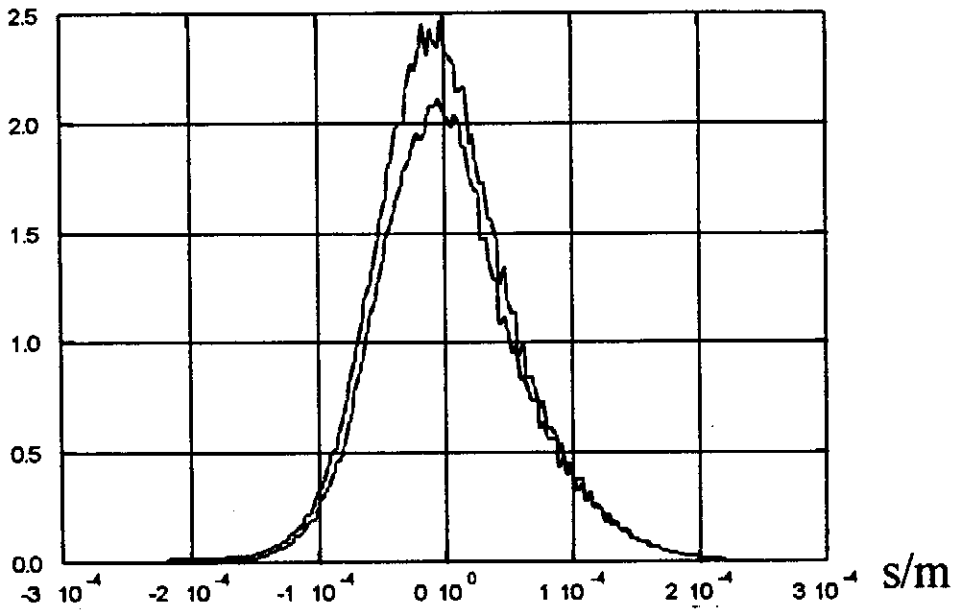

Figure 8.5 : Charge distribution before and after energy tails cut (arbitrary units)

Phase and charge jitter from the RF gun will change the final bunch length and peak current, because the energy correlation and the wakefield strength will vary. While the tolerance to incoming charge jitter is rather large (more than ± 10 %), the tolerance to incoming phase jitter is more severe. An injection phase jitter of 1 degree peak-to-peak (-0.3° and +0.7°) corresponding to 1 ps will induce a 10 % variation of the beam current or the bunch length.

We finally note the resistive wall wakefields in the undulator. Although the vacuum chamber in the undulator will be smooth, there will be nevertheless wakefields due to the finite conductivity of the vacuum pipe material. The corresponding broadening of the beam energy has been investigated, using an analytical expression for the longitudinal

resistive wall wakefield of a point-like charge in a circular vacuum pipe of radius r (K. Bane: SLAC-AP-87, June 1991). After convolution with a Gaussian charge distribution, the resulting rms energy broadening in shown in Table 8.2.

pipe radius [mm]	energy broadening for Cu	energy broadening for steel
5	0.034 %	0.21 %
4	0.043 %	0.28 %
3	0.059 %	0.37 %
2	0.097 %	0.55 %

Table 8.2: Rms energy broadening of a Gaussian charge distribution of rms bunch length 50 μm from resistive wall wakefields in the undulator. The electron energy is 1 GeV, the total charge is 1 nC, the undulator is length 30 m. Two different vacuum pipe materials have been considered: copper (conductivity = $5.9 \cdot 10^7$ 1/Ωm) and stainless steel (conductivity = $1.4 \cdot 10^6$ 1/Ωm). The calculation starts with a monoenergetic beam.

It is seen that for a copper pipe with diameter > 10 mm, the energy broadening is well below the tolerable rms energy width of 0.1 %. Stainless steel cannot be used (or must be coated). Note that the wakefield actually generates a correlated energy distribution along the longitudinal coordinate of the bunch, so that the effect within distances comparable to the cooperation length is considerably smaller.

8.2 Transverse phase space

The focusing system of the TTF linac is composed of quadrupole doublets, scaled with the beam energy and located at the end of each cryostat. It also includes correction magnets and beam position monitors for beam steering. We assume that the beam is matched to the focusing lattice and that any focusing mismatch has been removed. The beta function along the extended TTF linac is reproduced on Fig. 8.6. We note the perturbation of the lattice periodicity at the beginning due to the RF focusing properties of the cavities. The two magnetic compressors take place between the accelerating modules 1-2 and 4-5. The major sources of transverse emittance dilution are dispersive effects, transverse wakefields, space charge forces and RF deflections. In the same manner as for the longitudinal case, the transverse wake can be estimated from transverse loss factor computations with short bunches (figure 8.7). A fit of the Greens function of the transverse wake per cavity at very short distances is then deduced :

$$W_{\perp(s)} = 720\, s^{0.41} \quad (V / pC / m)$$

These wakefields effects, which are roughly proportional to the bunch length, are very weak, specially in the 0.5-1 GeV extended part, where the bunch is very short.

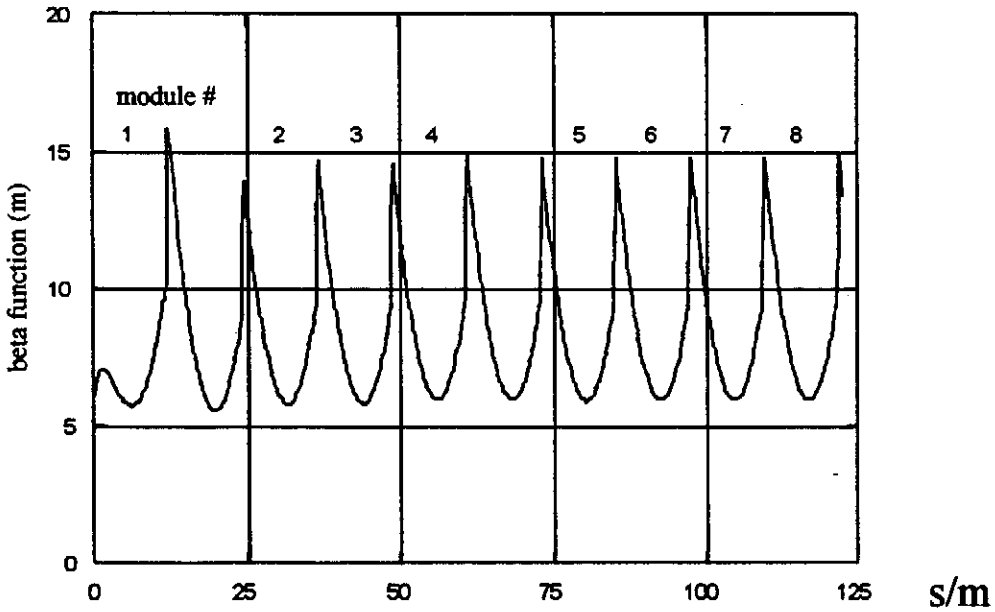

Figure 8.6 : Beta function (m) along the TTF linac

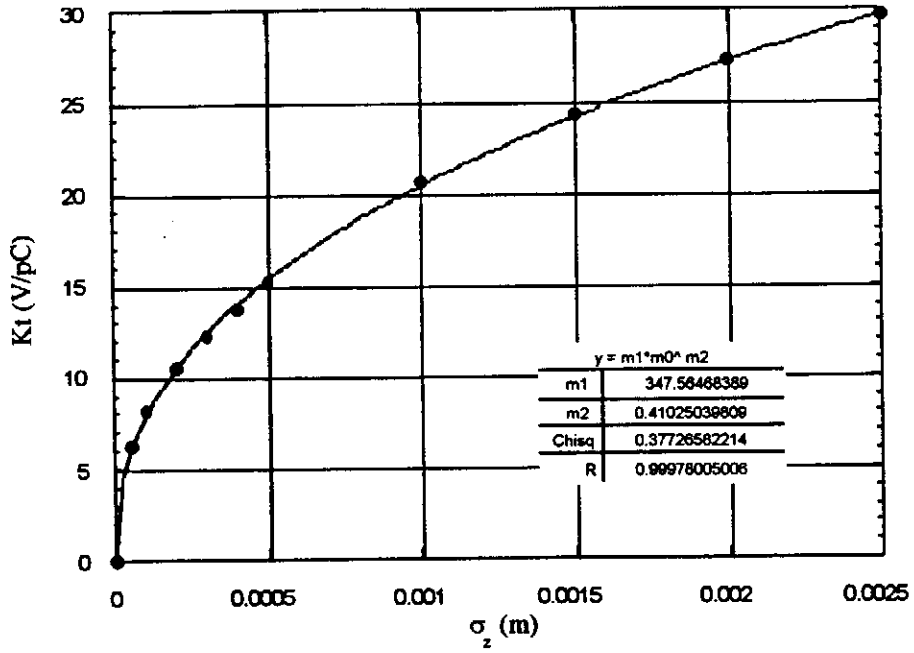

Figure 8.7 : Computed transverse loss factor (V/pC/m) per cavity for different bunch lengths

These effects have been modeled in the whole linac, including the bunch compressors, by means of the DILEM code. Since the bunches are compressed at relatively high energy, the space charge forces are expected to be nearly harmless and have been ignored. Because the number of focusing magnets is small and the beam energy spread is always small along the linac, lower than 0.5 %, the dispersive errors will not be significant after a one-to-one correction. Alignment errors as large as 500 μm for the quadrupoles and 150 μm for the BPMs (relative to the quadrupole center) have been assumed. If beam-based alignment techniques are used, these errors will be of course lower. Angular errors of the accelerating structures - rms errors of 1 mrad have been assumed - give rise to RF deflections, whose steering effect depends on the longitudinal position within the bunch. RF kicks due to couplers are expected to be much lower. In addition to rms cavity offsets of 1 mm, a transverse beam jitter at the linac entrance of 1 mm, more than two times the beam size, was also included. Taking into account all these errors, the computer simulations give a very low emittance growth, 1.5 % average value for 50 different seeds. Fig. 8.8 shows a typical plot of the emittance growth along the linac. The visible spikes occurring at the doublets are not serious and result from the fact that only one corrector for two quadrupoles was used in the simulations.

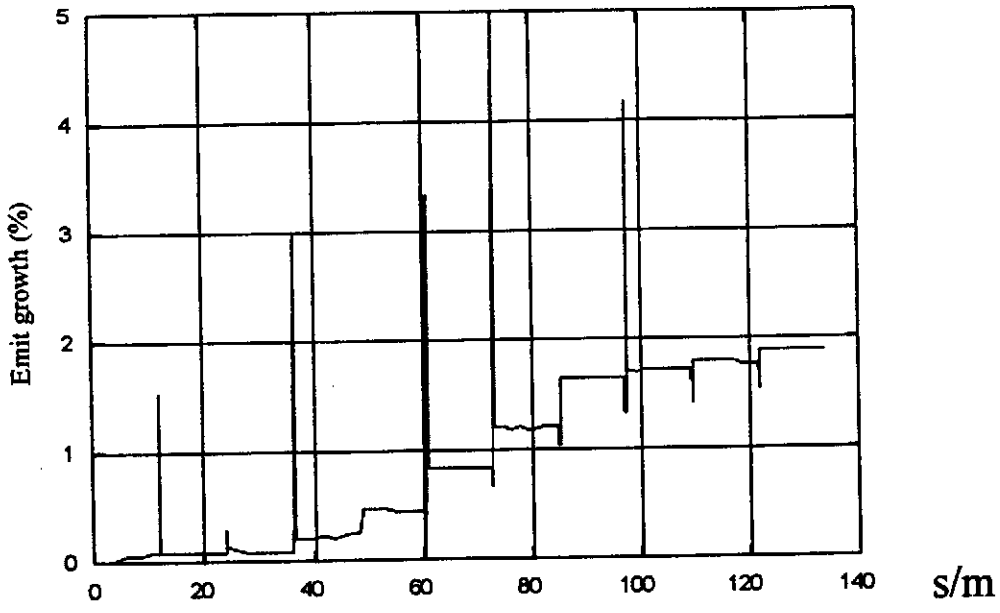

Figure 8.8 : Emittance growth (%) along the linac

9 Electron Beam Diagnostics

9.1 Electron Beam Parameters and Diagnostics

Beam diagnostic instruments such as beam size or intensity monitors are essential to understand and operate the TTF Linac. A sufficient number of monitors used in combination with optical elements like quadrupoles or steering dipoles is required to transport the beam from the injector towards the undulator. In addition it is necessary to determine and control the beam parameters at the entrance and along the undulator. The diagnostics must be adequate to optimize the laser light output. The phase space at the entrance to the undulator is determined by:

- the RF photoinjector
- 1st bunch compressor
- 1st superconducting acceleration section
- 2nd bunch compressor
- 2nd superconducting acceleration section
- 3rd bunch compressor
- 3rd superconducting acceleration section
- diagnostics section in front of the undulator.

Relevant parameters to be measured at these locations include bunch length and momentum spread. Behind that the undulator follows. In addition, to achieve an optimum laser light output from the undulator, it must be verified that electron and photon beam overlap along the entire length. Finally, the electrons must be separated from the 200 eV photon beam, momentum analyzed and safely dumped. The beam spot at the front side of the dump must be larger than $\sigma_x\sigma_y = 2.25$ mm^2 (rms values) to avoid a damage of the entrance window.

The beam parameters determine the type and design of the diagnostic tools to be installed. Table 9.1 summarizes the global beam parameters that do not change with position along the linac.

number of electrons per bunch	$6.24 \cdot 10^9$
bunch separation / ns	111
maximum number of bunches per bunch train	7200
repetition rate of bunch trains / Hz	10
transverse emittances (x/y), $\gamma\sigma^2/\beta$ / π mm mrad	1

Table 9.1: Beam parameters that do not change with position along the linac.

The emittance values given in Table 9.1 correspond to rms beam sizes of about 2 mm · $(MeV/E)^{½}$ at the entrance or exit of each superconducting acceleration section and rms divergences of about 0.3 mrad · $(MeV/E)^{½}$ in both planes. Table 9.2 lists the beam momentum, the momentum spread and the bunch length at various positions along the linac.

Section	Momentum / MeV/c	rms Momentum spread / %	rms bunch length / μm
injector	20		1500 - 2000
1st bunch compressor	20	1.00	800
1st superconducting acceleration section	140		800
2nd bunch compressor	140	0.50	250
2nd superconducting acceleration section	510		250
3rd bunch compressor	510	0.14	50
3rd superconducting acceleration section	1000	0.09	50

Table 9.2: Beam momentum, momentum spread and bunch length at various positions along the linac.

To optimize the Free-Electron Laser operation the knowledge of the length, the momentum spread and the charge of each individual bunch is helpful; however, this requirement is difficult to achieve at all locations along the linac (see section 9.3).

9.2 Diagnostics Components

The diagnostics components proposed at the different sections of the accelerator are:

9.2.1 Injector

- Position and profile: 2 fluorescent screens with mirror and CCD-camera (at the exit of the photoinjector and at the exit of the injector linac)
- Intensity: 2 integrating current transformers (at the exit of the photoinjector and at the exit of the injector linac)
- Transverse emittance: emittance slit mask with Cerenkov radiator and moderate-speed streak camera (at the exit of the photoinjector and at the exit of the injector linac)

9.2.2 1st Bunch Compressor

- Position (profile) : fluorescent screen / Optical Transition Radiation (OTR) radiator with CCD camera and stripline monitor (at the exit of the compressor)
- Momentum: stripline monitor (at the symmetry point of the compressor)
- Momentum spread: Secondary Emission Grid (SEM) grid, fluorescent screen / OTR radiator with CCD camera (at the symmetry point of the compressor)
- Intensity: integrating current transformer (at the exit of the compressor) and the sum signal of each stripline monitor

- Bunch length: Moderate-speed streak camera (recording the incoherent synchrotron light emerging form the last dipole of the compressor)

9.2.3 1st Superconducting Acceleration Section (1 Module)

- Position: TM_{110} - cavity (in front of the quadrupole package)

9.2.4 2nd Bunch Compressor

- Position (profile) : 2 fluorescent screens / OTR radiators with CCD camera (in front of and at the exit of the compressor) and stripline monitor (at the exit of the compressor)
- Momentum: stripline monitor (at the symmetry point of the compressor)
- Momentum spread: SEM grid, fluorescent screen / OTR radiator with CCD camera (at the symmetry point of the compressor)
- Intensity: 2 integrating current transformers (in front of and at the exit of the compressor) and the sum signal of each stripline monitor
- Bunch length: High-speed streak camera (recording the incoherent synchrotron light emerging form the last dipole of the compressor) and Michelson interferometer (recording the coherent synchrotron light emerging form the last dipole of the compressor).

9.2.5 2nd Superconducting Acceleration Section (3 Modules)

- Position: 3 TM_{110} - cavities (in front of the quadrupole packages).

9.2.6 3rd Bunch Compressor

- Position (profile) : 2 fluorescent screens / OTR radiators with CCD camera (in front of and at the exit of the compressor) and button monitor (at the exit of the compressor)
- Momentum: button monitor (at the symmetry point of the compressor)
- Momentum spread: SEM grid, fluorescent screen / OTR radiator with CCD camera (at the symmetry point of the compressor)
- Intensity: 2 integrating current transformers (in front of and at the exit of the compressor) and the sum signal of each button monitor

Bunch length: Very high-speed streak camera (recording the incoherent synchrotron light emerging form the last dipole of the compressor) and Michelson interferometer (recording the coherent synchrotron light emerging form the last dipole of the compressor).

9.2.7 3rd Superconducting Acceleration Section (4 Modules)

- Position: 4 TM_{110} - cavities (in front of the quadrupole packages).

9.2.8 Diagnostics Section in front of the Undulator

- Position (profile): 2 fluorescent screens / OTR radiators with CCD camera (behind 3rd superconducting acceleration section and in front of the undulator) and button monitor (in front of the undulator)
- Transverse emittance: fluorescent screen / OTR radiator with CCD camera and slow as well as fast wire scanner (between to quadrupole doublets)
- Intensity: 2 integrating current transformers (behind 3rd superconducting acceleration section and in front of the undulator) and the sum signal of each button monitor
- Bunch length: Very high-speed streak camera (recording the incoherent OTR light emerging form one of the OTR radiators) and Michelson interferometer (recording the coherent OTR light emerging form one of the OTR radiators).

9.2.9 Undulator

- Position: 5 button monitors, 5 collimators and 5 silicon strip detector arrays (in the gaps between successive undulator modules).

9.2.10 Diagnostics Section behind the Undulator

- Position: 2 fluorescent screens / OTR radiators with CCD camera and two button monitors (behind the undulator and in front of the beam separation dipole)
- Momentum: button monitor (at the focus of the spectrometer)
- Momentum spread: SEM-grid, fluorescent screen / OTR radiator with CCD camera (at the focus of the spectrometer)
- Intensity: 2 integrating current transformers (behind the undulator and at the focus of the spectrometer) and the sum signal of each button monitor
- Bunch length: Very high-speed streak camera (recording the incoherent synchrotron light emerging form the beam separation dipole) and Michelson interferometer (recording the coherent synchrotron light emerging form the beam separation dipole).

To localize beam losses, loss monitors will be distributed along the accelerator at quadrupoles and other aperture limitations.

Streak cameras are very expensive. Using a light guide system (parabolic mirrors) the bunch length measurements behind the injector and the first and the second bunch compressor could be performed with one high-speed camera. A similar solution using one very high-speed camera instead of three is possible for measurements behind the third bunch compressor and at the diagnostics sections in front of and behind the undulator.

9.3 Components Details

This chapter describes technical details of the diagnostics proposed.[1]

9.3.1 Fluorescent Screen and Optical Transition Radiation Radiator

The fluorescent screens (TTF design) are made of 0.5 mm thick chromium doped ceramic targets (Cromex). The OTR radiators (TTF design) consist of 25 μm thick Kapton foils coated with aluminum. Both targets are mounted on top of the same retractable holder placed in the beam path at 45 degrees to the beam axis. The emerging light is detected by a CCD camera. Fluorescent screens are very sensitive but have a poor time response (≈ 10 ms) and can show a non-linear behaviour at full linac current. The spatial resolution is not much better than 1 mm. By comparison, the light output of the OTR radiator is much less but the time response is in the range of picoseconds which allows bunch-to-bunch measurements using an intensified gated camera. A resolution of 1μm for the beam position and 10 μm for the beam profile should be possible. Fluorescent screens as well as OTR foils are destructive monitors. They will be heated by the beam. In the case of a 10 μm beam spot (rms value) the bunch train must be shortened to about 1% of its nominal length. However, a 1 mm spot (rms value) is tolerable without any reduction of the macropulse.

9.3.2 Wire Scanners

A thin carbon wire is moved through the beam, and the current in the wire produced by the secondary electron emission is measured as a function of the wire position. The wire thickness as well as the minimum step size determine the resolution of the profile measurement. A wire thickness of 10 μm is proposed. The step resolution of the wire motion should be even smaller. Two different operation modes can be distinguished.

- Slow scan: The wire moves with a speed less than 1 mm/s so that the cumulative signal from each bunch train gives one data sample of the profile histogram. To avoid the melting of the wire the length of the macropulse must be shortened to a few bunches.
- Fast scan: The wire moves with a speed of more than 1 m/s so that the signal from each bunch of the bunch train gives one data sample of the profile histogram. The fast-moving wire will probably withstand the instantaneous heating of a macropulse if the beam size (rms value) is not smaller than about 10 μm.

Both operation modes cannot be realized with the same scanner; therefore, two scanners are proposed, a slow-moving version driven by a stepping motor and another fast-moving one driven by a DC motor.

[1] A more extended discussion of most of the diagnostics equipment is given in chapters 3 and 9 of the TTF Linac - Design Report.

9.3.3 Emittance Measurement

Two different methods are used to measure the emittance of the low-energy beam coming out of the injector and of the high-energy beam passing through the undulator.

- To measure the emittance of the injector a time-resolved technique is proposed, providing emittance measurement in one transverse plane as a function of the longitudinal position within the beam. The space charge dominated beam is brought to a non-ballistic waist (i.e. particles do not cross the axis) and collimated into several emittance dominated beamlets by a slit emittance mask. The beamlets retain the transverse temperature of the original beam, but at such reduced charge that space charge forces within the individual beamlets contribute negligibly to their momentum spread. The beamlets then drift several meters to allow the correlated transverse momentum time to impart a measurable transverse distance offset, and are passed through a Cerenkov radiator. The emerging light is recorded by a streak camera. The spread of the light from each beamlet may be analyzed to unfold the contribution due to the transverse temperature of the beam from the natural spread angle of the Cerenkov radiation. The centroid of the beamlets at the radiator provides the centroid of the transverse momentum spread, while the transverse position is known immediately from the separation of the collimator slits. From these data the transverse phase space of the beam may be reconstructed as a function of longitudinal position within the beam. The slit separations are chosen to ensure that light from adjacent beamlets does not overlap at the streak camera.

- To measure the emittance in front of the undulator the quadrupole scan method is proposed. The beam profile is measured as a function of the setting of a preceding quadrupole doublet. The beam size is a parabolic function of the inverse focal length of the doublet. The accuracy of the emittance measurement depends on the precision of the beam size measurement, and on the number of data samples. Assuming a 10 μm resolution, at least 10 measurements should be performed. To transport the beam during the scan through the following undulator a second quadrupole doublet behind the profiler is recommended.

9.3.4 Secondary Emission Grid

A SEM grid consists of a couple of parallel wires placed in the beam path. The incident beam releases secondary electrons from the grid. This mechanism provides a signal proportional to the beam current. Thus, a histogram-like plot of the beam profile will be available. The dispersion function at the symmetry point of the first bunch compressor amounts to about 10 cm and at the symmetry point of the second and third bunch compressor to about 40 cm. Horizontal beam sizes (rms values) of 1 mm, 2 mm and 0.6 mm result from the momentum spreads given in Table 9.2, respectively. A SEM grid consisting of 30 tungsten wires, 0.1 mm in diameter and 0.5 mm apart would be adequate. Preamplifiers collect the generated charge. The resulting signals are converted by a multichannel ADC with 10 Hz repetition rate. Each wire of the grid is hit only by a small fraction of the beam: as long as the beam size is not smaller than about 1 mm the grid should withstand the instantaneous heating caused by a complete bunch train.

9.3.5 TM_{110} - Cavity

The amplitude of the TM_{110} - mode excited in the cavity by an off axis beam yields a signal proportional to the beam displacement and the bunch charge. The phase relative to an external reference gives the sign of the displacement. Both polarizations of the mode need to be measured to obtain the beam displacement in both planes. Four pin feedthroughs span an orthogonal coordinate system. The cavity is a cylindrical pill-box cavity designed for a resonance frequency of f_{110} = 1.517 GHz (TTF design). The very short bunches excite other resonance frequencies also. Therefore the signals of two opposite antennas are combined in a 180° broadband hybrid circuit and the difference signal is filtered by a bandpass resulting in a common mode rejection (TM_{010} - mode) of more than 100 dB. Finally, the signal is mixed down to DC and converted by a 5 MHz ADC. The resolution of the monitor is expected to be some 10 μm. First experiments using a setup not optimized show a measured resolution of 100 - 200 μm.

9.3.6 Stripline Monitor

The stripline monitor consists of four 175 mm long, 50 Ω coaxial antennas, positioned 90° apart in azimuth in a 60 mm beam pipe (TTF design). The 216 MHz component is filtered from the beam signal and mixed down to 50 MHz. The monitor yields a current independent, almost linear position information. The resolution is expected to be better than 100 μm. The sum signal of two opposite electrodes provides a fast information on the beam intensity. Intensity variations of some percent should be detectable.

9.3.7 Button Monitor

To measure the position of very short bunches, button electrodes are favourable due to their increased sensitivity at high frequencies. Four standard 50 Ω pin feedthroughs are proposed as antennas. Filtering the difference signal of two opposite electrodes at 200 MHz with 10 MHz bandwidth, a resolution of less than 10 μm is expected, at least in the case of the undulator vacuum tube with 10 mm diameter.

9.3.8 Integrating Current Transformer

Current transformers do not affect the beam. They are small loops wound around a toroidal magnetic core with the traversing electron beam as the primary winding. A ceramic gap in the beam pipe is needed to bypass the wall current around the monitor. Integrating current transformers sum up the charge of the bunches. The resulting signals are sampled periodically with a repetition rate of less than 1 MHz. A resolution in the percent range is nominal.

9.3.9 Streak Cameras

A streak camera consists of a photocathode, a high speed sweeping device deflecting the photoelectrons released from the cathode, a microchannel plate based image intensifier, a phosphorus screen and a high resolution CCD camera. Commercial vendors can supply cameras with a minimum resolution of 200 - 300 fs. The resolution is defined as the FWHM of the response curve of the streak camera to an infinitesimally short light pulse. In principle streak cameras are able to measure the bunch length of an individual bunch if operated in the single-shot mode. The so-called synchroscan mode which measures

repetitively the same bunch of different bunch trains yields a better resolution. The maximum measurement repetition rate is some kHz. A severe disadvantage of high-speed streak cameras is the very high price.

9.3.10 Michelson Interferometer

The coherent synchrotron or OTR light produced by an electron bunch can be used to measure the autocorrelation function of the light pulse by scanning a Michelson interferometer. The Fourier transform of the autocorrelation function is the square of the absolute value of the spectral energy distribution of the light pulse. Due to the detectors available (bolometers, opto-acoustical detectors) this method is limited to bunch lengths smaller than 1 mm. The resolution improves as the bunch length decreases. To record one autocorrelation plot, many bunch trains are necessary. A single bunch measurement is not possible.

9.3.11 Collimator

A set of steering magnets in combination with a narrow collimator placed between two successive undulator modules allows the alignment of the electron beam with respect to the photon beam. The collimator and photon beam axis must coincide. Both beam maxima should overlap if the electron beam passes the collimator. If the electron beam hits the collimator, it loses energy in the collimator and will not be accepted by the beam separation optics behind the undulator. The energy loss per unit length at a depth of two radiation lengths of copper is about 125 MeV / cm. Multiple scattering and the development of the electromagnetic cascade enlarge the incoming beam size by about a factor of 100 to $0.5 \cdot 0.5$ $(mm)^2$ (rms values) resulting in a deposited energy density per bunch of about 2 J / cm^3. Further study using a simulation is required.

9.3.12 Silicon Strip Detector Array

To measure the relative position of the electron beam and the photon beam inside the gap between two successive undulator modules an array of silicon strip detectors is proposed. Four movable detectors span an orthogonal coordinate system and are placed in the tails of the beams. Both photons and electrons deposit energy in the detectors. Placing an e.g. 100 μm thick aluminum foil in front of the strips however, absorbs the 200 eV photons. The enlargement of the electron beam due to multiple scattering can be calculated. A difference measurement with and without absorber allows one to disentangle photon and electron beam profiles. A silicon strip detector formed of strips 25 μm apart and 10 μm thick is expected to have a spatial resolution of about 10 μm. A disadvantage of this monitor is the poor radiation hardness of the material. A total dose of 1 Mrad = $6.24 \cdot 10^{18}$ MeV / kg should not be exceeded. Each electron produces about 5600 photons resulting in 1.12 MeV deposited photon energy in the wafer. An electron loses about 0.12 MeV if passing a 300 μm thick detector. Assuming a rms spot size of $50 \cdot 50$ μm^2 the critical dose is reached after 35 bunch crossings if the complete beam hits the detector. Therefore, the strips should be placed at least 5 σ from the beam center and the bunch trains should be shortened to a small number of bunches. If hit only by the tails of the beams, both, wafer and absorber can withstand the instantaneous heating.

9.3.13 Beam Loss Detection System

Two different beam loss detection systems are planned:

- Beam transmission through an accelerator section will be measured by two successive integrating current transformers. Total as well as relative losses of some percent can be detected.
- Beam losses will be localized by a set of distributed HERA beam loss monitors each formed by two reverse biased PIN diodes mounted face-to-face and operated in coincidence mode to suppress the photon background.

10 The Undulator

10.1 General

The undulator is one of the central components of the VUV-FEL. There are several requirements and boundary conditions which have to be considered for the design of the whole system:

1. the radiation wavelength was chosen to be 6.42 nm which corresponds to E1 = 192 eV. It violates the diffraction condition

$$\varepsilon \leq \frac{\lambda_R}{4\pi}$$

   by only a factor of two assuming the normalized design emittance of 2 π mm mrad and that the TTF is operated at 1 GeV. This is considered to be tolerable.

2. there is a lower limit on the vacuum chamber aperture given by resistive wakefield effects which is estimated to be 8-10 mm. Assuming a thin circular beam pipe of this inner diameter and a wall thickness of 1 mm an undulator gap of 10-12 mm is possible. To be on the safe side a gap of 12 mm will be assumed in this conceptual design.

3. additional focussing is required in order to keep the beamsize small over the whole undulator length. A quadrupole lattice consisting of focussing and defocusing quadrupolar fields (FODO lattice) has to be provided. Optimum focussing parameters are essential in order to reduce the overall length of the undulator.

4. the total length of the undulator system is limited to 30 m. In numerical simulations the saturation length was found to be around 25 m. However, in order to have a tolerance budget to errors in some of the ambitious design parameters (e.g. energy spread and normalized emittance) additional space for more undulator length is highly recommended. Additional space might also be needed in a later stage of the project which is beyond the scope of this proposal.

5. there is no need to change the gap of the undulator. Tuning of the radiation wavelength can be done by tuning the electron beam energy. An undulator with a fixed gap can be mechanically much simpler. It is also easier to obtain a lower level of field errors with a fixed gap by using shimming and tuning techniques.

6. the whole undulator system will be subdivided into six modules of 4.5 m length. In the matching sections of 0.5 m between the modules, beam position monitors, beam steering elements, collimators and phase shifters will be placed. This subdivision into modules makes manufacturing more easy and allows greater flexibility.

Fig. 1 shows a sketch of the undulator section when all six modules are installed. The total length is 30 m. Each modules requires 5.0 m; 4.5 m for the magnet structure and 0.5 m for the matching section.
The FODO lattice which is superimposed onto the undulator field is also indicated. Its periodicity has to be preserved throughout the whole undulator and must not be perturbed by the matching sections. Preliminary dimensions may be found in Fig. 1. Only the concept of the undulator set up is shown. Details will be discussed in the following sections.

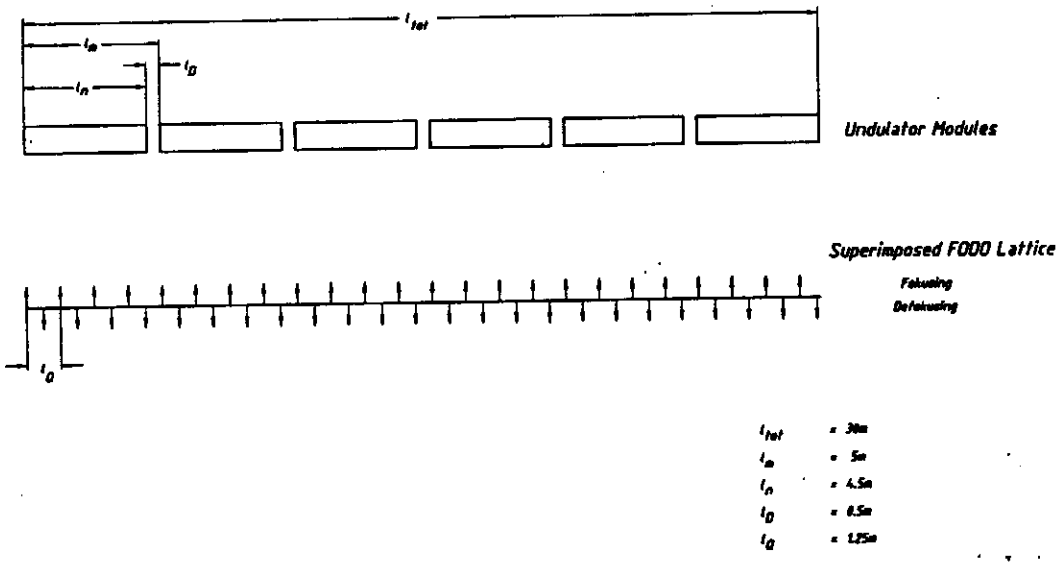

Fig. 1. General layout of the Undulator for the VUV-FEL at the TTF. A total length of 30 m is provided in which up to six undulator modules can be installed. There will be a periodic alternating gradient lattice superimposed to the undulator field. Focussing and defocusing sections are indicated. The parameters shown are preliminary design values.

10.2 Choice of magnet technology

For the VUV-FEL at the TTF an undulator is required which exhibits a short period length (below 3 cm) and a high field (about 0.5 T) at a gap of 12 mm. Detailed parameters will be discussed in the next sections.

There are two technologies which can be used to generate magnetic fields with the required strengths:

1. Superconductivity (SC).
   A superconducting helical undulator using a bifilar helical coil has already been used by Elias and Madey in their first FEL experiment in the 1970's [1]. They used a period length of 3.23 cm. The field of such bifilar helix containing no permeable material can be calculated analytically with formulae given in [2]. Recent investigations demonstrated the potential of this technology for the Stanford LCLS project [3]. Including high permeable material into the bifilar helix can increase the field strength significantly [4,5]. Although at the given geometrical parameters (gap/bore radius and period length) SC offers the highest possible field levels. There are, however, a number of severe problems which have to be solved before using this technique routinely in a very long undulator. These include:
   - fabrication techniques
   - fabrication induced field errors and tolerances
   - magnetic measurement techniques in long cold bores, with diameters below 10 mm
   - field error control / compensation
   - phase matching problem between undulator sections
   - superposition of an alternating gradient focussing lattice
   - alignment of the coil center of the cold undulator to the electron beam.

   Although none of these problems is considered to be unsolvable it requires a considerable R&D effort with an experienced staff.

2. Permanent magnets (PM).
   This technology on the other hand which uses Hybrid/NdFeB magnet arrays [6] is widely used in both synchrotron radiation (SR) sources and FEL's. At DESY/HASYLAB 10 insertion devices using PM technology are used routinely in DORIS III [7-10], one in PETRA [11,12]. All of the above mentioned problems have been solved for PM technology:
   - manufacturing techniques are readily available and extensive experience exists
   - fabrication errors can be controlled by high precision machining
   - a number of high precision magnetic measuring techniques have been developed and have become standard during the past years
   - field errors can be controlled using shimming and tuning techniques
   - phase matching of undulator modules is no problem
   - there are several design proposals to include quadrupolar focussing.

Although PM technology is clearly inferior to SC with regard to the achievable field levels it is for the above reasons why we propose PM for the VUV-FEL at the TTF.

10.3 Choice of undulator parameters

The undulator has to satisfy two conditions

1. The energy of the 1st harmonic should be 192 eV at 1 GeV.
2. The K-Parameter has to be larger than unity to keep the saturation length in an acceptable limit.

Assuming NdFeB/hybrid PM technology a maximum field

$$B_0[T] = 34.4 \cdot \exp\left\{-5.08\frac{g}{\lambda} + 1.54\left(\frac{g}{\lambda}\right)^2\right\}$$

can be assumed (g: gap, λ: period length). The relationship is valid for $0.07 < g/\lambda < 0.7$.

Fig. 2 shows the influence of the design gap on the choice of the period length under the restriction given by points 1 and 2. Fig. 2 also shows the effect of the gap on the K-value and the effect on saturation length, calculated using the formulae of Kim and Xie [13] assuming an average β–function of 3.0 m and the normalized design emittance of 2 mm mrad. Generally the lower the design gap, the shorter the design period length, the higher the K-parameter and the shorter the saturation length. For our design

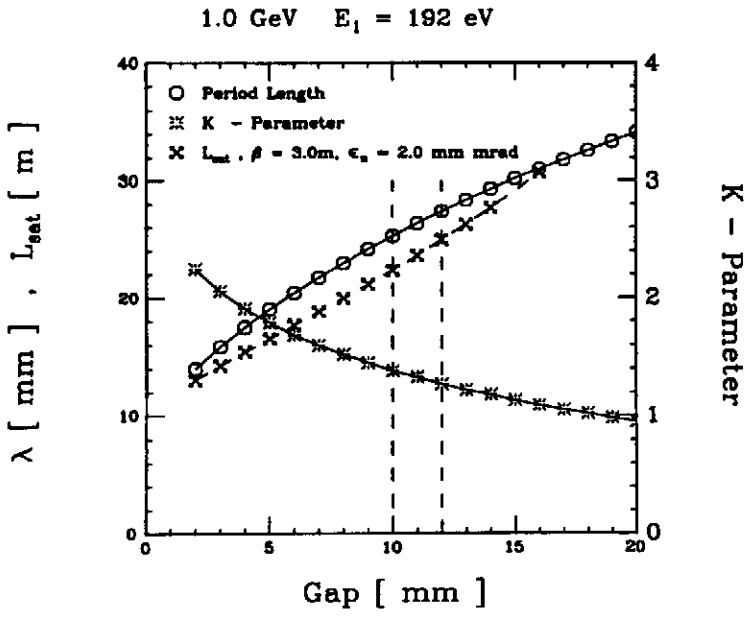

Fig. 2. Dependence of the period length, the K-parameter and the saturation length on the design gap. The constraint is to keep the first harmonic fixed at 192 eV. The dashed vertical line indicates the region of interest for the VUV-FEL at the TTF.

parameters, however, the formulae of Kim and Xie predicts a shallow maximum in the saturated power around a K of 2.

We assume a design gap of 12 mm resulting in the undulator parameters shown in the first column of Table 1. The second column shows the results if the design gap is chosen to be 10 mm. The lower gap value is a realistic option if resistive wall wake field effects can be shown to be tolerable. In the following sections, however, we shall assume the more conservative 12 mm design gap.

Table 1. Summary of undulator parameters

Design gap:	12 mm	10 mm
Period length :	27.3 mm	25.27 mm
Max. field :	0.5 T	0.584 T
K-parameter :	1.27	1.38
Radiation characteristics at 1.0 GeV		
γ:	1956	1956
Radiation wavelength:	6.42 nm	6.42 nm
Energy of 1st harmonic:	192 eV	192 eV
Saturation length, $\beta = 3.0$ m:	24.96 m	22.3 m
Saturation power, $\beta = 3.0$ m :	1.49 GW	1.622 GW

10.4 Undulator design

The undulator has two functions:

1. It has to provide the sinusoidal field so that the FEL process can take place. The values for the peak field and the period length are given in Table 1.
2. In order to keep the beamsize small over the whole undulator length an alternating field gradient caused by a superimposed quadrupole lattice has to be provided.

Using PM technology it is possible to generate fields which fulfill these requirements in one magnetic arrangement. Three alternative PM set ups are discussed in the following sections.

Fig. 3 shows a 3D view of a proposal by the group of Varfolomeev from the Kurchatov Institute in Moscow [14,15]. We shall abbreviate it by VU (for Varfolomeev Undulator). 1 1/2 periods are shown for numerical reasons. A regular hybrid structure provides the undulator field. An additional attachment consisting of two magnets mounted in the gap provides the quadrupolar focusing. Undulator period length and the length of the focusing attachment are completely independent. In fact it is possible to convert any regular planar undulator into a focusing one by using the additional side magnets. The focusing strength can be adjusted by changing the separation distance between the magnets.

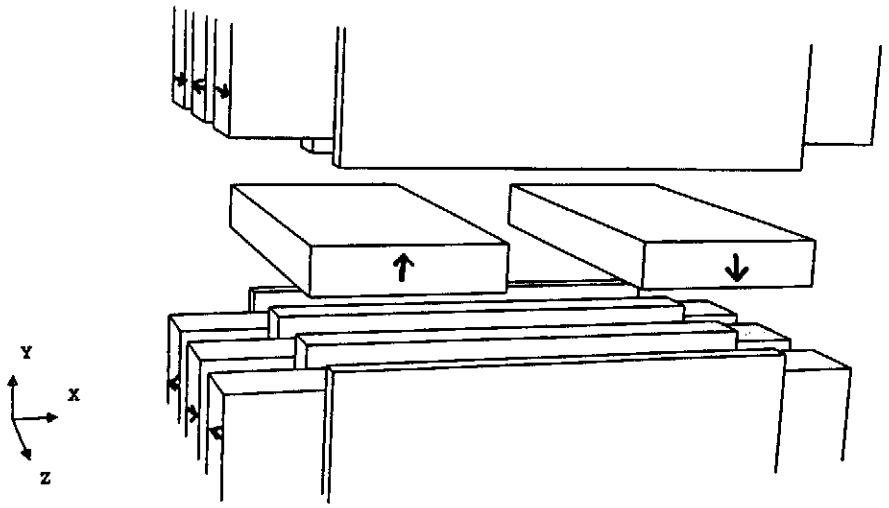

Fig. 3. 3-D perspective view of 1 1/2 period of a hybrid undulator following the proposal of Varfolomeev et al. (VU).

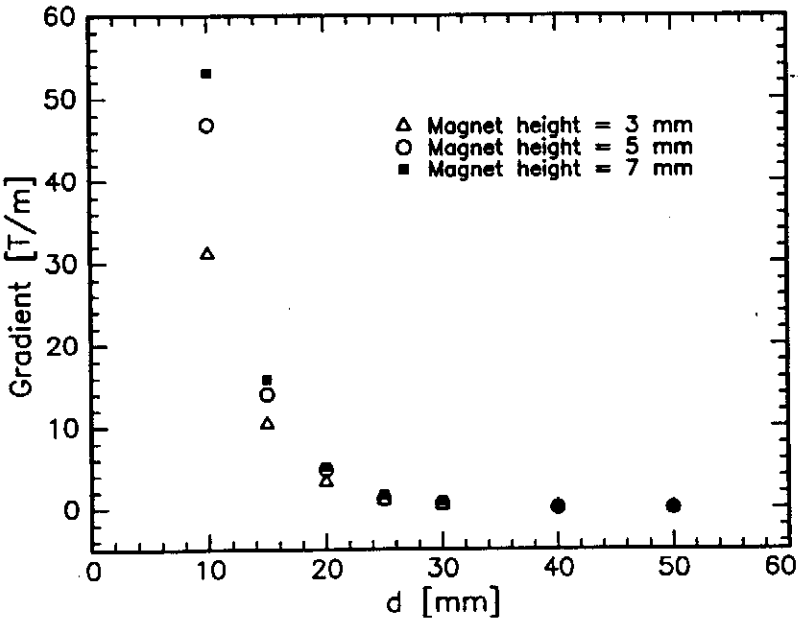

Fig.4. Field gradient of the VU as a function of the separation distance and the height of the focussing magnets.

The influence of a number of design parameters are studied in Figs. 4-7. Fig. 4 shows the dependence of the gradient as a function of the distance between the magnets for three different magnet heights. The distance has to be between 10 and 15 mm in order to obtain gradients well above 10 T/mm. Fig. 5 shows the influence of the magnet height at a relatively large distance, and show the optimum magnet height to be 7 mm. Fig 6 shows the influence on the magnet

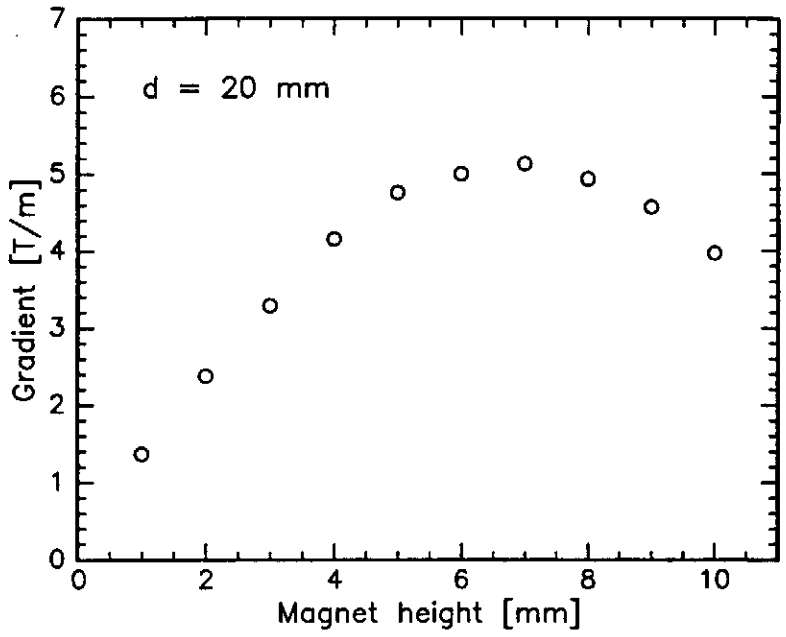

Fig. 5. Dependence of the gradient on the height of the focussing magnets.

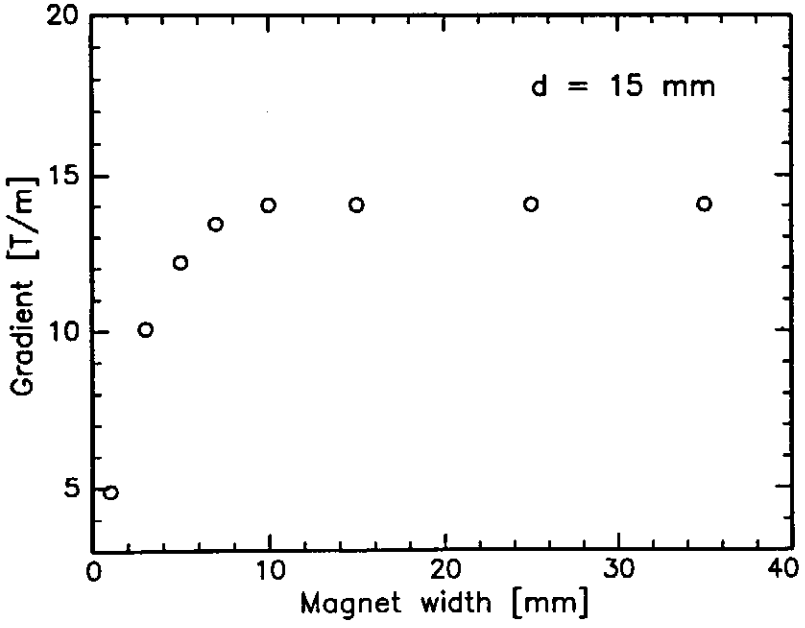

Fig. 6. Dependence of the gradient on the width of the focussing magnets.

width, and clearly shows that the gradient is practically constant above 10 mm. Finally Fig. 7 shows that the central peak field is not affected by the focusing magnets. This is of great importance if an alternating gradient structure is to be built in which sections with positive, zero, and negative gradient alternate; Fig. 7 shows that the peak field in this case does not change.

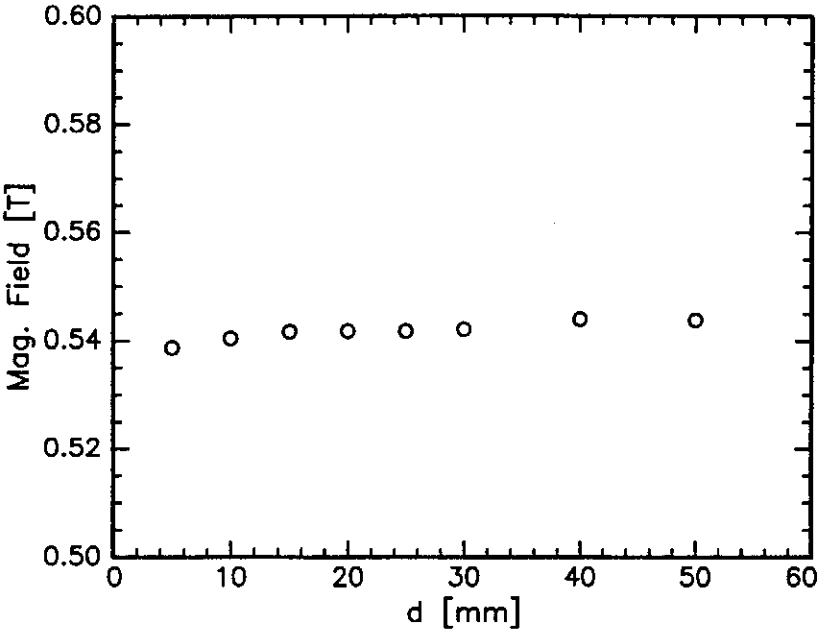

Fig. 7. Dependence of the peak field of the VU on the separation distance.

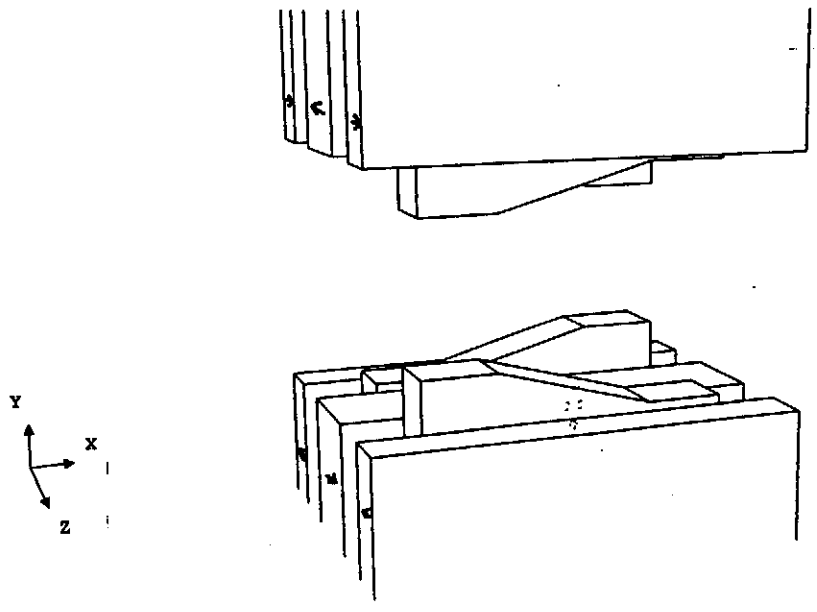

Fig. 8. 3-D view of one period of the tilted pole undulator (TPU).

In spite of its simplicity the VU has the disadvantage to almost enclose the beam. It might become very difficult to measure the exact field distribution at the beam position. Table 2a shows preliminary parameters which could be used for the VUV-FEL at the TTF. The height of the focusing magnets was chosen to be only 5 mm so that a clearance of 3.5 mm is left between the magnets and the pole tips. This might be sufficient to use a specially shaped field sensor to make measurements on the undulator axis.

Fig. 8 shows a second alternative the tilted pole undulator (TPU). The idea of the TPU is not new and was used in the past in several undulators for FEL's. Ref. 16 might serve as a good example. Ref. 17 is a more recent proposal for the LCLS at Stanford. The gap shown in Fig. 8 is opened out of scale so as to provide a better spacial impression. The poles are tilted alternatively near the beam axis and flattened for larger x-values for geometrical reasons. It can be shown that tilted pole faces give a good approximation to a scalar potential of the form [18]

$$\chi = \frac{B_{MAX}}{k} \cdot \sin h(k \cdot y) \cdot \cos(k \cdot z) + Q \cdot x \cdot y$$

where B_{MAX} is the peak field, Q the gradient, and $k = 2\pi/\lambda_0$, λ_0 being the period length, using the coordinate system as shown in Fig. 8. The magnetic field can be derived by

$$B = -\nabla \cdot \chi$$

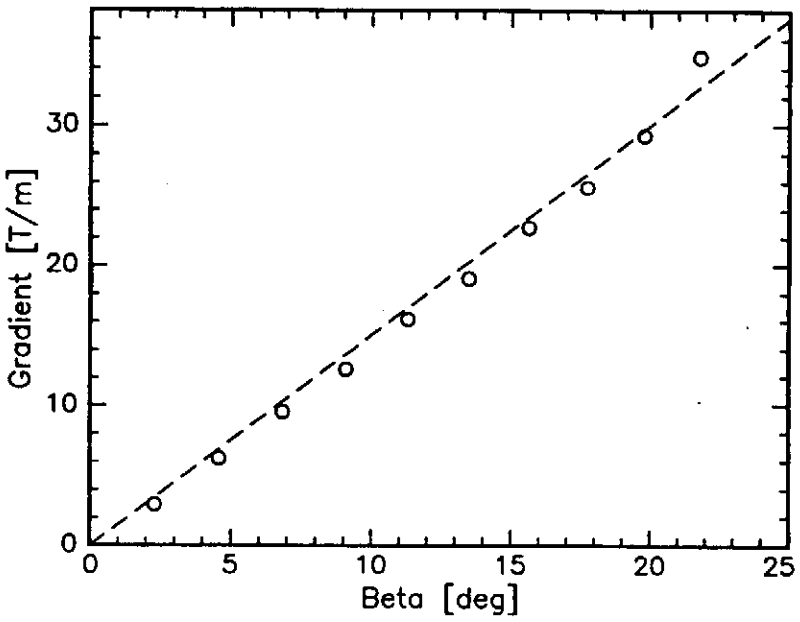

Fig. 9. Gradient as a function of the tilt angle. The dashed line was obtained by an analytic technique described in Ref. 18.

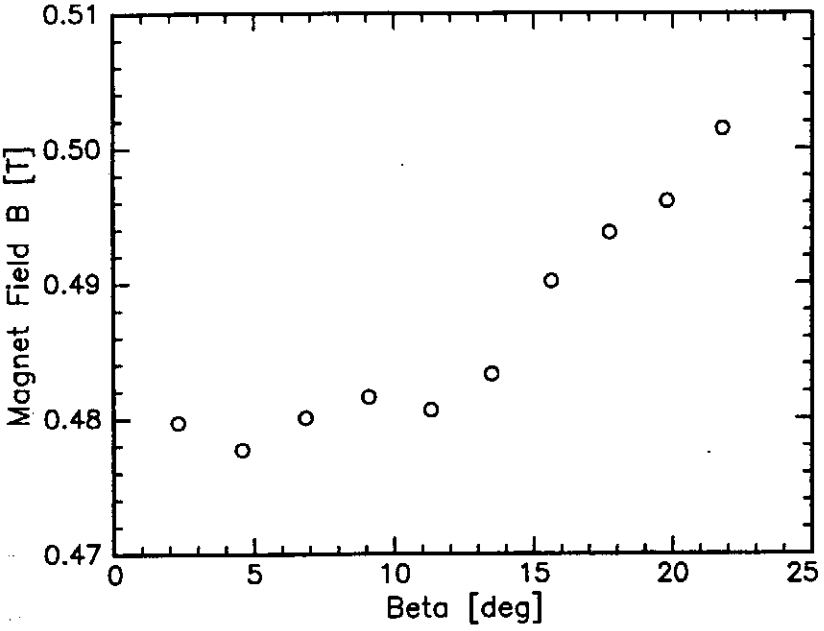

Fig. 10. Peak field dependence on tilt angle.

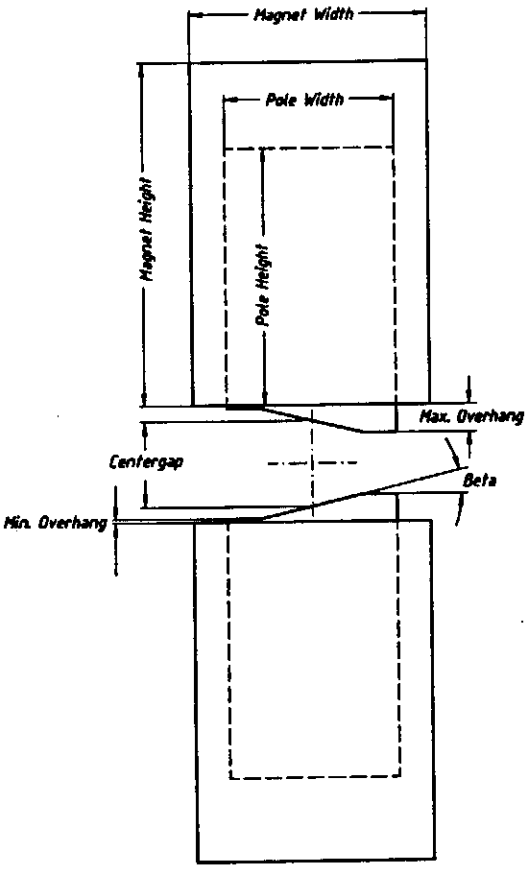

where ∇ is the gradient operator. In the vicinity of the z axis the field given by the pole arrangement shown in Fig. 8 is very close to the expected behaviour.

Fig. 9 shows the field gradient as a function of the tilt angle. The behaviour is almost linear. The dashed line shows the gradient calculated using the slope of the equipotential surfaces. This analytic method is described in more detail in Ref. 18. The agreement between both approaches is very good. One sees that at a tilt angle of about 15° a gradient of 20 T/m can be easily reached. In principle even higher gradients exceeding 30 T/m are possible. However, Fig. 10 gives an upper limit on reasonable field gradients. The undulator peak field as a function of the tilt angle is shown. It is seen that up to about

Fig. 11. Front view of the TPU giving the definitions of the tilt angle, the overhang and the center gap.

15°, there is only a minor effect on the peak field. Above 15° the peak field changes. For a TPU consisting of sections with positive, zero, and negative gradients this is of great advantage since it makes the transition between sections of different gradients simple and further adjustment may not be needed. Table 2b shows design values for a TPU which might be used for the TESLA-FEL. The magnetic width is considerably smaller than in the case of the VU allowing comparatively large tilt angles of the poles. Fig. 11 shows a cross-sectional view along the undulator axis for the design parameters shown in Table 2b.

Fig. 12 and 13 show the third alternative to be investigated [19]. The "staggered pole undulator" (SPU) is shown in a perspective view in two alternatives. The basic principle is demonstrated in Fig. 14. In an SPU the poles are staggered alternatingly to the right and to the left. First Fig. 14a demonstrates the situation in a normal undulator where the poles are unstaggered. A field profile of B_y along x is symmetric for positive and negative poles. If, however, the stagger is non-zero, the situation shown in Fig. 14b can be achieved. In this example positive poles are shifted to the left, negative to the right. Only electrons at x = 0 will suffer no deflection. At negative x-values there is now an excess of positive field and at positive x-values the opposite is true. In this way an approximate quadrupolar field near x = 0 is generated. In order to obtain an appreciable field difference the stagger has to be in the order of at least half of the pole width. In Fig. 12 the magnets are chosen very wide so that the overhang is larger than the stagger (SPU

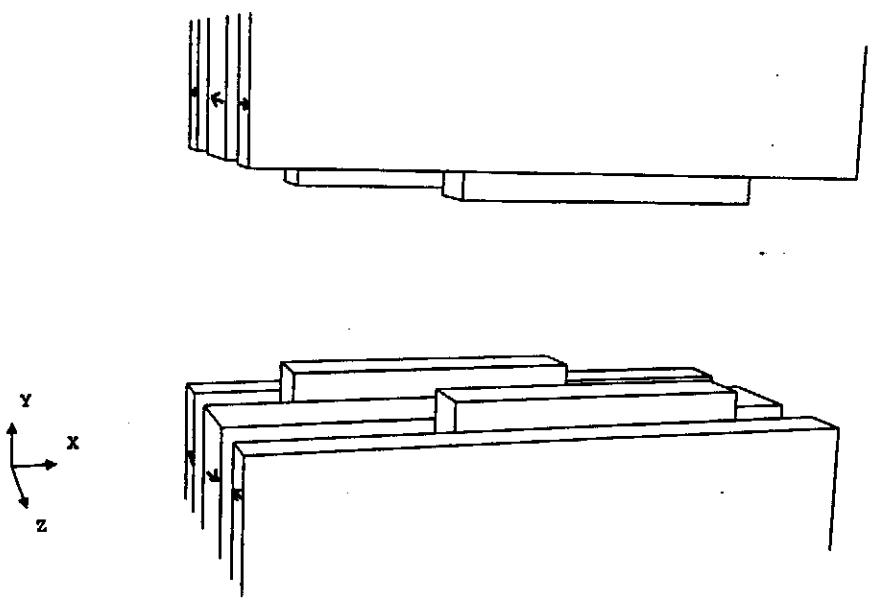

Fig. 12. 3-D view of the Staggered Pole Undulator using wide magnets (SPU I).

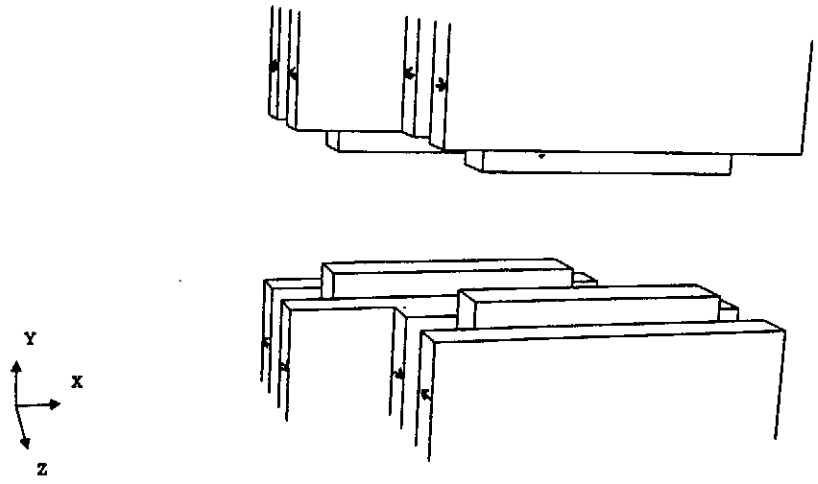

Fig. 13. 3-D view of the Staggered Pole Undulator including staggered magnets (SPU II).

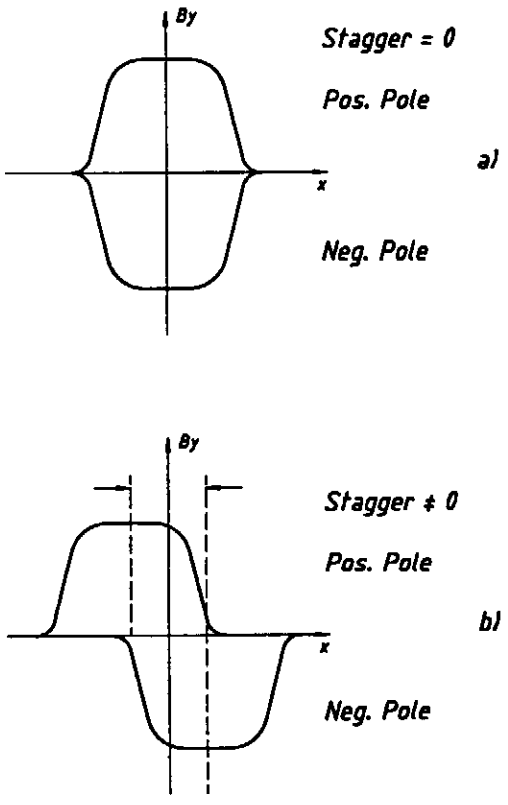

Fig. 14. Working principle of the SPU.

I). In Fig. 13 half of the magnet blocks are staggered (SPU II). Fig. 15 shows the gradient for the two SPU's as a function of the stagger. The gradient is very low until about 12 to 15 mm. At 20 mm about 15 T/m can be reached. In contrast Fig. 16 shows the peak fields as a function of the stagger. It differs by a few percent for the two types and is approximately constant up about 10 to 12 mm. In the region of higher gradients the peak field decreases by more than 10%. This decrease, however, makes the SPU not a good candidate for alternating gradient structures.

10.5 Comparison of Magnetic Designs

There are three magnetic configurations available to generate an undulator plus a quadrupolar field. For alternating gradient structures only the VU and the TPU are usable due to peak field variations in the SPU (Fig. 16). The inherent disadvantage of the VU is the need to enclose the electron beam leaving a rectangular hole of about 12 x 12 mm for a vacuum tube. Precise magnetic measurements, especially on long structures might be very difficult to perform. Although the height of the focusing magnet can be decreased to about 5 mm (Fig.5) the clearance between focusing magnet and undulator gap is still small and magnetic measurements are still problematic. On the other hand the focusing in the VU is by far the most flexible and its strength can easily be adjusted by varying the distance between the magnets (Fig. 4).

The TPU on the other hand offers free access from the side making precise measurements of magnetic properties straightforward. Tilt angles in the order of 15 ° will be needed for the VUV-FEL at the TTF. Fig. 11 gives a realistic cross-section. However, field quality and focusing strength are completely determined by the unavoidable assembly and fabrication errors. Low tolerances are therefore crucial in order to achieve the design goals.

Since the accessiblity of the gap is best in the TPU and the magnetic parameters are comparable with the VV this principle is proposed to be used for the VUV-FEL at the TTF.

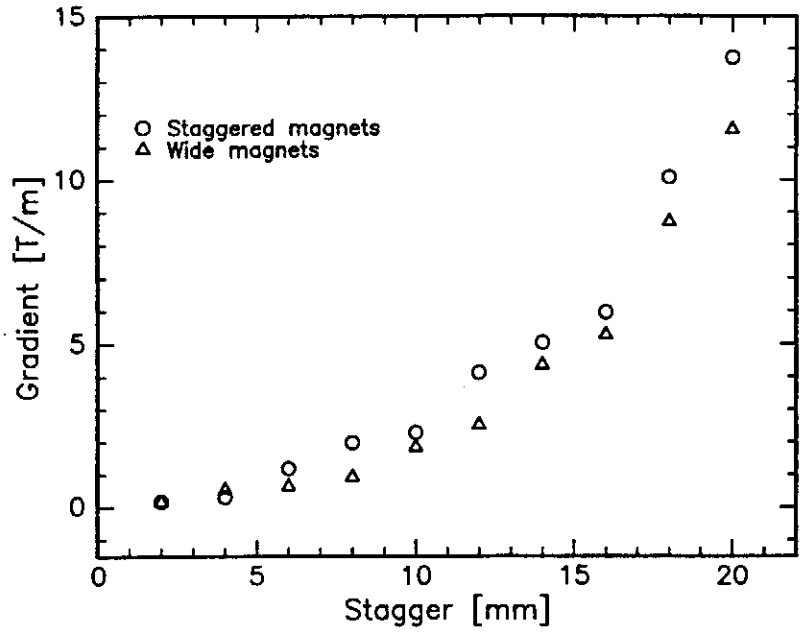

Fig. 15. Gradient as a function of the stagger (see also Fig. 12 and 13).

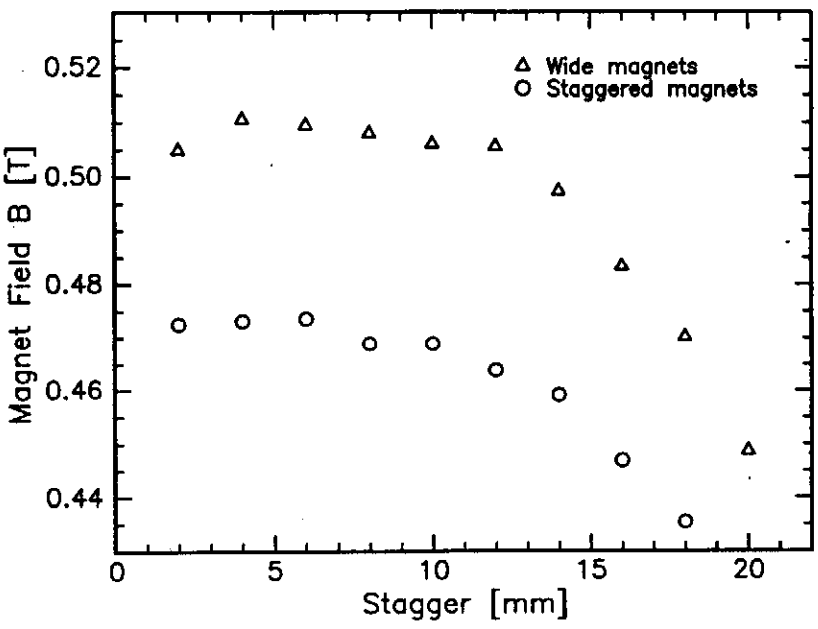

Fig. 16. Undulator peak field as a function of the stagger.

Table 2. Parameters and resulting performance of the three different undulator models.

a) Parameters for the VU (Varfolomeev undulator model)

Period length:	27.3 mm
Peak field:	0.54 T
Pole gap:	12 mm
Pole overhang:	0.5 mm
Focusing magnet separation:	12 mm
Magnet:	70x50x8.5 mm
Pole:	50x40x5.15 mm
Focusing magnet:	35x5xlength of quad.
Gradient:	~ 20 T/m

b) Parameter for the tilted pole undulator (TPU)

Period length:	27.3 mm
Peak field:	0.5 T
Center pole gap:	12 mm
Tilt angle:	~ 15 degree
Min. pole overhang:	0.5 mm
Max. pole overhang:	4.5 mm
Magnet:	35x50x8.5 mm
Pole (center):	25x40x5.15 mm
Gradient:	~ 20 T/m

c) Parameters for the staggered pole undulator with

1. wide magnets SPU I

Period length:	27.3 mm
Peak field:	0.445 T
Pole gap:	12 mm
Pole overhang:	2.5 mm
Magnet:	50x50x8.5 mm
Pole:	25.x40x5.15 mm
Stagger:	20 mm
Gradient:	~ 12 T/m

2. Staggered magnets as well SPU II

Period length:	27.3 mm
Peak field:	0.43 T
Pole gap:	12 mm
Pole overhang:	2.5 mm
Magnet:	35x50x8.5 mm
Pole:	25.x40x5.15 mm
Stagger:	20 mm
Gradient:	~ 14 T/m

10.6 References

1. L.R. Elias, J.M. Madey, Rev. Sci. Instr. 50(11) 1979
2. J.P. Blewet, R. Chasman, J. Appl. Phys.. 48, (1977) 2692
3. S. Caspi, LBL Report: SC-MAG-475, LBID-2052
4. S. Wipf, unpublished results
5. J. Pflüger in : Workshop on e^+ e^- Sources / Sep. 29 - Oct. 4, 1994, Schwerin Germany
6. K. Halbach, Journal de Physique, C1, suppl. 2, (1983) C1-211
7. HASYLAB Annual Reports 1987 through 1994
8. J. Pflüger, P. Gürtler NIM A287 (1990) 628
9. J. Pflüger, G. Heintze, W. Baran, D. Fernow, K. Kuntze, IEEE Trans. Mag. 28 (1992) 534
10. J. Pflüger, Rev. Sci. Instr. 63 (1992) 295
11. J. Pflüger, SPIE Vol. 2013, Conf. on Electron-Beam Sources of the High Brightness Radiation, July 13-14, 1993, San Diego, USA
12. HASYLAB Annual Reports 1993 / 1994
13. K.J. Kim, M. Xie NIM A 331 (1993), 359
14. A.A. Varfolomeev, A.H. Hairetokinov NIM A 341 (1994) 462
15. A.A. Varfolomeev, V.V. Gubankov, A. H. Hairetokinov, S.N. Ivanchenkov, A.S. Klebnikov, N.S. Osmanov, S.V. Tolmaev in : Proceedings of the 16th FEL Conference August 21-26, 1994, Stanford, USA
16. K.E. Robinson, D.C. Quimby, J.M. Slater, IEEE Journal of Quantum Electronics Vol. QE-23, 9 (1987) 1497
17. R. Schlueter in : Proceedings of the 16th FEL Conference August 21-26, 1994, Stanford, USA
18. "The Art and Science of Magnet Design", Vol. 2, p. 19 ff. , Workshop on Magnet Design, February 1995, Berkeley, USA.
19. J. Pflüger, unpublished results

11 FEL Process

11.1 General introduction to FEL theory

As was already mentioned in the introduction of this proposal, the SASE FEL [1,2] configuration offers some advantages with respect to the normal FEL amplifier or oscillator configurations. In particular, the SASE FEL does not need a seed laser to start the process, as with the standard FEL amplifier configuration, and no mirrors are needed, as in the oscillator configuration. Both the amplifier and oscillator FELs run into severe technical limitations when the operation regime is pushed into the XUV wavelength region. Nonetheless, much of the theory derived for the amplifier or resonator FEL still hold for the SASE FEL operation, the main difference in the case of the SASE FEL being the importance of the startup from noise.

As in all FELs, among the parameters of most interest we find the so-called ρ parameter [1]. This parameter can be deduced from the one dimensional (1D) Lorentz-Maxwell equations by rescaling them in order to obtain a system of dimensionless equations (universal scaling). With this working model it is possible to write very general scaling laws that allow the analysis of the FEL operation and the assessment of the potential fundamental limiting effects. The ρ parameter also determines the acceptance on the main beam and machine parameters [1,2,3] (as it will be shown in the following sections), and can be written as follows:

$$\rho = \left(\frac{1}{64\pi^2} \left(\frac{K\lambda_u f_B}{\sqrt{2}\gamma} \right)^2 \frac{I_p}{I_A \beta \varepsilon_n} \right)^{1/3},$$

where $I_A = 17$ kA is the Alfven current, I_p is the electron beam peak current, ε_n is the normalized transverse emittance, γ is the relativistic factor, $K = 0.9337 B_u[T]\lambda_u[cm]$ is the undulator parameter, f_B the decoupling factor, λ_u the undulator period, B_u the peak undulator field and β the beta function of the electron beam during the interaction in the undulator. The parameter ρ determines the gain length, saturation length and peak power. For the nominal TTF FEL parameters its value is approximately 2×10^{-3}.

The emitted FEL wavelength can be expressed in simple terms by the well known resonance condition, derived assuming that the force caused by the combined undulator and radiation fields, acting on the electrons, is stationary during the interaction along the undulator. For reference, we restate here the FEL resonance condition

$$\lambda = \frac{\lambda_u}{2\gamma^2} \left(1 + \frac{K^2}{2} \right).$$

In case the electron beam energy spread and emittance effects can be neglected, this is the resonant wavelength. In an actual SASE FEL, considering realistic effects like the beam energy spread and the finite electron beam emittance, the wavelength at which the system radiates is the one corresponding to the maximum gain. This maximum gain

wavelength is influenced by the forementioned electron beam parameters and generally shifted to a value slightly larger than the resonant wavelength shown before.

One important length depending on the ρ parameter is the gain length, i.e. the e-folding length of the radiated power, given in the 1D limit by:

$$\ell_g = \frac{\lambda_u}{4\pi\rho}.$$

For the TTF SASE FEL this value is about 1 m. The FEL exponential gain parameter G is then defined as the undulator length in units of the gain length, that is:

$$G = 4\pi\rho N_u,$$

where N_u is the number of undulator periods. High gain FEL operation is achieved when G is much greater than unity.

The peak power at the FEL saturation scales linearly with ρ:

$$P_{sat} \approx \rho P_{beam},$$

where $P_{beam}[\mathrm{GW}] = I_p[\mathrm{A}]E_k[\mathrm{GeV}]$ is the electron beam power. In this sense the parameter ρ is usually referred to as the FEL energy conversion efficiency. In addition, the 1D FEL theory shows analytically that in order not to depress the FEL gain the electron beam relative energy spread has to be smaller than ρ, in our case smaller than 0.2%.

One has to realize that all these relations only give a rough estimate of the FEL behavior. They have been derived in one-dimensional theory and additional equations related to transverse dynamics have to be included in order to describe more accurately the behavior of the system. One additional demand is the relation between electron beam emittance and wavelength. As stated in Ref. [3], the upper limit for the normalized emittance is

$$\varepsilon_n < \frac{\lambda\gamma}{4\pi}.$$

This condition leads to the crude first estimate that the normalized beam emittance should be smaller than 1π mm mrad for the operation at 6 nm. As it is shown in section 11.1.1 and by the numerical simulations, this condition is not very strict, so that one could tolerate also a slightly larger emittance (see Fig. 11.3).

A final issue that has to be considered is the influence of diffraction on the field. This is taken into account in all the simulation codes used for the exploration of the parameters of the TTF FEL proposal. Some additional insight in the influence of 3D effects on the choice of parameters is given in section 11.1.1

11.1.1 Inclusion of 3D effects for determining the optimal region of the FEL parameters

In 3D theory of the FEL amplifier the main parameters defining the operation are the gain parameter Γ (also known as D, see Yu et. al. in Ref. [3]), the diffraction parameter B and the saturation parameter ρ_{3D} [3,8]:

$$\Gamma = \left[\frac{8\pi^2 f_B^2}{\gamma \lambda_u^2} \frac{I_p}{I_A} \frac{K^2}{1+K^2/2} \right]^{1/2}, \quad B = \frac{4\Gamma \varepsilon_n \beta}{\lambda \gamma} = \frac{l_R}{l_g}, \quad \rho_{3D} = \frac{\Gamma \lambda_u}{4\pi},$$

with l_R the Rayleigh length. When the effects of the space charge field and energy spread are negligible, the main characteristics of the FEL amplifier can be expressed in terms of Γ, B and ρ_{3D}. The value of the inverse e-folding length of the radiation field is

$$\Lambda \approx \begin{cases} \Gamma B^{-1/3} & \text{for } B \geq 1 \\ \Gamma & \text{for } B < 1, \end{cases}$$

The efficiency at saturation $\eta_{sat} = P_{sat} / P_{beam}$ is given by

$$\eta_{sat} \approx \begin{cases} \rho_{3D} B^{-1/3} & \text{for } B \geq 1 \\ \rho_{3D} & \text{for } B < 1. \end{cases}$$

To obtain maximum efficiency and shorten the undulator length, it is necessary to focus the electron beam to provide the value of the diffraction parameter $B \approx 1$. When decreasing the electron beam size, i.e. decreasing B, the requirements on the value of the energy spread become to be less severe:

$$\frac{\Delta\gamma}{\gamma} \leq \begin{cases} 0.5\rho_{3D} B^{-1/3} & \text{for } B \geq 1 \\ 0.5\rho_{3D} & \text{for } B < 1. \end{cases}$$

Simultaneously, the requirements on the value of the emittance become more severe.

$$\varepsilon \leq \begin{cases} \lambda B^{1/3}/4\pi & \text{for } B \geq 1 \\ \lambda B^{1/2}/4\pi & \text{for } B < 1. \end{cases}$$

For the design parameters of the TTF FEL we have the following set of reduced parameters:

$$\Gamma \approx 2.33 \times 10^{-2} \text{cm}^{-1}, \quad B \approx 14, \quad \rho_{3D} \approx 0.005.$$

We see that, for these values, the safety margin in the nominal value of the emittance and the energy spread of the electrons is small. With the exception of the equation for the emittance, the equations given here, for the diffraction parameter B larger than unity, are close to the 1D relations given in the previous section (for example $\rho = \rho_{3D} B^{-1/3}$). Changing the value of the diffraction parameter B significantly from the nominal value would violate either the emittance or the energy spread condition. These simple estimations are in good agreement with the results of numerical simulations, as will be shown in the remainder of this chapter.

11.2 FEL design parameters

From semi-analytical formula [3] the parameter space has been investigated in order to find a rough parameter list meeting FEL physics requirements and other design considerations.

We start with the present machine parameters of the TTF linac. The super conducting (sc) linac will operate at 1 GeV and deliver a charge per bunch of 1 nC. The minimum longitudinal bunch length after 2 or 3 compression stages will be 50 μm. The minimum wavelength aimed at is 6 nm. This wavelength can be reached with the normalized emittance of 2π mm mrad according to the relation found in section 11.1.1. In order to obtain the correct wavelength, the undulator period has to be of the order of 2.5 cm at a K-value of 1. Small changes in K will not significantly change the period of the undulator. Very small values of K, choosen to decrease the radiation wavelength, are not advisable, since ρ (and hence the gain) decrease strongly with K. Larger values, however, are only possible with a superconducting undulator, an option which is not considered at this time. In addition, when high K-values are used to increase the gain, smaller undulator periods are needed in order to meet the FEL resonance at 6 nm.

In order to have $\rho \approx 2x10^{-3}$ with the given peak current of 2.5 kA (1 nC in 50 μm), the beta function is set equal to 3 m. From the analysis given in [3], as well as from the expression for ρ, we know that the β function has to be optimized. In order to go towards a small beta function, additional focussing must be used (see Chapter 10). Besides focussing, the FODO lattice currently envisaged has to fulfill two requirements. The first one is due to the modular setup of the undulator, with spaces between the modules up to 0.5 m. The periodicity of the FODO lattice has to be 1 m in order to prevent a quadrupole to lie in the space which is reserved for diagnostics and additional beam steering, thus making the space between the undulator sections even longer. A second and less severe demand is that the focussing gradient should not exceed 20 T/m: higher values are expected to give additional problems in building the undulator. Therefore the value for β equal to 3 m seems the optimum choice within the given constraints. For this value of β, the diffraction parameter B is approximately equal to 4.5 (see section 11.1.1).

With these parameters more or less fixed, the ρ parameter is determined to be around 2×10^{-3}. This sets a limit on the energy spread. Calculations of the gun, sc linac and bunch compressors show that the energy spread is expected to be 0.1%, i.e., sufficiently small to permit the FEL operation. A further bunch compression would increase the peak

Properties of TESLA Test Facility (TTF):	
Active length	66.5 m
Field gradient	15 MV/m
Electron beam properties at the beginning of the undulator:	
Energy	1 GeV
normalized emittance	2 π mm mrad
Emittance	1.02 π nm rad
External focusing β function	3 m/rad
Bunch width (1σ)	55 µm
Divergence (1σ)	26 µrad
Bunch length (1σ)	160 fsec
Number of bunches per bunch train	7200
Bunch separation	111 nsec
Repetition rate of bunch trains	10 Hz
relative energy spread (1σ)	0.1%
Bunch charge	1 nC
Electrons per bunch	$6.24*10^{9}$
Average power	72 kW
Peak power	2.5 TW
Average current	72 µA
Peak current	2500 A
Properties of the FEL undulator:	
Period length	2.73 cm
Undulator k value	1.27
Peak field	0.497 T
Magnetic gap	12 mm
Photon beam properties at the end of the undulator:	
Energy	193 eV
Wavelength	6.42 nm
Divergence (1σ)	28 µrad
Spectral bandwidth at saturation (FWHM)	1 %
Saturation length	19 m
Average power	70 W
Peak power	3 GW
Photons per bunch	$4*10^{13}$
Average flux	$3*10^{18}$ photons/sec
Peak flux	$1*10^{26}$ photons/sec
Average brilliance	$6*10^{21}$ photons/sec/ $mm^2/mrad^2/0.1\%$
Peak brilliance	$2*10^{29}$ photons/sec/ $mm^2/mrad^2/0.1\%$

Table 11.1: Parameter list for the SASE FEL on TTF

current but also increase the energy spread and for this reason decrease the gain. An increase in the bunch length would give a smaller energy spread as well as a smaller current. This would decrease ρ and therefore also the gain.

With ρ and the electron beam power given, the laser peak power is calculated around 5 GW. The gain length, as calculated in the previous section, is approximately 1 m.

In Table 11.1 we present a list of the nominal parameters chosen for the SASE FEL on TTF. The value of the spectral bandwidth given in the table includes estimates of the fluctuation in saturation length from pulse to pulse and is therefore larger than the value of 0.5%, which would be obtained from single pulse simulations using a time dependent model. The influence of variations of the parameters given in the table on the FEL performance will be studied in the next section.

11.3 Startup from noise

A SASE single pass FEL does not require any input field, since the spontaneous radiation emitted by a sufficiently intense electron beam entering the undulator drives the high gain instability. In this configuration the FEL would start from the random noise in the electron bunching. For a complete study of the shot noise startup the time dependence of the input noise and the slippage effects should be taken into account in the theory and in the simulations. The 1D analysis shows that a critical parameter for shot noise analysis is the beam length in units of the "cooperation length" [4]:

$$\ell_c = \frac{\lambda}{4\pi\rho}.$$

For the TTF FEL the cooperation length is 0.26 μm, and the beam length is 50 μm. In this case shot to shot fluctuations should be a fraction of a gain length and the use of an equivalent input signal analysis should be adequate. A more careful study with existing time dependent FEL codes (GINGER and FELEX) is in its starting phase and will be reported on soon.

11.3.1 The steady state analysis of the shot noise startup

In the steady state simulation model, no time structure of either the electron or radiation beams is taken into account, and a proper "equivalent input noise" has to be assumed in order to evaluate the necessary undulator length required to reach saturation. One possible estimate for the value of this equivalent input noise is to consider the spontaneous radiation produced in the first gain length of the undulator. The peak power radiated by an electron beam of peak current I_p and energy E_t in a undulator with a peak field B_u and a length L_u is given by the following formula (in practical units)

$$P[\mathrm{kW}] = 0.6327 \cdot L_u[\mathrm{m}] \cdot I_p[\mathrm{A}] \cdot E_t[\mathrm{GeV}]^2 \cdot B_u[\mathrm{T}]^2.$$

Using a gain length of about 1 m, this value would be approximately 400 kW for the SASE TTF FEL parameters. This power, however, would be radiated in a relatively broad band, $\Delta\omega/\omega \approx 1/N_u \approx 3\%$. The bandwidth of the high gain FEL amplifier is much smaller than this value, being approximately equal to the FEL parameter $\rho \approx 2\times10^{-3}$ [1,2].

The fraction of the emitted synchrotron radiation in this bandwidth is about 8% of the total power, leading to about 30 kW of equivalent input noise.

Another possible estimate of the equivalent input power can be evaluated from the shot noise current in the cooperation length [4], which gives the following approximate formula:

$$P[\mathrm{kW}] = 9.9687 \cdot 10^6 \cdot \rho^2 \cdot \frac{E_k[\mathrm{GeV}]}{\lambda[\mathrm{nm}]}.$$

In our case, this equivalent power due to the noise in the electron phases, averaged over the cooperation length, evaluates to 6 kW.

For input powers much smaller than the FEL saturation, only the saturation length depends on the magnitude of the input signal, while the peak power at saturation does not. The dependence of the saturation length on the input power is a very simple one. Retaining the linear analytical model up to saturation it follows that the saturation length is only logarithmically dependent on the input power, and

$$\Delta z_{sat} \approx \ell_g \ln\left(\frac{P_1}{P_2}\right)$$

is the saturation length change for an input signal P_1 larger (smaller) than the input signal P_2. For a gain length of approximately 1 m the saturation length increases by 2.3 m lowering the input signal by one order of magnitude. This scaling has been successfully tested using steady state 2D simulations.

In the following simulations a conservative estimate for an equivalent input signal of 1 kW has been assumed.

11.3.2 Time dependent analysis

In order to derive a quantitative estimate for the shot to shot fluctuations of the SASE process and to assess the spectral properties of the emitted radiation, a program of detailed 2D time dependent simulation [5] has been started with the use of the codes GINGER and FELEX (briefly discussed in a later section of this report).

An estimation of the shot to shot fluctuations based on 1D analytical and numerical models [4,6] predicts that random fluctuations of the saturation length are a major problem in the case of bunches shorter or of the order of a few cooperation lengths. In this case fluctuations can be of the order of several gain lengths. As the bunch length is increased the rms fluctuations decrease as $1/\sqrt{\ell_b/\ell_c}$. For the TTF FEL the fluctuations should be reduced to a small fraction of the gain length and should not play an important role, but careful 2D simulations are needed to confirm this.

Another peculiar characteristic of the SASE FEL is the strong spiking both in the temporal and spectral domain of the emitted radiation. Inhomogenities of the electron phases along the longitudinal position of the beam can seed superradiant instabilities and lead to the occurrence of strong radiation spikes. Preliminary calculations with GINGER, performed by W.M. Fawley (LBL) have confirmed the presence of strong spikes, with a

duration of the order of a cooperation length and peak power of few tens of GW, as in agreement with rough estimates based on 1D models. A detailed analysis of the statistical properties of these spikes is needed and has been recently started. The average emitted power along the undulator until saturation, however, does not significantly differ from the results obtained with time independent models. After saturation the FEL behavior is determined by the nonlinear regime of the spikes. The total linewidth (half width half maximum) has been estimated using GINGER to be of the order of the FEL parameter, ρ=0.2%, as expected from the 1D time dependent model.

J.Goldstein (LANL) has started a similar analysis with the code FELEX and the results show a larger saturation length than GINGER or the other steady state calculations, namely by 2-3 meters. Since the results have not been fully interpreted, they are not included in this report. Because of the importance of the study, however, the undulator design must have enough safety margin to allow for some additional length.

11.4 Exploration of the parameter range

In this section, the results of the extensive simulation activities that have been performed using different numerical codes will be discussed.

11.4.1 General considerations on the FEL codes used for the TTF FEL

A number of 2D/3D FEL simulation codes have been used for the analysis of the performance of the SASE proposal at DESY, and for the determination of the beam quality and parameter tolerances required for the successful operation of the facility.

We include in the following sections a short description of each code. For an overview of simulation codes for short wavelength amplifiers the reader can refer to Ref. [7] and the references cited in the following sections. A number of calculations done with the LANL code FELEX are not yet included, pending further study. The influence of shot noise, which is of particular interest for the analysis of a SASE FEL, has been studied in section 3 of this chapter. There the results obtained with FELEX and GINGER are briefly discussed.

FS2R

The program package FS2R [8] has been designed for calculations of the FEL amplifier with an axisymmetric electron beam. It consists of three codes: FS2RD (analysis of the eigenvalue problem), FS2RL (analysis of the initial-value problem) and FS2RN (nonlinear simulation code). Codes FS2RD and FS2RL are essentially based on the use of analytical techniques and FS2RN makes use of Green's function methods for the calculation of the radiation field.

NUTMEG and GINGER

NUTMEG and GINGER [9,10] are authored by E.T.Scharlemann and W.M.Fawley. The code development has been started in the 80's, the codes have been used as a simulation support for the LLNL FEL experiments and were successful in the predictions of the experimental data. Both codes consider a 2D axisimmetric radiation field and take into account the 3D electron motion in an undulator, allowing the user to describe an external

focussing field. All relevant 2D effects, like diffraction and guiding, effects of finite beam emittance and undulator errors, are included in the physical model used in the simulation.

NUTMEG is a steady state simulation code that does not include propagation effects, i.e. slippage between the radiation and electron beam. The code, as with all simulation codes based on the steady state theory (like TDA and FS2R), cannot take into account the finite length of the electron pulse, or any beam parameter dependence on the longitudinal position (current profile, energy distribution, etc.). NUTMEG can, however, model the higher harmonic components of the emitted radiation field and simulate multiple undulator schemes.

GINGER extends the model to include time dependent effects, and properly taking into account both any longitudinal structure of electron beam and radiation field, and the slippage between the pulses. GINGER can also model the shot noise startup by means of an incoherent random noise over the initial electron pulse without needing any equivalent input signal to start the SASE process, and can give information on the temporal and spectral characteristics of the emitted radiation.

TDA

The code TDA3D has been described in detail by Tran [11] and Jha [12]. It solves the electron equations in a six dimensional phase space and the wave equation in the paraxial, single frequency approximation. The wave equation is expanded into azimuthal modes to take into account non-axisymmetric effects in the interaction process. Equations are averaged over a wiggler period, with the exception of the error term in the wiggler field, used in the section 4.5 of this chapter. The focussing of the electron beam by the external FODO lattice is taken into account by adding an additional term in the differential equation for the electron momenta. The effect of space charge, which is also included in TDA3D, is not considered in the simulations presented in this proposal. Earlier calculations by NUTMEG have shown that it plays no role in the TTF FEL. The different azimuthal modes, of importance especially in case of wiggler field errors, is however taken into account.

In the following we show the results of NUTMEG calculations to illustrate the dependence of the saturation length and of the peak emitted power on the beam and machine parameters. Similar calculations have been performed with TDA3D and the FS2R [13] group of codes and the results are found to be consistent with what is presented in the following sections. TDA3D simulations show a longer saturation length of about 1 m and a lower emitted power by a factor up to 15%. This small discrepancy can be interpreted from the fact that TDA considers a full 3D radiation field structure and is the only code that models the discrete FODO lattice without approximating it to a smooth focussing (as NUTMEG), or considering the induced axial energy spread (as FS2R).

1.4.2 Influence of the beam energy spread and peak current

One of the most important parameters influencing the FEL gain is the energy spread. As is well known, the optimal, near 1D, FEL operation requires the relative energy spread $\Delta\gamma/\gamma$ to be smaller than ρ, the FEL parameter (2×10^{-3} for the nominal TTF parameters presented before). Due to the beam dynamics in the linac and in the buncher sections, a

reduction of the energy spread can be obtained lowering the beam current, therefore reducing the intrinsic FEL gain. Hence, the required beam coming out of the linac needs to be optimized for high current values while keeping the energy spread smaller than ρ. The nominal values chosen are a peak current of 2.5 kA and a corresponding energy spread of 0.1 %. These values are consistent with those obtained from simulations on the TTF linac dynamics. In this section, the influence of a larger energy spread on the FEL gain and saturated power is studied.

Calculations have been performed both at a normalized emittance of 1π and 2π mm mrad. At $\varepsilon_n = 2\pi$ mm mrad, an increase of a factor 2 in the energy spread brings the gain length to a value which does not lead to saturation within the undulator length of 25 m.

Figure 11.1 shows the peak power and saturation length as a function of energy spread for an emittance of 1π mm mrad. The peak power is approximately 7 to 8 GW at the nominal value of 0.1 % and decreases almost linearly to 3 GW at an energy spread equal to 0.2 %. At the same time, the saturation length has increased to 20 m. In view of the pulse to pulse fluctuations in power and gain depression effects due to wiggler field errors, this is the maximum saturation length that can be allowed for.

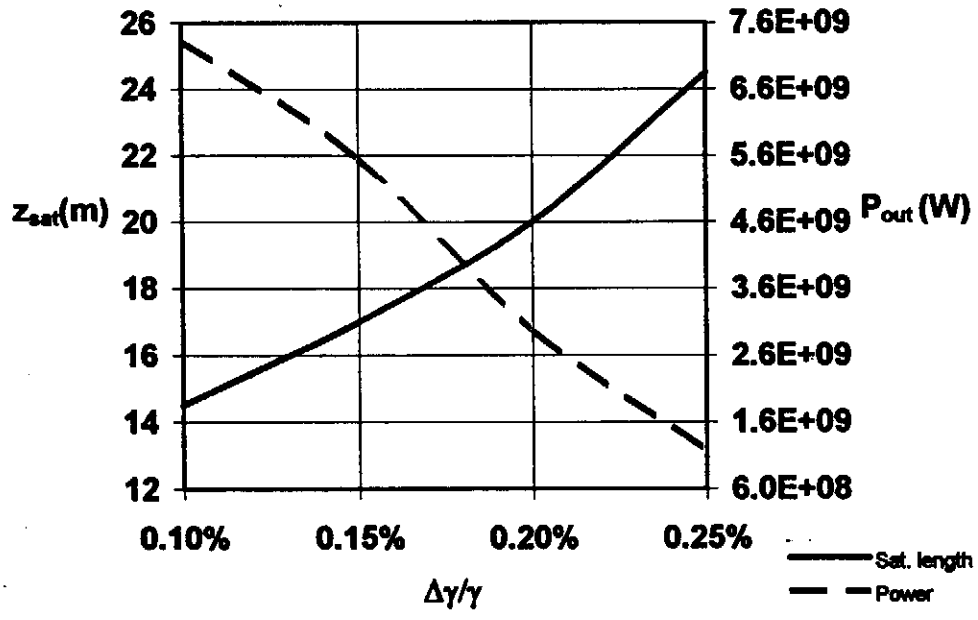

Fig. 11.1: Saturation length and emitted power at peak gain as a function of the electron beam energy spread for ε_n=1 π mm mrad.

For an emittance of 2 π mm mrad, shown in Fig. 11.2, the nominal emittance value assumed in the rest of this chapter, the energy spread limitation are stronger and the maximum allowed energy spread will be around 0.15 %.

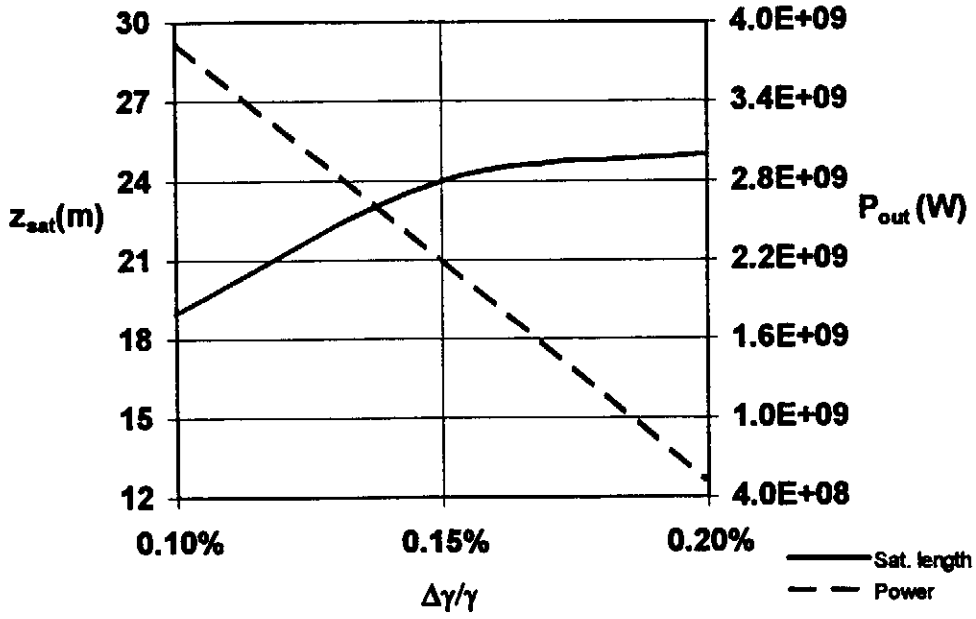

Fig. 11.2: Saturation length and emitted power at peak gain as a function of the electron beam energy spread for ε_n=2 π mm mrad.

As a consequence of these analyses the requirement on the beam enery spread has been set to 0.1%.

11.4.3 Influence of the electron beam emittance

With the assumed nominal value for energy spread of 0.1%, the influence of emittance on the FEL performance is studied. With an emittance of 2π mm mrad, the saturated power is nearly 4 GW. This power is reached after approximately 19 m of undulator. At 1π mm mrad, the peak power is 7 to 8 GW, as was already found in the previous section. Using the same safety margin for saturation length as in the previous section, i.e., 20 m, the maximum allowed emittance is slightly larger than 2π mm mrad. This gives a peak power of approximately 4 GW. The dependence on emittance is not as strong as the energy spread, however, and a slightly larger value is acceptable.

In figure 11.3 the dependence of saturation power and saturation length as a function of emittance is shown for the nominal energy spread value of 0.1%.

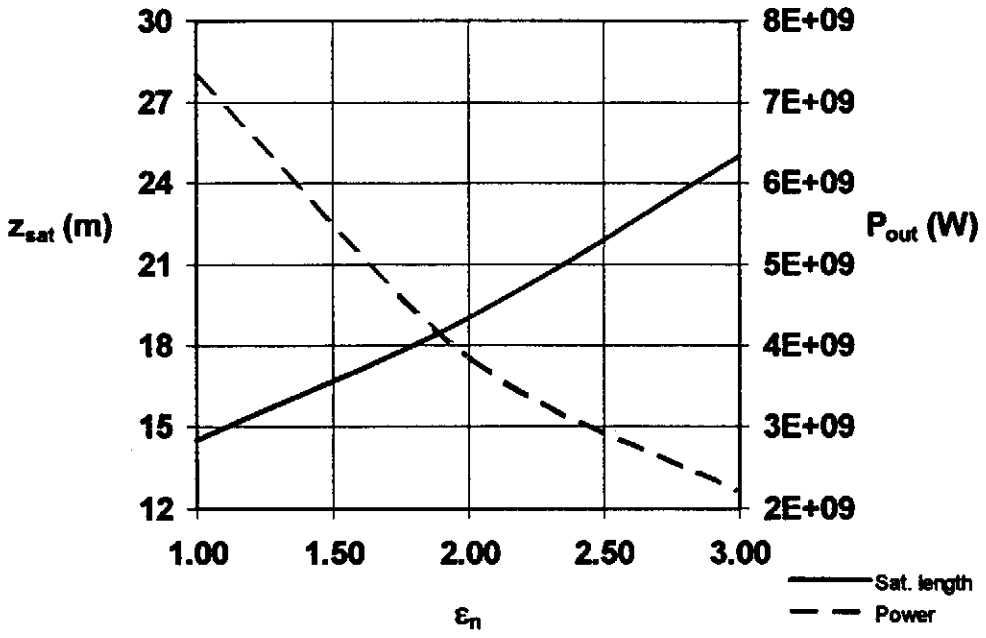

Fig. 11.3: Emitted intensity and saturation length at the peak gain as a function of the normalized electron beam emittance, for the nominal energy spread of 0.1%.

11.4.4 Effect of the electron beam focussing

We restate here the expression of the FEL parameter ρ:

$$\rho = \left(\frac{1}{64\pi^2} \left(\frac{K\lambda_u f_B}{\sqrt{2}\gamma} \right)^2 \frac{I_p}{I_A \beta \varepsilon_n} \right)^{1/3}$$

where I_A = 17 kA is the Alfven current, and β is the beta function of the electron beam during the interaction in the undulator. From this expression it is clear that higher values of ρ can be reached by providing external strong focussing along the undulator. In figure 11.4 we show the behavior of the saturation length and emitted intensity at peak gain for different values of the β function assumed in the undulator.

We choose the value of β=3 m as the nominal value, because it gives a sufficient improvement of the saturation length and is technologically compatible with the modularity of the undulator sections. Lower beta functions are not compatible with the modular design of the undulator. In addition, a smaller beta function would result in a violation of the dependence of emittance and energy spread on the defraction parameter (see section 11.1.1). Further design considerations on the external focussing provided in the undulator can be found in Chapter 10.

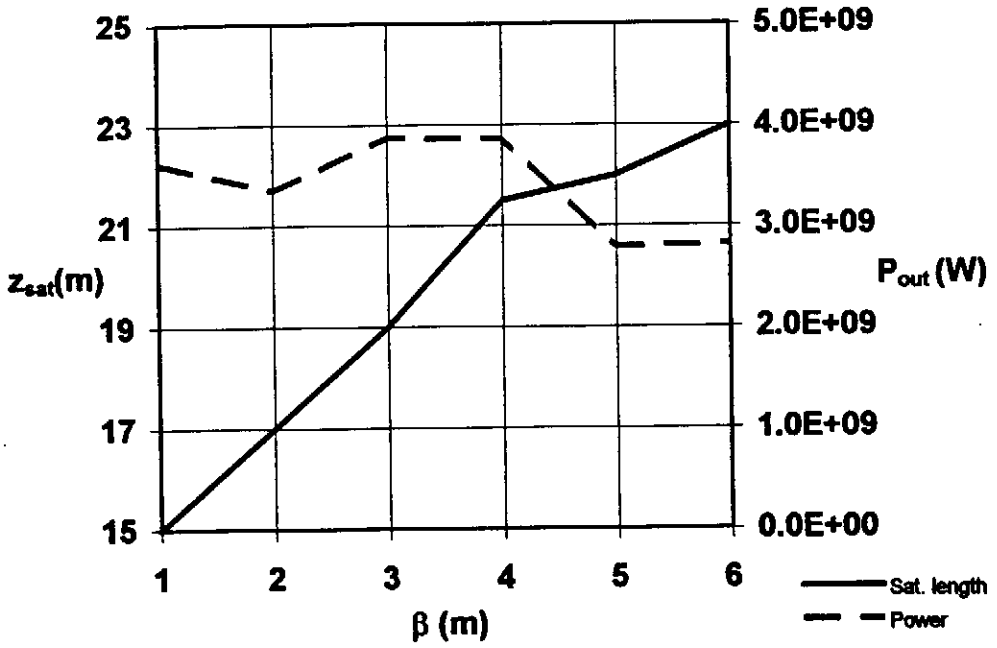

Fig. 11.4: Saturation length and emitted power at peak gain as a function of the external focussing strength.

11.4.5 Influence of Undulator field errors on the TTF-FEL performance

The gain length of an FEL depends on many parameters, among them the magnetic field errors of the undulator. As has been shown by several authors, for example Bobbs [14], Kincaid [15], and Yu [16], the rms field error is not a good parameter to estimate the effect of magnetic field purity on the FEL performance. As an example, Fig. 11.5 shows the power along the undulator for different initial error seeds of the field error. In all cases, however, the rms field error is the same. The saturation power varies over orders of magnitude.

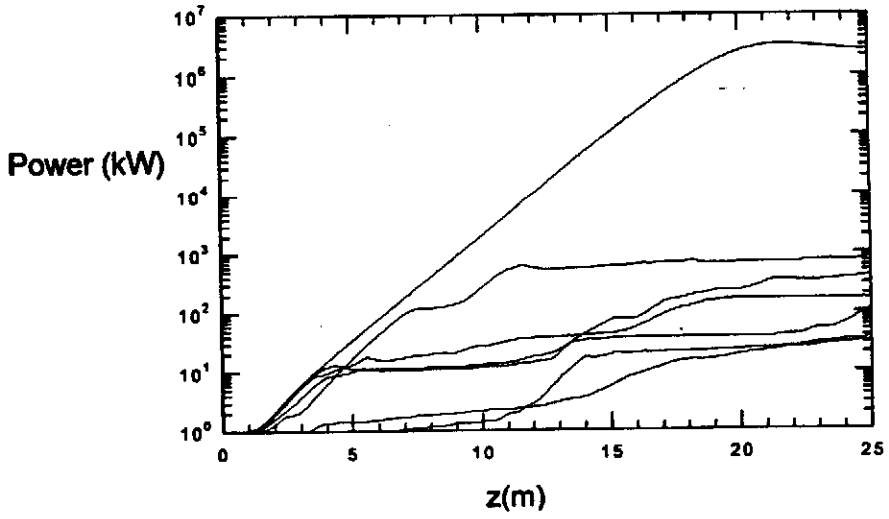

Fig. 11.5: Emitted power as a function of the distance along the undulator, for different field error configurations with the same rms value of 0.5%.

Instead, we use the rms phase shake as a measure of the undulator quality or FEL performance. As a definition for phase, we start with that used in FEL physics,

$$\psi \approx \left(k_u - \frac{k}{2\gamma^2} \right) z - \frac{k}{2} \int \beta_\perp^2 dz,$$

where k_u and k are the undulator and radiation wavenumber, respectively, $\beta_\perp$ the transverse electron velocity normalized to the speed of light and γ the normalized electron energy (Lorentz factor).

In the one-dimensional theory, i.e., neglecting dependence on the transverse coordinates x and y, $\beta_\perp$ can be derived from

$$\beta'_\perp = \frac{K k_u}{\gamma} \cos(k_u z)$$

where $K = eB_u / k_u mc$, as mentioned in the first section of this chapter. This equation gives $\beta'_\perp$ (indicating with the prime the derivative with respect to z) in terms of the magnetic field strength on axis. This quantity can be measured on a bench. Thus, the phase of on-axis electrons can be measured without detailed knowledge of the FEL interaction process. In case of an ideal magnetic field without errors

$$\psi(z) = \left(k_u - \frac{k}{2\gamma^2} \left(1 + \frac{K^2}{2} \right) \right) z + \frac{kK^2}{8k_u\gamma^2} \sin(2k_u z).$$

Note that the last term in this equation is oscillating and the first term gives a linear increase in phase. In order for the em-wave in an FEL to gain energy, the wave has to remain in phase with the electrons, i.e. the phase has to be constant. Therefore, the coefficient of the term linear in z has to be zero. This results in the already mentioned 1D resonance condition.

In the case of a non-ideal undulator, $\beta_\perp(z)$ depends on the complete history, i.e., on the errors of previous poles. The transverse velocity can continuously increase along z, leading to a reduced transverse overlap of the electron beam and the radiation field. This should be compensated by a kick at the undulator entrance or steering between the different undulator sections.

For the wavelength of maximum gain, adding an initial kick to the electron beam, the rms phase shake is defined as the phase at the magnetic poles including errors minus the phase in the case of ideal magnetic field, squared and summed over all poles. With the definition of phase given at the beginning of this section, the ideal ψ is zero. Thus, the phase shake is

$$\sigma_\psi = \sqrt{\frac{1}{2N_u} \sum_{n=1}^{2N_u} \psi^2(n\pi)}.$$

In order to determine the performance of the FEL including the undulator field errors, simulations have been performed with the code TDA3D [12], including magnetic field errors and FODO lattice (see chapter 10). The goal is to systematically study the correlation between phase shake and FEL parameters like saturation length and peak power. These simulations will include the undulator plus superimposed quadrupole focussing. From the calculations we hope to obtain valuable information on tolerance requirements for the manufacturing of the magnetic structure as well as hints for a sorting strategy and the distance between steering stations to keep the electron beam close to the optical axis. Fig. 11.5 already shows some of the potentials. Clearly there are 'bad' and 'good' configurations having the same RMS values but totally different saturation power levels. First results have been obtained and will soon be published.

11.4.6 Higher harmonics contents of the emitted radiation

We have used NUTMEG to estimate the third harmonic content of the emitted radiation. As a consequence of the strong bunching induced by FEL emission, the higher order harmonics are nonlinearly driven by the exponential diverging fundamental field. At saturation, for the nominal parameters of the TTF FEL proposal, the 3rd harmonic wavelength (at λ_3=2.14 nm) reaches the value of approximately 6 MW, showing a gain of nearly 12 dB/m, three times greater than the gain at the fundamental wavelength (4 dB/m). This behavior can be fully understood in a simple 1D multiharmonic analysis of

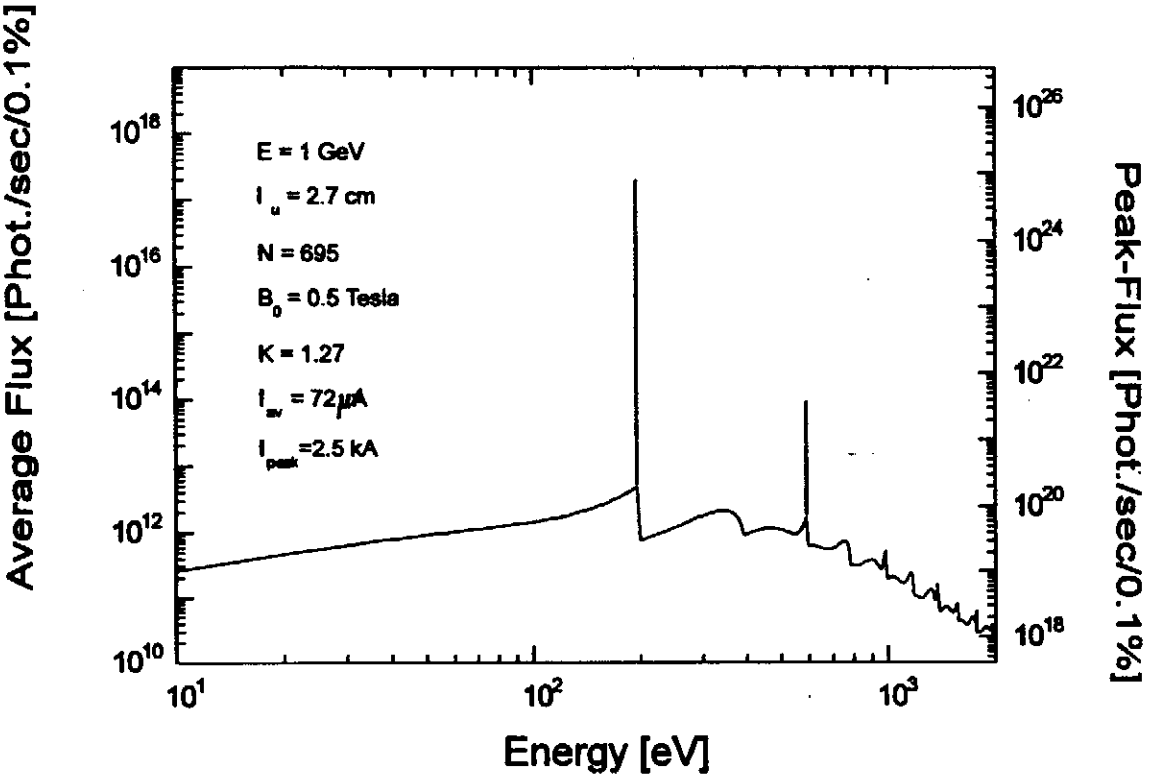

Fig. 11.6: Expected emitted photon flux by the TTF SASE FEL. The two peaks correspond to the FEL emission at the fundamental and 3rd harmonic. The lower curve is the spontaneous emission in the undulator.

the FEL, where it can be analytically shown that the n^{th} radiation harmonic is driven at a gain n times larger than the gain at the fundamental [17]. In Fig. 11.6, we compare the data for the FEL fundamental and third harmonic emission to the photon flux due to the spontaneous emission in the undulator.

References

1 R. Bonifacio, C. Pellegrini, L.M. Narducci, Opt. Commun. 53 (1985), 197;
2 K.J. Kim, Nucl. Instrum. and Methods A250 (1986), 396; K.J. Kim, M. Xie, Nucl. Instr. and Methods A331 (1993), 359; K.J. Kim, Nucl. Instrum. A58 (1995), 31;
3 C. Pellegrini et. al., Nucl. Instrum. and Methods A341 (1994) 326; L.H. Yu, S. Krinsky, R.L. Gluckstern, Phys. Rev. Lett. 64 (1990), 3011; Y.H. Chin, Nucl. Instrum. and Methods A331 (1993), 424; Y.H. Chin, K.J. Kim, M. Xie, Phys. Rev. A46 (1992), 6662; R. Bonifacio, L. De Salvo Souza, B.W.J. McNeil, Opt. Commun. 93 (1992), 73; E.L. Saldin, E.A. Schneidmiller and M.V. Yurkov, Opt. Commun. 97 (1993) 272
4 R.Bonifacio, L.De Salvo, P. Pierini, N. Piovella, C. Pellegrini., Phys. Rev. Lett., 73 (1994), 70;
5 W.M. Fawley, A.M. Sessler, E.T. Scharlemann, Proceedings of the 1993 Particle Accelerator Conference, IEEE (1993), Vol. 2, 1530;
6 The 1D time dependent simulation code SARAH by P. Pierini has been used to test the theory presented in Ref. 4;
7 G. Travish, Nucl. Instrum. and Methods A 358 (1995), 48;
8 E.L. Saldin, E.A. Schneidmiller, M.V. Yurkov, DESY Report 94-219, November 1994; E.L. Saldin, E.A. Schneidmiller, M.V. Yurkov, Calculations with FS2R code of 6 nm and 70 nm options of SASE FEL at the Tesla Test Facility, to be published;
9 E.T.Scharlemann and W.M. Fawley, in Modeling and Simulation of Optoelectronic Systems, SPIE, vol. 642 (1986), p. 1;
10 R.A.Jong, W.M.Fawley and E.T.Scharlemann, in Modeling and Simulation of Laser Systems, SPIE, vol. 1045 (1989), p. 18;
11 T.-M. Tran and J.S. Wurtele, Comp. Phys. Comm. 54 (1989) 263;
12 P. Jha and J.S. Wurtele, Nucl. Instr. Meth A331 (1993) 477;
13 E.L.Saldin, E.A.Schneidmiller, M.V. Yurkov, to be published as a TESLA-FEL report and submitted to Elsevier Science.
14 B.L. Bobbs, G. Rakowsky, P. Kennedy, R.A. Cover, D. Slater, Nucl. Instrum and Methods A296 (1990), 574;
15 B.M. Kincaid, J. Opt. Soc. Am. B2 (1985), 1294;
16 L.H. Yu, S. Krinsky, R.L. Gluckstern and J.B.J. Zeijts, Phys. Rev. A45 (1992) 1163;
17 R.Bonifacio, L.De Salvo, P.Pierini, Nucl. Instrum. and Methods, A293 (1990), 627;

12. Shielding and Beam Dump

12.1 Shielding along the TTF Linac

Based on the TTFL parameter list, the shielding for the linac with its 800 MeV maximum electron beam energy has been calculated according to the German safety regulations [1]. Two comprehensive [2,3] publications emphasize the requirements for scattered radiation. We first have calculated the dose per lost electron behind some shielding material; from this one can easily develop the necessary shielding thickness.
The following operating parameters have been used:

	E	=	800 MeV
	N_e / macro pulse	=	$4 \cdot 10^{13}$ e^- / pulse
	f_{rep}	=	10 Hz
	N_e / second	=	$4 \cdot 10^{14}$ e^- / second
=>	$I_{average}$	=	64 µA
	P	=	51.2 kW

The standard wall thickness along the linac itself is only 80 cm heavy concrete. This relatively small value is possible for the following reasons. The superconducting linac gives some safety just because of the fact that the maximum acceptable losses at low temperatures are extremely low. The at 1.8 K needed cryogenic power is 160 W, the installed power is limited to 200 W. Therefore, beam losses of more than 40 W would not allow the operation of the linac; 40 W correspond to $8 \cdot 10^{-4}$ of the average 51.2 kW. The losses have to be more or less equally distributed along the 50 m long linac since otherwise a local quench would occur. Anyhow, assuming a point source producing the dose equivalent to a 5 m long linac section, an operation of 1000 hours per year at maximum beam current would result in $1.1 \cdot 10^{17}$ lost electrons per year.

The maximum acceptable losses have to be distributed since the loss of approximately $1 \cdot W/cm^2$ would cause a quench. With a Niobium wall thickness of 2.5 mm and an energy loss of typically 2 MeV cm^2 / g, this corresponds to about $1.2 \cdot 10^9$ electrons per pulse on an area of 1 cm^2, or $3 \cdot 10^{-5}$ of one pulse, or 4% of the above mentioned, equally distributed losses.

The warm part behind the fourth cryo module (experimental area) needs 1.6 m of heavy concrete shielding. Here, the beam losses will be monitored using toroids placed at different locations along the beam line. In the case of losses the gun emission will be reduced. The resolution in the differential current measurement is 0.1 mA or 1.25% of the beam current. Concentrating the losses in a 12 m long warm section to point like sources one gets $6 \cdot 10^{18}$ lost electrons per year for 1000 hours of operation.

Outside of the shieling ion chambers will measure the electromagnetic component of the radiation and moderating neutron counters take care of the neutron dose. Both detectors produce one pulse per 1 µSv which are used to calculate the total losses. At a dose of

900 μSv / h the electron gun emission will be stopped after 4 s; at 40 μSv / h this will be done after 1.5 min.

The dose per year has been calculated, and under the above mentioned constraints the maximum dose behind the linac shielding is limited to 30 mSV / a. Behind the 1.6 m shielding for the warm sections one gets a maximum of 20 mSV / a which is sufficient. The detailed description of this calculation as well as of the beam monitoring and beam inhibit system can be found in [4].

Any further extension of the linac to higher energies will be shielded by 160 cm concrete down to the deflecting magnet. The system to deflect the beam into an absorber has to be designed to work with high reliability. A combination of electro-magnet and permanent magnet is under consideration.

The main experimental area with the direct photon beam at 0 deg needs concrete shielding for the following reasons (see also Fig.2.4 and Fig.13.2).

a) Small electron beam losses along the linac and especially along the wiggler create electromagnetic cascades. Their central component (and also neutrons) enter the experimental area.

b) A possible malfunction of the deflecting system, scattering part of beam into the area, requires a miniumum concrete shielding.

c) X-ray production in the cavities. Example: Even outside the beampipe a dose rate of 100 R/h was measured just behind the superconducting cavities in HERA WEST, this during the conditioning and without the injection of an electron beam.

The concrete shielding could have a thickness of 80 cm.

At the end of the main experimental area a heavily shielded absorber is necessary.

In the second experimental area with the photon beam reflected by mirrors it is also not possible to stand at the beam pipe. The necessary shielding depends on the amount of photons (see above) scattered from the mirrors down the beam line. The fluence of photons will be measured during an early stage of development, and the shielding will be determined from this. Anyhow, a beam shutter can be used to allow the access to this area while having the photon beam in the straight section's experimental area.

12.2 Electron Beam Dump

12.2.1 Design of the Standard TTF Dump

The preliminary design of the TTF dump was made assuming the following parameters: $E_{beam} = 800$ MeV, $I_{avg} = 64$ μA, 10 bunch trains per second with a length of 800 μs each and a minimum beam size of $\sigma_x \sigma_y > 2.25$ mm^2. These parameters imply an average beam power of 52 kW which has to be safely absorbed by a the dump. The main problem of such a dump is usually the large temperature gradient in the absorber material which may

lead to unacceptable stresses. The maximum temperature rise on the beam axis consists of two parts:

1. The instantaneous temperature ΔT_{inst} which arises from the deposition of beam power in the small volume of the beam cone during the passage time of one bunch train, and
2. the equilibrium (average) temperature ΔT_{eq} which is mainly determined by the heat conductivity and cooling of the absorber material[1].

At the entrance of the dump the small beam size leads to a large instantaneous temperature whereas the equilibrium temperature becomes more important near the shower maximum. The best solution turned out to be a cylindrical graphite core in an aluminum tube as primary absorber, followed by an aluminum and a copper section. It is planned to use so called reactor graphite MPG-6 with a density of $\rho = 1.71$ g/cm^3 for

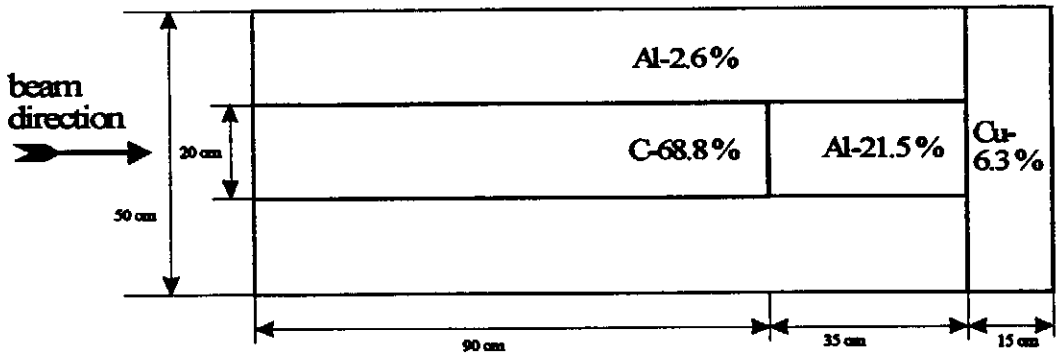

Fig. 12.1: Longitudinal section of the beam dump. The numbers give the relative amount of power deposition in the corresponding section.

the graphite core, which exhibits a high temperature and stress resistivity and a relatively high thermal conductivity. A further advantage of graphite is the moderate energy deposition per unit length dE/dx which helps to keep the equilibrium temperature low. Fig. 12.1 sketches the dump dimensions and the arrangement of materials in the standard TTF dump. The peak temperatures in the aluminum and graphite sections are about 140 °C and 390 °C, respectively.

12.2.2 Upgraded Beam Parameters

The use of the TTF linac as an FEL driver requires different beam parameters. The most important parameter change concerns the increase of the beam energy from 0.8 GeV to 1.0/1.2/1.6/2.0 GeV while the average beam current is kept constant. Furthermore the structure of the bunch train is modified - the number of bunches in one train is increased by a factor of eight while the charge per bunch is reduced by the same factor. The length of each train is kept at 800 μs. The heat diffusion length in the absorber material for the passage time of such a bunch train, given by

$$< \Delta x > = \sqrt{\frac{\Delta t \lambda}{\rho c}} \approx 260 \mu m ,$$

[1] see the Tesla-Test-Facility Design Report for a detailed description

is less than the beam size of $\sigma_{x,y} > 1500$ μm. Therefore the approximate assumption of a δ-function like instantaneous heating should be valid.

12.2.3 Implications on the Beam Dump

We consider here three possibilities to absorb the high energy TTF-beam:

a) Usage of the normal TTF dump, designed for 800 MeV

The critical temperature is in the aluminum section, whereas the graphite temperature is far below the possible limit. It is increased overproportionally with the beam energy, since not only the total power is increased but also the depth of the shower and therefore the relative amount of deposited power in the aluminum section. In order to keep the maximum temperature in the aluminum constant one has to reduce the beam current. Maximum beam currents for different beam energies, obtained from GEANT simulations, are given in table 12.1. Furthermore the amount of radiation leakage out of the dump body has been considered for the different energies, including the beam current reduction. The simulation shows that the total radiation leakage is actually reduced due to the current reduction in all cases. Reduced current, however, would not meet the final design goals.

b) Construction of a longer dump

In order to keep the temperature in the aluminum section low one could lengthen the graphite section (fig. 12.1). In this case a new design is necessary and unfortunately the length of the beam dump would exceed the raster size of the concrete shielding blocks of 1.6 m. For constant temperature in the aluminum section the length of the graphite section has to be approximately 90/105/116/132/144 cm for beam energies of 0.8/1.0/1.2/1.6/2.0 GeV respectively.

beam energy [GeV]	I_{max} [μA]	$P_{loss,\ transversal}$ [W]	$P_{loss,\ longitudinal}$ [W]
0.8	64	301	97
1.0	45	255	103
1.2	34	223	110
1.6	22	186	123
2.0	16	163	131

Table 12.1: Consequences for the usage of the standard TTF dump with different beam energies. I_{max} is the maximum allowed beam current for a constant temperature in the aluminum section. Furthermore the total radiation leakage in transversal and longitudinal direction is given (the current reduction is taken into account).

c) Pyrolytic graphite

Another possibility to increase the effective length of the graphite section is the use of pyrolytic graphite with a higher density of $\rho \approx 2.1$ g/cm^3. With a beam current of 32 μA, 1.6 GeV and the original dump dimensions the resulting maximum temperature in the

aluminum section can be kept to 140 °C. The radiation leakage amounts to 270 W transversely and 122 W longitudinally. This solution seems most promising because the original dump dimensions can be used - only the graphite has to be exchanged. However, a disadvantage is the higher price of the pyrolytic graphite and possibly the availability of the material.

An even denser material is silicon carbide (SiC) which could also be used in the dump core. However, due to the much higher energy loss per unit length a critical temperature can also be reached in the outer aluminum tube. Therefore further careful study of the SiC option is required.

12.2.4 Conclusions

In principle the standard TTF dump can be used without radiation leakage problems at any energy up to 2.0 GeV. With rising energy the beam current has to be reduced according to table 12.1. If higher currents are needed the simplest solution is obtained by filling the standard beam dump with pyrolytic graphite instead of the MPG-6 material. This will allow 50 % of the design current at a beam energy of 1.6 GeV. The construction of a longer dump would also solve the problem, but needs more effort. A somewhat longer dump, filled with pyrolytic and partly silicated graphite could be the best solution for 2 GeV at full beam current. The extraction of a higher beam power has consequences for the water cooling circuit parameters which have to be investigated in more detail.

It should be mentioned that the estimates of the maximum allowed temperatures contain several pessimistic assumptions. It is therefore imaginable that the current limits in table 12.1 can be exceeded without danger. The standard beam dump of the Tesla-Test Facility will be equipped with several diagnostic tools, especially temperature sensors, which can help to estimate the real limits from practical experience.

References

[1] Strahlenschutzverordnung 1989, Bundesanzeiger Verlags-Ges.mbH, Köln.

[2] H. Dinter et al., Calculations of Doses due to Electron-Photon Stray Radiation from a High Energy Electron Beam behind Lateral Shielding, Rad. Prot. Dosimetry Vol. 25, No. 2, pp. 107 - 116, (1988).

[3] K. Tesch, Shielding Against High Energy Neutrons from Electron Accelerators - A Review, Rad. Prot. Dosimetry, Vol. 22, No. 1, pp. 27 - 32, (1988).

[4] *TESLA Test Facility - Conceptual Design Report,* TESLA Report 95-1, DESY 1995.

13 Civil Engineering

13.1 Overview

The extension consists of 3 part:

1) A straight tunnel with connection to the shielding building at bldg. no. 28 (Hall 3)

2) Beam switchyard with subsequent shielding

3) Experimentation Hall

Figure 2.4 (see chapter 2) shows an overview of the planned new buildings. The shielding building with connection to Hall 3 is already in the process of realization.

13.2 Local Conditions

The beam will be directed into northern direction out of the Hall 3. The required building can be built between the existent dry well and the spray pond. They get road access in the north to the PETRA ring road. Within the planned location route, the dry well must be pipe cased. In addition, the existing cable trays and pipetrays must be sinked.

13.3 Description of Buildings

13.3.1 Tunnel

The tunnel will be built from pre-fabricated reinforced concrete sections of 5.0 m circumference. In the massive floor, supply channels are foreseen. At the tunnel wall, fixing of cable trays etc. has to be provided. Radiation shielding is provided by at least a 3 m sand bank. Support walls from reinforced concrete are able to stand the load from the sand shielding. Figure 13.1 shows a cross section of the tunnel.

13.3.2 Connection from Tunnel into Experimentation Hall

A bending magnet will be installed to ensure that the electron beam cannot enter the hall. Instead, the beam is deflected into a beam dump. This region can simultaneously be used for beam analysis, e.g. for spectrometer, bunch length and emittance measurements. It is to be shielded by loaded concrete 3.5m x 3.5m.

13.3.3 Experimentation Hall

The hall consists of reinforced concrete piles, connected to the concrete foundation. Walls and roofs are made from 20 cm thick gas concrete slabs. The roof will be sealed by bitumen. As a means of natural lighting, double glazed sections of structural glass will be let into the side walls. Figure 13.2 shows a layout of the hall.
The hall will be supplied with a movable crane on tracks which will carry up to 10 tons with a hook height of 6 m. There will be access to the hall from the front of the hall on the street and also on the west side wall.

In the North-east the hall could later be extended. From this area an extended control system for the experiments would be possible. Within the hall, shielding of the experiments and of the beam consists of movable concrete blocks.

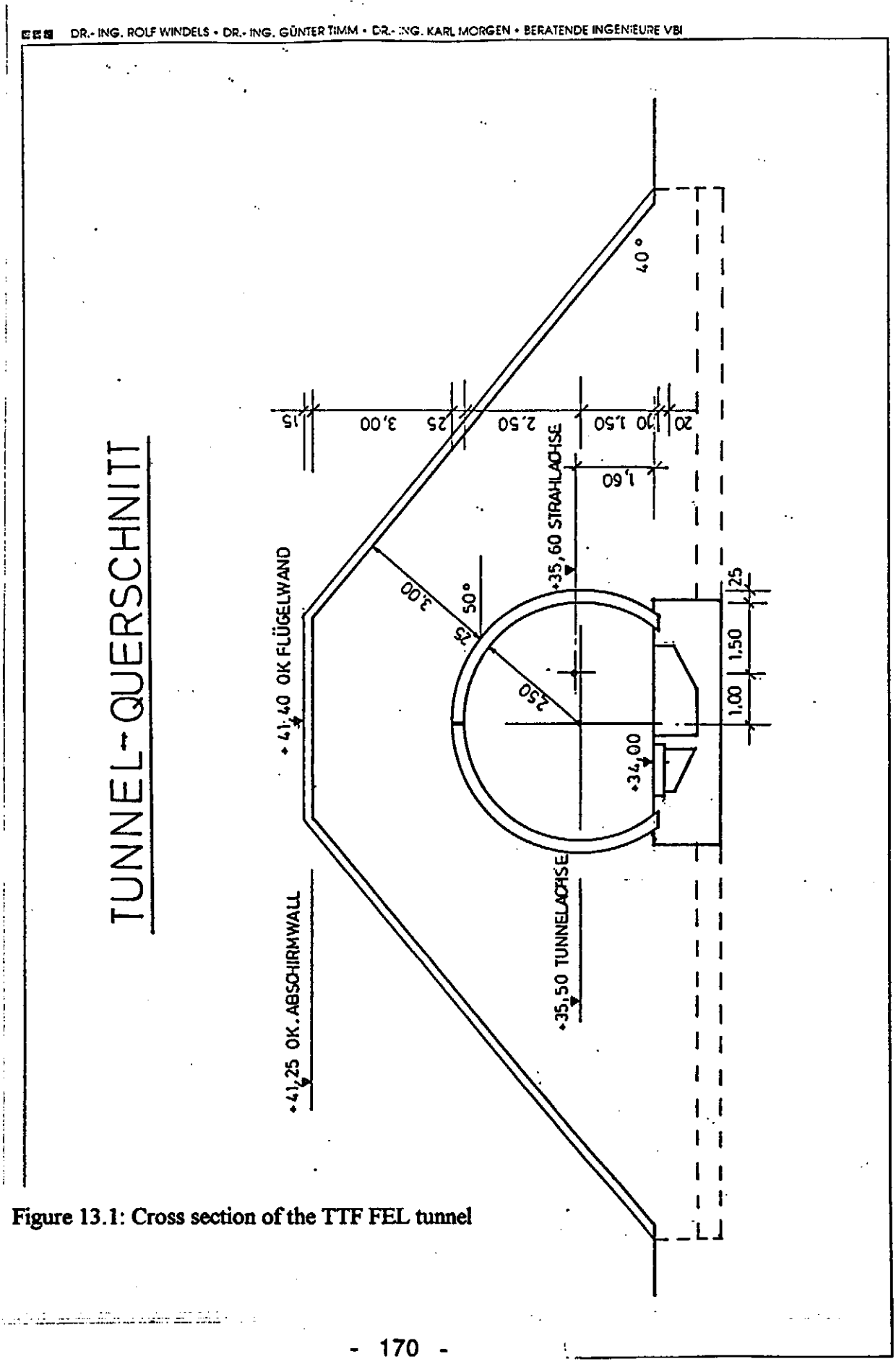

Figure 13.1: Cross section of the TTF FEL tunnel

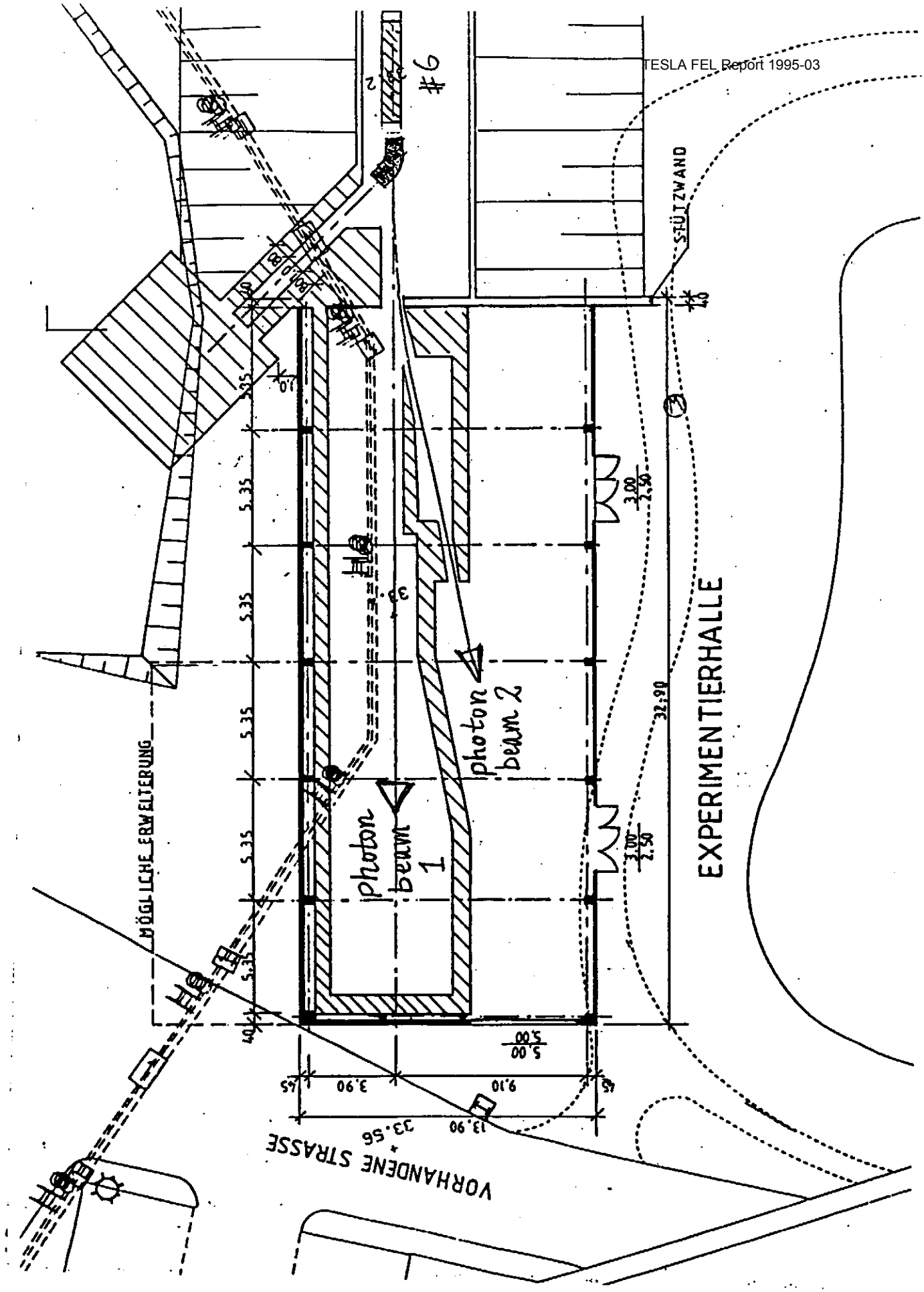

Figure 13.2: Layout of the Experimental hall

14 Future Potential

14.1 Photon Energy Upgrade

As has already been pointed out in Chapter 11, one big attraction of the SASE FEL scheme is the absence of no apparent limitation which would prevent operation at even smaller wavelengths: therefore, the most obvious first upgrade step would certainly be to increase the photon energy. From the users point of view, a photon energy above 290 eV would be very useful ("water window"). To achieve this energy, the TTF FEL electron energy would have to be 1.23 GeV.

Depending on the progress of superconducting rf technology, it may be that the required accelerating gradient of 18.3 MeV/m can be reached with TESLA accelerating modules. Note that the TESLA 500 Linear Collider scheme presently assumes 25 MV/m, so that there is a big common motivation of both FEL and high energy physics communities to exceed the TTF goal of 15 MV/m. An alternative way to reach higher beam energies is to increase the effective accelerator length. To avoid major reconstruction work, one could think of electron beam recirculation. While this is an attractive option for superconducting linacs, experience with the TTF FEL will show if the beam can be sufficiently well controlled so that this further complication can be managed within the very tight FEL tolerances.

It has been mentioned previously that decreasing the photon wavelength also decreases the maximum tolerable beam emittance. This could be partially compensated by increasing the undulator K-parameter, which, however, means rebuilding the undulator and even higher electron energy. Thus, improving the electron gun towards even smaller beam emittances will be an issue for any photon energy upgrade.

The other way to reach smaller wavelength is to decrease the undulator period length λ_u . An attractive future alternative to the proposed planar hybrid undulator could be a superconducting helical undulator, because it may allow the reduction of the period length by a factor two to three. Further work on such a device might well pay off.

14.2 Resonant harmonic generation

One other option to go to even shorter wavelength is to employ a two wiggler scheme for resonant harmonic generation, using the fact that the electron beam is bunched by the FEL interaction [1,3]. The spectral content of the electron beam bunching include all higher harmonics of the emitted wavelength. A logical choice would therefore be to use a short undulator section (the buncher) tuned at 6 nm to develop the electron bunching and a second undulator section (the radiator) tuned to the third harmonic of the radiation wavelength. The difference between lasing with a single undulator operating at 2 nm compared to lasing at 6 nm with a buncher/radiator scheme is, in the latter case, one does not have to fulfill the emittance requirement at the short wavelength. In this case the power in the harmonic resonator is mainly limited by the energy spread induced by the FEL action in the buncher.

We have performed NUTMEG simulations to test this scheme with the TTF FEL parameters. The length of the TTF undulator has been decreased to 15 meters in order to

minimize the energy spread induced by the strong FEL action. In this case a short radiator length is needed in order to have appreciable power at 2 nm. In Figure 14.1 we show the emitted 2 nm radiation intensity as a function of the radiator length. The power reaches 50 MW after 1.5 m. The undulator used in this section is a short period, high field device (1.2 cm period length, 7.6 kG peak field), that can make use of superconducting magnet technology.

This option would obviously need a change in the setup of the different undulator sections, which have to be properly realigned. We note here, however, that the proposed beam emittance of 2π mm mrad would not fulfill the emittance requirement for emission at 2 nm without the bunching developed in the buncher.

In all setups, even though the severe limit on emittance is relaxed, the influence of wiggler field errors is expected to be more severe. This has not been studied in detail to date and will be subject of further investigation.

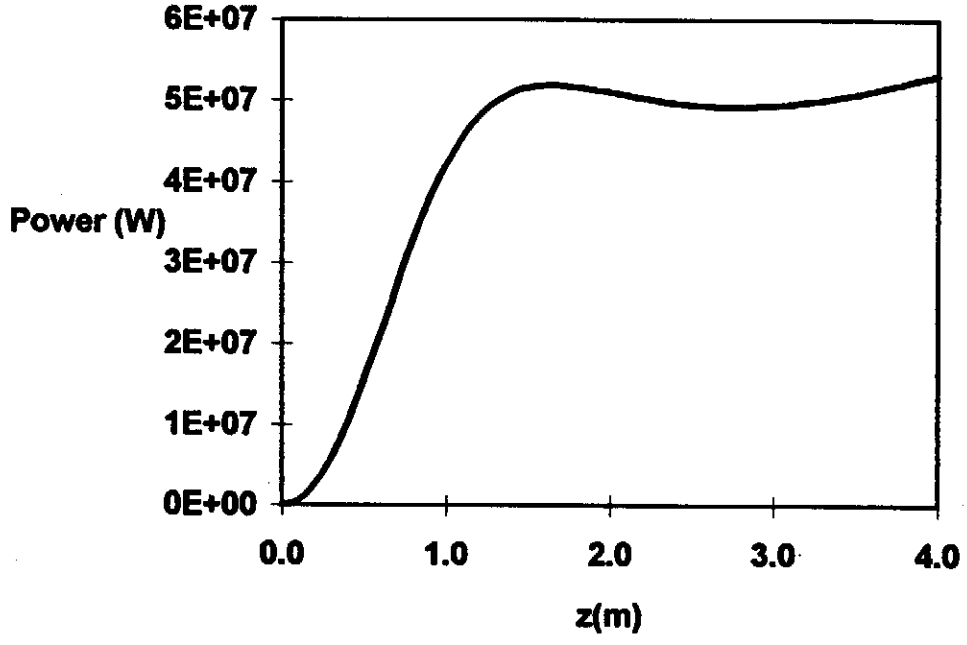

Fig. 14.1: Emitted intensity at 2 nm in the radiator section of a two undulator scheme for the TTF SASE FEL proposal.

14.3 Increased Radiation Power by tapering

It is an inherent advantage of single pass, linac based FELs that by undulator tapering there is the potential to improve the saturation power by more than an order of magnitude. Combined with the excellent power efficiency of a superconducting linac, one can imagine an overall wall-plug to photon beam efficiency above 1 %. This is well beyond the efficiency of a storage ring based FEL which is limited to about one permille according to the Renieri limit [4]. High power efficiency operation might increase the attractiveness for potential industrial applications.

An intrinsic complication with tapering at SASE FELs is related to the fact that the saturation length fluctuates from pulse to pulse due to the stochastic nature of starting from noise. Thus finding the optimum tapering configuration needs further theoretical studies and experimental experience with the SASE saturation.

References

1 P. Pierini, R. Bonifacio: 1-2 nm radiation emission at the SASE FEL on TTF, to be published;
2 R. Bonifacio, L. De Salvo Souza, P. Pierini, E.T. Scharlemann, Nucl. Instrum and Methods A304 (1991), 224;
3 F. Ciocci, G. Dattoli, A. de Angelis, B. Faatz, F. Garosi, L. Giannessi, P.L. Ottaviani and A. Torre, ENEA report, submitted to IEEE J. Quant Elec.;
4 W.B. Colson, C. Pellegrini, A. Renieri (eds.): Laser Handbook Vol. 6, North Holland (1990).